Metals and Ceramics Division

Heavy Vehicle Propulsion Materials Program
Quarterly Progress Report for
April through June 2002

D. R. Johnson
Technical Project Manager

Prepared for
U.S. Department of Energy
Assistant Secretary for Energy Efficiency and Renewable Energy
Office of FreedomCAR and Vehicle Technologies Program
EE 07 01 00 0

Prepared by the
OAK RIDGE NATIONAL LABORATORY
Oak Ridge, Tennessee 37831-6066
Managed by
UT-Battelle, LLC
for the Department of Energy
Under contract DE-AC05-00OR22725

CONTENTS

Materials and Testing Standards

Implementing Agreement for a Programme of Research and Development on Advanced Materials for Transportation Applications (ORNL)

Standards for Reliability Testing of Heavy Vehicle Propulsion Materials (NIST)

Mechanical Property Test Development (NIST)

Development Of Low-Cost Austenitic Stainless Diesel Engine Components With Enhanced High-Temperature Reliability

P.J. Maziasz and R.W. Swindeman
Oak Ridge National Laboratory
and
M.E. Frary and M.J Pollard
Caterpillar, Inc.

Objective/Scope

The objective of this work is to evaluate cast austenitic stainless steels as high-performance alternatives to SiMo ductile cast iron, which is currently the standard material used in most diesel engines for exhaust manifold and turbocharger housing components. The new material must be able to withstand prolonged exposure at temperatures of 750°C or above, as well as to survive the severe thermal cycling from near room-temperature to such high-temperatures without developing cracks. This project has tested commercially available cast alloys, as well as developed new, modified cast alloys with significantly enhanced performance. The ultimate project goal is to provide high-performance, reliable materials that are also cost-effective for such applications. This advanced diesel engine work is part of a broader CRADA (Cooperative Research and Development Agreement) project (ORNL99-0533) that began July 21,1999, and was scheduled to end July 22, 2001, but has been extended for 12 more months. Any more detailed information on this project must be requested directly from Caterpillar, Inc.

Technical Highlights, 3rd Quarter, FY2002

Background

Advanced large diesel engine must have higher fuel efficiency as well as reduced exhaust emissions, without sacrificing durability and reliability. Therefore, exhaust manifold and turbocharger housing materials must withstand temperatures ranging from 70 to 750°C or higher in a normal duty cycle that includes prolonged, steady high-temperature exposure as well as more rapid and severe thermal cycling. New technology to reduce emissions and heavier duty cycles will push temperatures in these critical components even higher. Current exhaust components are made from SiMo ductile cast iron, and higher engine temperatures would push such materials well beyond their current strength and corrosion limits. Therefore, one goal of this project was to generate the new data on alternate higher performance materials like cast austenitic stainless steels to enable materials selection and component lifing. There is limited industrial experience on cast austenitic stainless steels like CN12, especially for diesel engine applications, and little high-temperature mechanical properties data available, particularly creep and fatigue. The main purpose of this project was to produce data comparing cast CN12 and SiMo cast iron for such diesel exhaust component applications. Another component of this project was a parallel alloy development effort to further optimize the cost-effective performance of such cast austenitic stainless steels.

Approach

Commercial cast CN12 austenitic stainless steel (Fe-25Cr-13Ni-1.8Nb, C, N, S) was chosen as the baseline alloy for evaluation relative to SiMo ductile cast iron. Materials were evaluated in

the as-cast condition as well as after appropriate thermal aging at temperatures up to 850°C. Tensile and isothermal cyclic fatigue properties were evaluated selectively from room temperature up to 900°C, together with some high-temperature creep-rupture and oxidation/corrosion testing. Microstructure analysis was performed on some of the specimens to better understand mechanisms associated with the properties changes. In a parallel effort, new alloying element modifications were made to CN12 and to CF8C cast steels to further enhance their high-temperature performance.

Technical Progress

Previously, tensile and creep properties were obtained on commercial cast iron and on commercial, baseline CN12 stainless steel. Tensile data on CN12 included unaged and aged specimens. High-cycle isothermal fatigue testing at 700°C and 850°C at ORNL has been completed, and some thermal fatigue testing over this temperature range has been done at Caterpillar on one of the new modified CN12 alloys. Microstructural analyses of selected specimens of as-cast or as-cast and aged materials was done at ORNL to better understand the properties behavior and to establish the effects of aging on the baseline CN12 material. CN12 has a clear tensile strength advantage and an overwhelming creep-strength advantage over SiMo cast iron above 550-600°C. The isothermal fatigue data at room temperature and at 700°C also shows an enormous fatigue life advantage of CN12 over the SiMo cast iron.

For the alloy development effort, eight smaller heats (15 lbs each) of modified CN12 austenitic stainless steels were produced at ORNL and evaluated. Initial screening of as-cast or cast and aged material included tensile testing. As-cast material was also creep-rupture tested at 850°C. Significant improvements were achieved in the high-temperature strength and aging resistance of the modified CN12 stainless steels. The best modified CN-12 alloys was five to ten times better relative to the standard commercial CN-12 alloy for creep-rupture testing at 850°C and 110 MPa.

In addition to the modified CN12 austenitic stainless steels, a similar effort was made to modify a less costly and more castable CF8C (Fe-19Cr-12Ni-Nb, C) austenitic stainless steel. While CF8C steel had been previously considered as a candidate for diesel exhaust applications, it was dismissed for lack of high-temperature strength. Standard commercial CF8C is used for gas-turbine exhaust components used below 650°C. Three smaller heats of modified CF8C were made at ORNL (one baseline unmodified alloy and two modified alloys) and evaluated for tensile and creep-rupture properties at 850°C and 35 MPa. The best modified CF8C steel has dramatically better creep resistance at 850°C standard, commercial CF8C. The standard commercial CF8C steel ruptured after about 500 h, whereas one modified CF8C steel ruptured after almost 13,000 h last quarter, and the best modified CF8C steel has exceeded 21,000 h without rupture. Additional creep-test of standard, commercial CN12 steel began previously for comparison with the best modified CF8C steel at the same creep conditions, and that test has exceeded 10,000 h without rupture.

Communications/Visits/Travel

Team communications between ORNL and Caterpillar occur in detail at least several times a week. The current CRADA was extended another 6 months, and will end July 22, 2002. A new 3-year CRADA for commercial scale-up and evaluation of component manufacture and

performance with the new modified CN12 and CF8C steels has been agreed to and is currently in the final stages of the approval process.

An invention disclosure and patent application on cast austenitic stainless alloys with improved performance were completed by Caterpillar and filed with the U.S. Patent Office in December 2000. It is entitled "Heat and Corrosion Resistant Cast Stainless Steels With Improved High Temperature Strength and Ductility," by P.J. Maziasz (ORNL), T. McGreevy (U. of Bradley/CAT), M.J. Pollard (CAT), C.W. Siebenaler (CAT), and R.W. Swindeman (ORNL).

Status of Milestones

Formal milestones were imbedded in the CRADA and are not part of the HVPM Program FWP. However, all milestones have achieved on or significantly ahead of schedule.

Publications

There have been several detailed internal reports on this project at the Caterpillar Technical Center.

A final report on this CRADA will be issued next quarter.

Development of NO_x Sensors for Heavy Vehicle Applications

Timothy R. Armstrong
Oak Ridge National Laboratory

CRADA No. ORNL 01-0627
with Ford Motor Company

Objective

The proposed project seeks to develop technologies and materials that will facilitate the development of NO_x and ammonia sensors. The development of low-cost, simple NO_x will facilitate the development of ultra-low NO_x emission engines, directly supporting the OHVT goals.

Technical Highlights

1. An evaluation of the thermodynamic equilibrium of NO_2 and NO led the team to decide to develop a NO sensor that would operate at 700°C. In this scenario only 10% of the NO_x is NO_2 that would have to be catalyzed to NO to obtain an accurate reading. At reduced temperatures the NO_2 concentration increases rapidly making catalysis more difficult to drive to 100% completion.
2. The sensor design to be developed is a simple mixed potential sensor with a 2-electrode design.
3. We completed the technical evaluation of the current literature and patents relating to NO_x sensor materials. The literature indicates:
   a) That NO_x sensors are sensitive to hydrocarbons and therefore all hydrocarbons in the exhaust stream will need to oxidized to CO_2.
   b) For any given electrode material NO and NO_2 give opposite, but not equal signals. Therefore it is imperative to sensor only NO or NO_2. Sensing NO_x on a single electrode will provide inaccurate results.
   c) None of the literature indicated that any research institution tested their materials in real exhaust gases. Many of the materials developed have known sensitivities to impurities in exhaust gases such as SO_2 and some have failed testing at Ford.
4. Based on the literature survey a sensor was designed that will essentially contain both a hydrocarbon and NO_2 catalyst, a reference electrode, a working electrode and a counter electrode, and sit on a heated support. This sensor will provide both a signal for NO and O_2.
5. We have initiated construction on 2-electrode test stands to screen a large number of potential NO sensitive materials. The test stand is composed of a high-temperature furnace, a gas mixing panel to mix CO, CO_2, NO, NO_2, SO_2 and hydrocarbons, a chemiluminescence sensor to determine NO and NO_2 concentrations, and a meter to measure the EMF generated.

Status of Milestones

Although this project had a late kick-off, we are ahead of schedule on most of the milestones:

1. Modify current sensor test stand for operation at 800°C (delayed at request of Ford).
2. Test NGK sensor in modified test stand (delayed at request of Ford).
3. Deliver NO_x catalyst assessment and program plan to Ford (completed 6/2002).
4. Construct NO_x electrode test stand (two stands to be completed by August 2002).
5. Deliver report on initial rest results (on schedule September 2002).
6. Design and procure screens for simplified NO_x sensor design (to be completed August 2002).
7. Produce first simplified NO_x sensors for testing (delayed until December 2002).

Communications/Visits/Travel

1. Kick-off meeting held at Ford Scientific Research Labs (4/30/02).
2. Meeting held on 6/10/02 at Ford Scientific Research Labs to report results of literature search and proposed materials development plan.

Problems Encountered

None to date.

Publications

None to date.

Cost-Effective Smart Materials for Diesel Engine Applications

J. O. Kiggans, Jr., F. C. Montgomery, T. N. Tiegs,
and L. C. Maxey
Oak Ridge National Laboratory

Objective / Scope

There are two objectives for this project. The first is to evaluate the cost-effectiveness and maturity of various "Smart Materials Technologies," which are under consideration for diesel engine applications, such as fuel injection systems. The second is to develop "Smart Materials" to be incorporated into working actuators and sensors.

Task 1 – Compositional Alteration of PZT-4

A major task of this project is to develop cost-effective PZT compositions and processing methods that will give PZT powders that will sinter to high density at a temperature below 960ºC. This goal is driven by the need to lower the cost of multilayer PZT actuators by reducing the cost of the interlayer electrodes. Commercial hard PZT powders require sintering at temperatures exceeding 1200ºC and, thus, multilayer devices must use costly Pd/Ag electrodes.

In earlier progress reports we provided data that supports our contention that small additions of bismuth oxide compounds can lower the PZT sintering temperature sufficiently that Ag or Ag/Pd alloy (70/30) can be used as internal electrodes. In the last quarterly report we showed that attrition milled PZT-840 powder containing a sintering aid consisting of 2 wt % Bi_2O_3 with an acceptor ion oxide resulted in a powder that sintered to greater than 99% of the theoretical density after 1 hr at 900ºC. Additionally, the sintered PZT had piezoelectric properties which were as good as the properties of commercial PZT sintered at ~1275^{o}C and, because of the acceptor ion, the electromechanical Q was significantly higher than that of either the undoped powder or commercially sintered PZT-840. This work is continuing and the new results will be reported in a future quarterly.

Task 2 - Multilayer Electroded Laminates

The purpose of this study is to find satisfactory methods for the preparation of PZT laminates with internal electrodes from tape cast materials. Preceding work was directed towards the determination of the optimal conditions for preparing multilayered PZT laminates. We have described in previous progress reports the physical and electromechanical properties of laminates prepared from PZT powders that did not contain any sintering aid. In this current report we focus on laminates that were sintered at temperatures less than the melting point of Ag by incorporating a sintering aid in the PZT powder.

Experimental

Tape Casting

Two methods were used to prepare tape-casting slurries. In the first method, commercial PZT-840 powder (American Piezo Ceramics, Inc.) was mixed with ~2.0 wt % Bi_2O_3 (Alfa Products,

99.8%), an acceptor oxide and the tape casting ingredients using an oblique blender. In the second method, the slurry was also prepared by oblique blending the ingredients, but the PZT-840 had previously been attrition milled for 6 h with the Bi_2O_3 and the acceptor oxide. The composition of the tape casting slurries are given in Table 1

Table 1. Composition of Tape Casting Slurries

	PZT powder		Tape Casting Slurry Composition (wt %)							
Tape ID	ID	Milling	PZT powder	Sintering aid	Xylene	Ethanol	Manhedan Fish oil	Butyl benzyl phthalate	PEG 400	PVB - B98
201	201	none	85.63	2.04	4.43	4.43	0.44	0.79	0.79	1.47
207	206	attrition	71.43	1.70	9.56	9.56	0.60	1.85	1.85	3.46
208	206	attrition	71.07	1.69	9.65	9.65	0.60	1.84	1.84	3.67
210	206	attrition	70.30	1.67	10.0	10.0	0.59	1.82	1.82	3.82

Tapes were fabricated using a Mistler Co. TTC-1000 tape-casting machine. The slurries were cast onto a Mylar film moving at a speed of 20 cm/min. using a 15.25 cm doctor blade adjusted to a thickness of 0.03 cm. The thickness of the dried tapes was 0.02 – 0.025 cm.

Screen Printing

Ag electrodes were applied using a model HC-53 thick film screen printer (Affiliated Manufacturers, Inc). The 325 mesh screens with the electrode patterns were purchased from Hybred Screen Technology. The silver bearing inks were obtained from Metech, Inc. Internal electrodes were prepared by screen printing a circular 2.70 cm OD pattern directly on the dried tapes. Exterior electrodes (Metech 3288) were also a circular pattern (2.40 cm OD) but were applied to the sintered parts. The exterior electrodes were fired onto the part at ~625ºC for 10 min. as recommended by Metech Inc.

Lamination

A metal punch was used to cut 2.7 cm diameter disks from the tapes. The punch was centered on the internal electrode so that the disk was slightly larger than the electrode. Multiple tape laminates were made using the following procedure: six of the electroded pieces were stacked with the electrode surface on top and the stack was covered with a non-electroded PZT piece. Each end of the stack was covered with 2.7 cm Mylar disks and they were heated at 75^{o}C in a 2.7 cm steel die. After one hour heating, the samples were pressed for 10 min. at 6.9 MPa.

The disks were sintered in closed alumina crucibles on a platinum setter with a mixture containing 10 wt % ZrO_2 and 90 wt % $PbZrO_3$ added to control the PbO vapor pressure above the samples. After sintering, the density was measured using the Archimedes method by immersion in ethyl alcohol.

To measure the piezoelectric properties, the disks were poled at 2.0 kV/mm for 10 min. in a silicone oil bath at 120^{o}C. The piezoelectric properties were measured at room temperature after a 24 h stabilization period. Capacitances were measured at 1 kHz and the resonant frequencies of the radial mode were measured using an impedance gain phase analyzer (Agilent 4194A).

The piezoelectric constant, d_{33}, was measured using a Pennebaker model 8000 Piezo d_{33} tester (American Piezo Ceramics)

Results and Discussion

Poor bonding between layers during lamination can result in low sintered density and a reduction in the piezoelectric constants. Table 2 compares the properties of samples formed by uniaxial die pressing with those formed by laminating tape-cast powder without including any interlayer electrodes.

Table 2. Properties of Sintered Die-Pressed PZT-840 and Laminated PZT-840.

Sample		Green Density (% T.D.)[a,b]	Sinter Conditions		Sintered Density (% T.D.)[a]	Piezoelectric Properties			
ID	Type		(ºC)	h		d	d_{33}[c]	k_r	Q_m
245-A	Die Pressed	56.3%	898	3	101.6%	0.40%	0.32	0.61	903
L174A	Laminated	58.8%	898	3	100.5%	0.37%	0.31	0.59	605
250-B	Die Pressed	55.8%	852	3	101.6%	0.38%	0.28	0.58	977
L175A	Laminated	58.8%	852	3	99.3%	0.41%	0.29	0.55	822

a. After removing the binder
b. Based on a theoretical density of 7.6 g/cm^3
c. x 10 $^{-9}$ m/V

The densities for the sintered laminated samples are somewhat lower than those for the sintered die-pressed powder even though the green density, after the binder is removed, is higher for the laminated samples. The lower density coincides with a lower value for both the radial coupling constant (k_r) and the mechanical quality factor (Q_m) in the laminated samples. The cost and the size of the actuator package and its associated electronics dictate the design requirements. The goal of this program is to develop a multilayer device which has a piezoelectric strain constant (d_{33}) of about 0.3 x 10 $^{-9}$ m/V, k_r around 0.5, and a Q_m which is greater than 300. Thus, the properties of the samples laminated without internal electrodes are sufficient to meet the design requirements.

To lower the cost in the multilayer actuator, the PZT active element must sinter to full density below the melting point of silver (960ºC) so that costly, higher melting, Pd or Pd/Ag will not be needed as the interlayer electrodes. Interaction between Ag and the PZT ceramic is reported in the literature. The increase of the vapor pressure of Ag above 960ºC favors silver transport along open porosity in PZT that is not fully dense.[1] Silver migration has been extensively identified during the preparation of multilayer piezoelectric transformers with silver–palladium inner electrodes. Zou[2] showed that a small amount of silver addition changed the electrically conductive process in PMN–PNN–PZT piezoelectric ceramics from nearly complete grain conductivity to grain and grain boundary mixed conductivity. Increased electrically conductivity of the part can reduce the ability to pole the part.

We conducted two types of tests to determine the effects that the Ag electrode has on the piezoelectric properties of attrition milled PZT-840 powder containing the Bi_2O_3-based sintering aid. In the first test, disks formed by uniaxial die pressing were sintered at 900ºC for 0.5 hr and then a test electrode was screen printed on one surface of each disk. The disks with the test electrodes were annealed at 900ºC for an additional 0.5 h or an additional 3.0 h. After the second anneal, a Metech 3288 electrode was fired at 625ºC onto the surface that was not covered with the test electrode. The samples were poled and the piezoelectric properties measured. The results are given in Table 3.

Table 3. Piezoelectric Properties of PZT-840 with Bi_2O_3-Based Sintering Aid after Heating at 900ºC with Metech Ag Electrodes.

	Ag electrode Ink					Piezoelectric Properties			
Sample ID	Metech Product	fritted	Bake Temp[a] (ºC)	Time at 900ºC (h)	Sintered Density (% T.D.)[b]	d	d_{33}[c]	k_r	Q_m
124-D	none	--	--	0.5	101.3%	0.4%	0.31	0.61	939
124-A	3288	yes	550-700	0.5	100.9%	0.5%	0.27	0.49	961
124-B	3571	yes	850-925	0.5	100.9%	0.6%	0.27	0.52	957
124-C	3571UF	no	na[d]	0.5	101.5%	0.5%	0.28	0.53	853
101-D	none	--	--	3.0	nm[e]	0.3%	0.34	0.63	925
101-A	3288	yes	550-700	3.0	nm	0.5%	0.28	0.51	1023
101-B	3571	yes	850-925	3.0	nm	0.4%	0.28	0.55	990
101-C	3571UF	no	na	3.0	nm	0.4%	0.28	0.55	996

a. Metech recommended ~10 min. firing temperature
b. Measured after 30 min sintering; based on a theoretical density of 7.6 g/cm^3
c. x 10^{-9} m/V
d. not available
e. not measured

The effectiveness of the sintering aid is demonstrated by the fact that the parts are fully dense after 0.5 h at 900ºC. Earlier sintering studies have shown that undoped PZT-840 requires temperatures of at least 1125ºC to reach full density.

Three different silver bearing conductor formulations produced by Metech were tested. Comparing the data in Table 3 for the control sample sintered without any electrodes to that for samples sintered with Ag electrodes shows that the Ag electrodes cause a slight degradation of the piezoelectric properties. The formulation in the ink does not alter the piezoelectric properties, even though the 3288 and the 3571 use a mix bonded frit system to improve the adhesion of the electrode to the ceramic. The fact that the properties did not continue to degrade when the anneal time increased suggests that the degradation is caused by a very rapid process or may be concentration limited. Since the test electrodes were not coated with the 3288 after annealing, it is possible that the electrical properties of the test electrodes were degraded. This is

unlikely since the resistances of the test electrodes measured at ~2 cm distance were the same as that for the 3288 electrode.

In the second type of test, we measured the piezoelectric properties of sintered, laminated stacks of PZT-840 doped with the sintering aid. In some laminates the layers were interlaced with Metech 3571UF electrodes. These were formed by laminating layers of tape which had electrodes screen printed on one surface. The results are given in Table 4. The table also gives data for multilayer laminates that were made from attrition milled powder and for laminates of tapes prepared from powder that we had not attrition milled.

Table 4. The Properties of Multilayer Laminates after Sintering under Various Conditions.

Sample ID	Tape Batch	Powder milling	Electrode	Sintering Conditions		Sintered Density (% T.D.)[a]	Piezoelectric Properties			
				Temp (ºC)	Time (h)		d (%)	d_{33}[c]	k_r	Q_m
L136-A	202	none	none	900	3	89.0	0.6	0.28	0.47	764
L151-A	202	none	none	900	12	93.7	0.6	0.28	0.51	771
L155-A	201	none	none	950	3	92.4	0.6	0.30	0.51	606
L158-A	201	none	none	950	12	97.1	0.6	0.30	0.56	754
L171-B	201	none	none	950	18	94.8	0.6	0.33	0.58	524
L171-A	201	none	3571UF	950	18	99.4[b]	0.7	0.28	0.31	313
L182-B	207	attrition	none	900	1	97.7	0.4	0.32	0.54	845
L182-A	208	attrition	3571UF	900	1	102.6[b]	0.7	0.21	0.43	761
L174-A	207	attrition	none	900	3	100.6	0.4	0.31	0.59	605
L194-A	210	attrition	3571UF	900	3	102.6[b]	0.6	0.26	0.53	793
L175-A	207	attrition	none	850	3	99.3	0.4	0.29	0.55	822

a. Based on a theoretical density of 7.6 g/cm^3
b. Including weight of inter-layer electrodes

The laminates made from tape batches 201 and 202, which used powder that had not been attrition milled, were difficult to sinter. Even after heating at 950ºC for 12-18 h the laminate was not fully dense. Laminates prepared from attrition-milled powder, however, sintered to full density after 3 h at 900ºC. These facts are in agreement with the data we presented in the last report concerning the effect of attrition milling on the sintering behavior of uniaxial die-pressed powder pellets. It is apparent that the base powder needs to be attrition milled to reduce the particle size sufficiently that high density can be achieved by sintering at 900ºC.

Laminates prepared from tape batches 207 to 210 were made from attrition milled, doped PZT-840 powder. The piezoelectric constants of the samples without inter-layer electrodes are similar to the constants from die-pressed samples that were sintered without external electrodes. This suggests that the lamination procedure is adequate to assure bonding between the layers of PZT and eliminate interface porosity. There is an increase in the d_{33} of the samples without inter-layer electrodes when the sintering temperature is increased from 850 to 950ºC. There also appears to be an increase in d_{33} for samples with interlayer electrodes as the sintering time at 900ºC is increased. The most significant result is, as we found previously in the external electrode study, that annealing the Ag electrode in contact with the PZT causes a reduction in d_{33} and k_r.

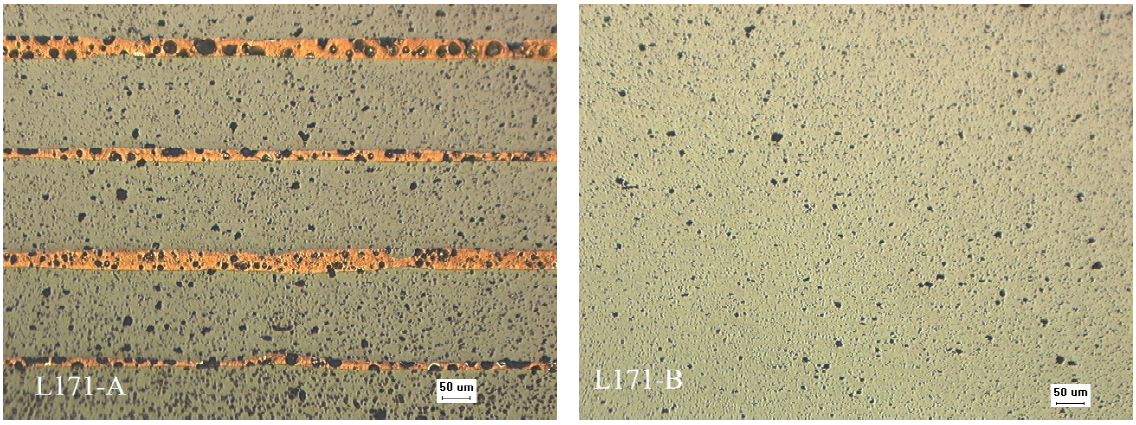

Figure 1. Photomicrograph showing macro structure of laminated PZT-840 containing a Bi_2O_3 based sintering aid prepared from unmilled powder after heating 18 h at 950°C: L171-A has Metech 3571UF interlayer Ag electrodes .

Figure 1 shows the macro structure of the laminates heated at 950ºC for 18 h. Because the sintering temperature was close to the melting point of the silver electrode (962ºC), significant degradation of the interlayer electrodes occurred resulting in porosity in the electrode. Furthermore, since the base PZT powder was not milled, significant porosity is also observed in the ceramic.

An increase in both the density in the interlayer electrodes and the PZT ceramic is observed in the laminates prepared from attrition-milled powder.

Figure 2 shows the structure of the laminates sintered at 900ºC for 1 h. It is clear by comparing the photomicrographs in Figure 1 with those in Figure 2 that there is less porosity in the latter samples. It is also clear that there is little interlayer porosity in the samples laminated without internal electrodes.

A 2000x magnification of the electrode-PZT interface is shown in **Figure 3**. The electrode is dense but two voids are seen at the interface formed by screen printing. Many of these voids were present along the length of the electrode and the majority were along the same interface.

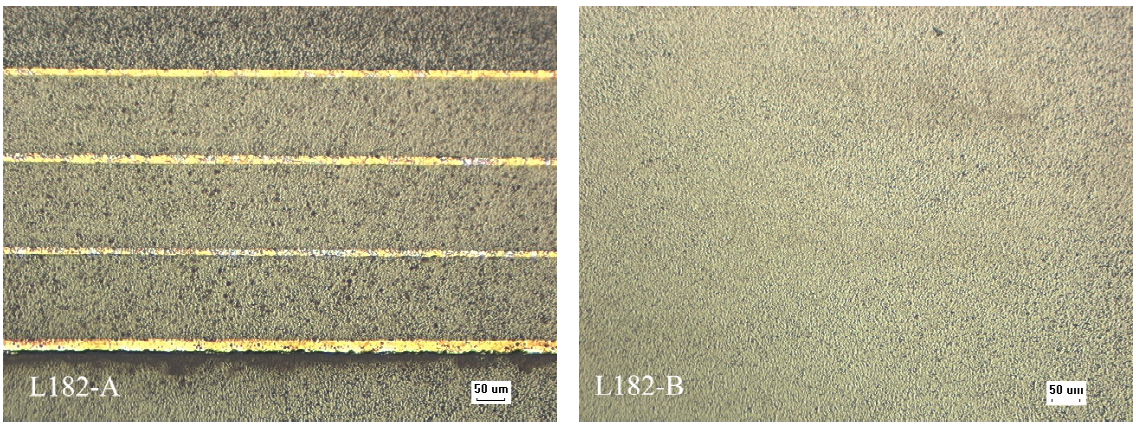

Figure 2. Photomicrograph showing macro structure of multilayer laminates prepared from attrition milled PZT-840 containing a Bi_2O_3 sintering aid after sintering at 90 ºC for 1 h: L182-A has Metech 3571UF interlayer Ag electrodes.

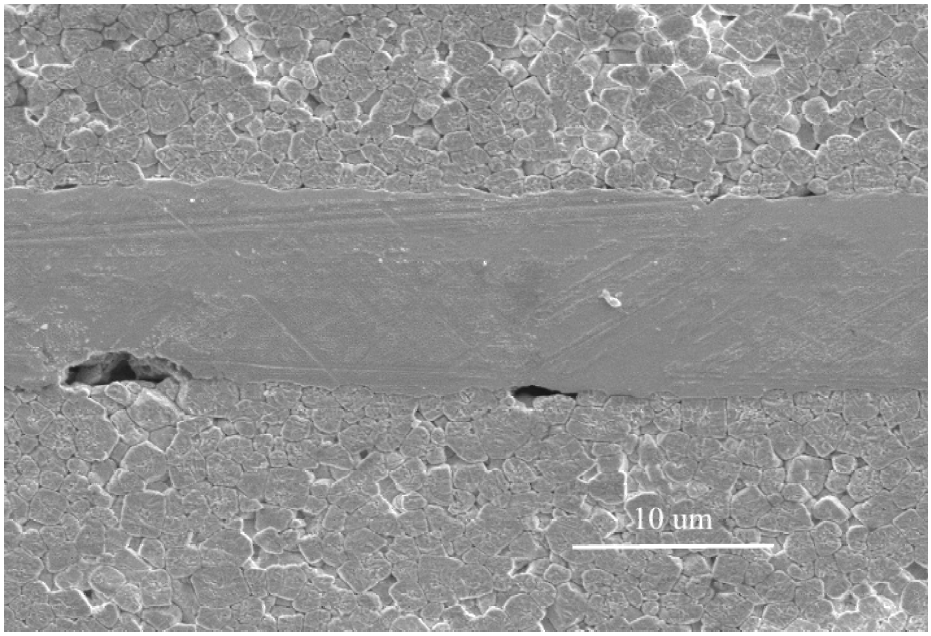

Figure 3. SEM photomicrograph of the interface between an inner Ag electrode and the PZT ceramic 182-A after heating 1 h at 900ºC

Electrodes containing Ag alone without any bonding agents often show poor adhesion until the processing temperature is around 900ºC. At lower temperatures, delamination at the interface or significant interfacial cracking occurs. Ecclestone[3] attributes the improved adhesion at 900ºC to a Ag-PbO eutectic that begins to form from ~820ºC. In his study on the microstructure of the interface between PZT and Ag based electrodes he found some interchange of mass across the metal ceramic bond. Accordingly, we used EDS to probe the chemical composition along the interface in sample L182-A that was heated 1 h at 900ºC. We used a 5-micron EDS sampling box located about 1 micron from the interface. The amount of Ag in the sampling region was below the detection limit for EDS (~0.1 wt %).

Task 3. Static and dynamic testing of flexure amplified piezo stack actuator

A paper study is underway to compare amplifier designs, including both flexural and hydraulic-diaphragm types. There are no results to present in this report.

Status of Milestones

1) Evaluate and characterize commercially available PZT materials. Seek methods to improve the properties of these materials through alternative processing and forming methods. Fabricate new PZT compositions that allow sintering of the PZT materials at lower temperatures.

Status: The evaluations of new commercial materials and low temperature PZT materials planned for this milestone are complete.

2) Fabricate new PZT compositions to seek improvement in the electrical and mechanical properties. More specifically, research work will center on dopants that increase toughness of PZT materials.

Status: Work is underway. Results will be presented in the next reporting period.

3) Use ORNL expertise in motion amplifier devices to design and fabricate motion-amplifying fixtures for fuel injector assemblies. A paper study will be conducted to compare the advantages of fluid-mediated diaphragm amplifiers versus machined, bending structures.

Status: A paper study is in progress. Results will be presented in the next reporting period.

References

[1] Caballero, A. C., *et. al*., J. of Materials Science, 32 (1997) 3257-3262.

[2] Zuo, Ruzhong, *et. al*., Materials Letters, 54 (2002) 185– 190.

[3] Ecclestone, L.J., *et. al*., Electron Microscopy and Analysis Group Conference EMAG99, Sheffield UK, 1999, p55-58.

Low-Cost Manufacturing Processes for Ceramic and Cermet Diesel Engine Components

D. E. Wittmer
Southern Illinois University-Carbondale

Objective/Scope

The purpose of this work is to investigate the potential of low-cost manufacturing processes for ceramic and cermet diesel engine components. The primary task is to develop cost effective processing, forming and sintering methodologies for cermet and ceramic formulations, used by industrial diesel engine manufacturers.

Technical Highlights

Task 1. Collaboration with industrial partner(s).

This task involves the collaboration with industrial partners to assist them in processing and sintering of their diesel engine components. Our goal is provide assistance in processing and sintering which may result in a reduction in surface reactions and part warping. Moreover, this may also provide an alternative sintering process that will allow improved throughput efficiency and manufacturing economy. Due to the proprietary nature of this task, any research data generated from this task is normally controlled by the terms of each specific confidentiality agreement. The reporting of this data and any results are the responsibility of the industrial partner(s).

Task 2. Cost Effective Processing and Sintering of Diesel Engine Components

This task was completed during this reporting period. The resulting work was published in a Masters Degree thesis by Jeffrey A. Hazelwood entitled "Low-Pressure Powder Injection Molding of Intermetallic Bonded Titanium Carbide." Copies of this thesis will be delivered to the contract monitor and program manager.

This task was divided into three major sub-tasks: powder processing, low-pressure injection molding, and sintering. The goal being to develop powder processing that would allow for a homogeneous mixture to be injection molded with a minimum of process defects. This was accomplished in several small batches of intermetallic-TiC powders, where the intermetallic was Ni3Al, NiAlFe, NiCr, or NiCrFe. The intermetallic was investigated as both pre-alloyed or reaction sintered metal powders. A substantial amount of research was accomplished to determine binders and solids loadings to arrive at a mixture that could be injected. The best results were obtained for the binder containing petroleum jelly, paraffin wax, and stearic acid in the ratio of 55:44:1. The injection molding conditions found to produce the best parts were an injection molding temperature of 160°F at a pressure of 60 psi. Following molding, the binder was burned out on a setter powder or in a wicking bed of sand. The resulting bisque parts were then either sintered directly or they were isopressed to 35 ksi prior to sintering. Sintering took place at SIUC and at ORNL. At SIUC sintering took place in the continuous furnace over the temperature range of 1400 to 1450°C and at two belt speeds (0.75 and 1.5 in/min). At ORNL

sintering took place by vacuum, low-pressure hot isostatic pressing (V-LPHIP) at 1450°C. The details of this cycle have been reported previously.

During the development of this formation process, based on low-pressure powder injection molding, large amounts of feedstock were compounded, formed, burned out, and sintered. Through this processing trends were observed that give insight into what types of materials are best suited for this process and what the limitations of this process appear to be.

Feedstocks formed from a very wide range of particle sizes (1 to 45 μm) and varied morphology are best suited for the processes used in this research. These feedstocks yielded smooth low viscosity mixes at a higher solids loading than other feedstocks. The tight particle packing within these feedstocks minimized separation during injection molding and allowed for binder burnout in a wicking bed, without migration of the fine TiC to the part surface. Also, proper wicking of the binder resulted in less free carbon residue in the part which would allow for better wetting of the TiC by the intermetallic during sintering.

The burnout cycle used was based on the TGA analysis of the binder system, followed by trial and error experimentation. The binder burnout proved to be the most difficult stage of this process and the information available in the literature was of little direct help due to the sensitivity of the process to numerous variables. Relative to the published results, the binder burnout cycle used for this research was quite rapid and could account for the low yield rate of several compositions.

Cermets formed from the reaction sintered intermetallics were good candidates for low-pressure injection molding, due to the ability to somewhat tailor their particle size distribution and powder morphologies. Of course one can only tailor these properties within the bounds of the available commercial powders. One disadvantage of cermet materials, from a formation perspective, was their combination of high-density metallic powders and the low-density TiC powder. In some compositions it was observed that a density gradient formed within the feedstock which caused density variation between rods. More significantly, a density gradient is suspected to have occurred during liquid phase sintering of every composition. This gradient resulting from migration of the lower density TiC within the higher density liquid intermetallic during sintering has been attributed with the consistent bowing of rods of each composition.

Several compositions were sintered to high density by both continuous sintering and vacuum, low-pressure hot isostatic pressing (V-LPHIP), resulting in high hardness and fracture toughness. The best density results with the smallest deviation in hardness were obtained by V-LPHIP. This does not rule out continuous sintering as a potential future process, but will depend on application testing to determine the lower limits on the properties that can be used in diesel engine applications. Of additional importance was that nearly all of the 40 vol % TiC-60 vol % intermetallic compositions had a thermal expansion coefficient near that of cast iron and they can be machined by electro-discharge machining. This gives added advantage over ceramics and since they are non-magnetic, gives these materials advantage over iron-based alloys.

In conclusion, the following observations were made:

- Non-iso-pressed V-LPHIP reaction sintered NiAl-TiC rods were formed and processed to a finished state with a higher yield than isopressed or non-isopressed pre-alloyed compositions.

- Both the reaction sintered NiAl-TiC and NiCr-TiC rods achieved higher densities when continuous sintered at 1400°C, compared to 1450°C. Leading one to believe that even better properties may be obtained at lower temperatures.

- Microstructural analyses of every initial test compositions showed that continuous sintered samples had more fine TiC grains than the V-LPHIP sintered samples.

- Initial testing of pre-alloy and reaction-sintered compositions showed that the bimodal systems, containing only a large metallic powder and the fine TiC powder, were unable to be processed to an acceptable finished state.

- Feedstocks containing a very broad particle size distribution of varied morphology are best suited for low-pressure injection molding.

- Slight variations in the particle size of the wicking powders used can drastically affect the binder removal mechanisms.

- Low iso-pressed yields can always be linked to bisque defects.

- The process-limiting defect was sintered deformation in the form of bowing caused by the migration of TiC during the sintering process. Therefore, continuous sintering may offer advantages over V-LPHIP if higher sintering rates can be achieved.

Status of Milestones

1.	Collaboration with Industrial Partners	On Schedule
2.	Cost Effective Processing and Sintering of Diesel Engine Components	Completed

Communications/Visits/Travel

D. E. Wittmer to ISSI-TMS conference in Jackson Hole, WY to make presentation.

Problems Encountered

None

Publications and Presentations

Jeffrey A. Hazelwood, Masters Thesis, "Low-Pressure Powder Injection Molding of Intermetallic Bonded Titanium Carbide," June 28, 2002.

T.N. Tiegs, J.L. Schroeder, P.A. Menchofer, F.C. Montgomery, D.L. Barker, F. Goranson and D.E. Wittmer, "Processing and Properties of TiC-Ni3Al," Structural Intermetallics-2001, ISSI-TMS, pp. 811-818, 2001. (Presented by Wittmer at ISSI-TMS conference in Jackson Hole, WY April 28-May 2, 2002, rescheduled due to 9/11).

Low Cost-High Toughness Ceramics

T. N. Tiegs, F. C. Montgomery, and P. A. Menchhofer
Oak Ridge National Laboratory

Objective/Scope

Significant improvement in the reliability of structural ceramics for advanced diesel engine applications could be attained if the critical fracture toughness (K_{Ic}) were increased without strength degradation. Currently, the project is examining toughening of ceramics by incorporation of ductile intermetallic phases.

Technical Highlights

Previous studies have shown that the properties of the aluminide-bonded ceramics are attractive for diesel engine applications and consequently, development of these materials was started. At the present time, TiC-based composites with 40-60 vol % Ni_3Al are being developed because they have expansion characteristics very close to those for steel. Preliminary wear testing indicated that improved wear resistance could be achieved by decreasing the grain size of the TiC. Achieving fine grain size with the high binder contents is difficult because of the large inter-grain distances. In addition, it was thought that changing the TiC grain shape from a highly faceted one to a more rounded equiaxed grain would reduce localized stress at sharp corners. This, in turn, would improve abrasion resistance from any wear debris. Consequently, grain size refinement is presently being studied. Several approaches can be used to control the final TiC grain size. The methods studied in the present report include: (1) use of additives to change the interface behavior of the growing TiC grains, and (2) reduction of the initial TiC particle size. The development effort is being done in collaboration with CoorsTek, Inc.

Large Batch Processing of TiC-Ni_3Al Composites - The series of large batches (≥2 kg, composition #10) discussed in the previous progress report was continued. In the past reporting period, at least five addition vacuum/low pressure hot isostatic pressure sintering runs were performed and approximately 32 long rod shaped specimens were fabricated. The specimens were isopressed and bisque fired at CoorsTek prior to being returned to ORNL. After sintering, the samples that had high densities (≥ 98 % T. D.) were sent out for machining into test components. Rig testing of the machined specimens will be performed.

As previously reported, compositions to complete the study on effects of additives on the wear properties were fabricated (large batches #14 and #15). The compositions are given in Table 1. The Mo additions have been utilized in the past to improve the flexural strength. The TaC addition has been shown in previous small batches to improve the hardness of the cermets. B_4C has also been shown to improve the hardness of the cermets and boron is a known additive to increase the ductility of the Ni_3Al. Previous work has shown that Fe additions increase the room temperature strength, but more importantly Fe has been shown to be very effective at changing the shape of the TiC grains. These compositions were sintered and fabricated into mechanical test samples. The strength results are summarized in Table 1.

As shown, the strengths for the two recent compositions are both just under 800 MPa. This is a significant drop in strength (typically >1050 MPa), but more importantly, the scatter in the strengths was large. Some strengths were in the 1050 to 1180 MPa range, however, some were also in the 340 to 380 MPa range. The cause for the low strengths is believed due to a coarse batch of TaC powder that was used for these composites that did not get milled effectively. Previous batches of materials that contained TaC had used a different source for the powder. SEM analysis will be done to confirm the origin of the critical flaws.

Alternate Precursors for Ni_3Al Formation - All previous work used a combination of Ni and NiAl for an in-situ reaction to form the Ni_3Al. Because the costs of the starting raw materials can be a significant fraction of the total cost of a component, alternative materials for fabricating the cermets is of interest. Compositions have been mixed and pressed that use just Ni and Al for the reaction synthesis of the Ni_3Al since both of these are reasonable cost raw materials. In addition, an Al-Ni product produced by a catalyst manufacturer in large quantities is being evaluated as a possible raw material. These samples are currently being fired to determine their densification behavior.

Status of Milestones

On schedule.

Communications/Visits/Travel

Travel by T. N. Tiegs to Orlando, FL, June16-20 to attend the 2002 World Congress on Powder Metallurgy and present paper.

Problems Encountered

None.

Publications

None.

Table 1. Summary of large batch processing variables for different TiC- Ni_3Al composites.

Batch No.	Ni_3Al Content (vol %)	Grain Growth Inhibitor (wt %)	TiC Milling Time (min.)	Metal Milling Time (min.)	Flexural Strength (MPa)
#10	50	2% Mo*	90	30	--
#14	50	4% TaC	90	30	798±310
#15	50	1% Mo*, 2% TaC*, 0.1% $B_4C^{\dagger}$, 1% $Fe^{\dagger}$	90	30	790±255

* Percent based on TiC content.

† Percent based on Ni_3Al content.

Direct Rapid Synthesis of Nickel Aluminide, Titanium Carbide, and Their Cermets

Michelle Zeles, Christopher Gump, Joe Spencer, and Alan W. Weimer (PI)
University of Colorado

Introduction

Intermetallics[1,2] are a class of compounds that possess a variety of useful physical and chemical properties for industrial and engineering applications, including greater strength, higher melting points, and better corrosion resistance than common alloys. Whereas alloys are a simple mixture of metals, intermetallics are comprised of definite atomic ratios chemically bonded together into a crystalline lattice, such as Ni_3Al. Some intermetallics are even dubbed "superalloys" because of their extraordinary strength and their high thermal and electrical conductivity. However, their heat resistance and low ductility are similar to ceramic materials[3].

As a superalloy, nickel aluminide (NiAl or Ni_3Al) is a desired intermetallic for a variety of applications, including die-casting and glass making molds, superconductor substrates, diesel engine inserts/pre-burner chambers, incinerator liners, heat exchangers and high temperature/oxidation resistant coatings[4]. Hot pressing these parts requires a fine powder of nickel aluminide. The current method of synthesis, the Exo-Melt™ process, produces a solid brick of nickel aluminide that must be milled into a fine powder[5]. Due to the cost and time associated with this process, it is desirable to develop a process for directly synthesizing powdered nickel aluminide.

Powdered synthesis of nickel aluminide is difficult due to the low melting point of aluminum. When powdered aluminum is heated to its melting point to start a nickel aluminide reaction, the aluminum particles often gather and coalesce into relatively large droplets of aluminum metal and can remain unreacted. The use of diluents may combat the coalescence of aluminum. The purpose of the first half of this research was to investigate whether a nickel aluminide diluent can be used to make powdered synthesis feasible.

The second half of this research involved experiments with titanium carbide (TiC). Currently, TiC is produced to create high-speed cutting tools because of its low density, high toughness, and excellent chemical resistance relative to hard metals. The state-of-the-art for TiC synthesis involves charging a quantity of titanium oxide and carbon to an electric arc furnace. The furnace is heated to 1300^{o}C over a long period of time (because of the large thermal mass involved), where the reaction takes place. The furnace must then cool back to ambient temperature, and the resulting monolith of TiC must be ground to a fine powder. This process is very slow and very energy intensive. Rapid carbothermal reduction using an aerosol transport tube reactor has already been shown to work for the continuous synthesis of boron carbide, and should function equally well for titanium carbide.

The purpose of the research was to create a new process to directly synthesize powdered intermetallics (specifically nickel aluminides), titanium carbide, and cermets of the two materials. The reactions are initially studied in a high temperature Thermogravimetric Analyzer (TGA), and will then be run separately and simultaneously in an aerosol transport tube reactor. In an effort to prevent particle growth and coalescence, diluent materials will be added to the

feedstocks. The process has been named the Thermally Ameliorated Rapid Powder Synthesis (TARPS) process. It is believed that TARPS will reduce the cost and production time for not only TiC and NiAl, but cermets of the two materials as well.

Background

Nickel aluminide is currently used for many facets of industry, the driving reason being its unique combination of properties. Current methods of production involve reacting liquid nickel and aluminum metals. The aluminum melts first, at around 660°C, and then proceeds to react with the nickel. The heat released during the reaction then melts the remaining nickel in the mixture. As the reaction approaches completion, the new intermetallic compound cools to a solid. While this process is very successful in the synthesis of nickel aluminide, it results in a solid brick of NiAl that must be milled into powder.

A carrier material acting as a diluent solves this problem. Union Carbide Corporation[6] developed a way of dealing with such heat and melting issues when synthesizing aluminum nitride from powders. Union Carbide used 30-50% diluent in their processes. A similar method and amount of diluent may be applicable for nickel aluminide. By adding a small amount of nickel aluminide powder to the nickel and aluminum reactant mixture, a desirable effect is achieved. The nickel aluminide already in the mix provides a surface for the molten aluminum to coat, as opposed to the aluminum coalescing into droplets. The added nickel aluminide also serves to absorb some of the heat from the exothermic reaction.

The properties of titanium carbide- low density, wettability, and resistance to wear, make it a good candidate to blend with nickel aluminide. Cummins, Inc. is interested in such cermets for use in diesel engine parts.

Experimental Methods

Part One

Reactions were performed in a Theta Industries thermogravimetric analyzer (TGA). Reactant powders were prepared in both stoichiometric variations of NiAl and Ni_3Al, with powder ratios of 1:1 and 3:1, nickel to aluminum, respectively. The proper diluent (NiAl or Ni_3Al) was added to each powder reactant ratio. Diluent effect was tested with three amounts of diluent - 10, 30, and 50 mole percent. Each experiment was run twice, giving a total of 12 experiments, run in random order. Four runs were done without diluent, two of each NiAl and Ni_3Al.

Powders were prepared by first calculating all needed masses for powders of proper ratios and diluent concentrations. These amounts were measured to milligram accuracy and placed in vials. Each vial was then vigorously shaken for a period of a few minutes. An alumina crucible was used to hold the sample in the TGA. To prevent cracking of the crucible from thermal expansion during the course of the reaction, a small bed of powdered alumina was placed in the crucible. In addition to preventing cracking, it was hoped that the alumina would prevent the nickel aluminide from sintering to the crucible.

For each run, approximately 0.3 g of reactant was heated at 30°C per minute to 700°C. The furnace was then cooled at 30°C per minute back to room temperature. This temperature profile

allowed for just enough heat for the aluminum to melt. Once the aluminum melts, it coats and comes in close contact with the diluent and the nickel and reacts. Aluminum melts at 660°C, therefore 700°C is a sufficient temperature to reach and ensure melting of all the aluminum reactant.

Products were then placed in individual vials and stored for analysis. Products were analyzed by x-ray diffraction (XRD), scanning electron microscopy (SEM) and particle size distribution (PSD). XRD was taken to ensure the abundance of nickel aluminide in the product. SEMs were gathered to examine particle sizes and morphology. PSD displayed the diameter of the particles vs. their percentages.

The results for the initial experiments lead to further testing of the percentage of the diluent used. More experiments were run with 20, 25, 35, and 40 percent diluent for NiAl and Ni_3Al. The same procedure from above was used and the products were analyzed by XRD and PSD.

Part Two

The second set of experiments focused on creating TiC. The final goal was to create a TiC and NiAl cermet. Therefore, for the first trial run the starting reagents were nickel, aluminum, titanium oxide, and carbon black. The reagents were mixed with a ratio of nickel and aluminum equaling 60% of the total mass and titanium oxide and carbon black being 40%. Previous research has used the 40/60% mass ratio for mixing TiC and NiAl[7] and that was the mixture percentage chosen to start from. These starting materials were each weighted out and then titanium oxide and carbon were milled together and the nickel and aluminum were milled together. To create 1 g of mixture, 0.4 grams of the titanium oxide and carbon were mixed in with 0.6 grams of nickel and aluminum. The mixture was then place in crucible in the TGA. No alumina bed was used. The temperature was raised at 30°C per minute to 1400°C and held for 8 minutes.

The product from that run was not the nice TiC and NiAl cermet that was hoped for. A new approach had to be taken. It was decided that only the TiC should be created first and then mixed in with the nickel and aluminum. The starting materials for the TiC reaction were a 1:3 mole ratio of titanium oxide and carbon black. The two materials were milled together over night. About 1 g of the mixture was put into the crucible in the TGA. The temperature rose at 30°C per minute to about 1400°C and held for 15 minutes. PSD was done on the product. The TiC product was larger than expected and the size was not uniform throughout the material.

A new method for creating TiC was devised. It was proposed that mass transfer resistances during the reaction between titanium oxide and carbon lead to the particle growth. To solve the problem titanium oxide and carbon pellets were made. To create the pellets, titanium oxide and carbon were mixed with wheat and cornstarch and milled over night. Water was then added to the dry mixture and then made into pellets by the extruder. The pellets were then dried in an oven for 3 hours at 350°C. Around 2 g of the pellets were placed in the crucible and in the TGA. The temperature program was left the same, 30°C per minute to about 1400°C and held for 15 minutes. The product pellets were then easily crushed into powder with a mortar and pestle.

The next step was to add the nickel and aluminum to the newly formed TiC. To find an optimum mass percent of TiC to nickel and aluminum, different mass percentages for TiC were picked: 10, 20, 30, and 40%. These mass percentages of TiC were mixed in with nickel and aluminum. Four runs were done using 1:1 moles nickel and aluminum and four more runs were done using a 3:1 mole ratio of nickel to aluminum. Each of the mixtures was mixed in a mortar and about 0.5 grams were put into the crucible. The temperature program rose at 30°C per minute to about 700°C and held for 6 minutes. After those samples were run, the next set of eight mixtures was made the same except that diluent was included in the nickel and aluminum mass percentage, 30% molar diluent was added, and then in another set of eight 20% molar diluent was added. PSD was run on all the samples to find the optimum mass percent to create the smallest, uniform product.

Results and Discussion

Part One

A dramatic effect on particle size through use of diluent was observed through SEM. Images showed that particles synthesized with diluent particles were two orders of magnitude smaller than particles synthesized without diluent. The reaction of NiAl with no diluent produced very round particles that appear to have formed through coalescing (Figure 1). This is what was expected to happen if powders were simply heated. The aluminum most likely coalesced with other molten aluminum to produce somewhat spherical particles ranging from 50 to 150 microns. The physical appearance of this product also supported what appears in the SEM. The product resembled small metal spheres, some large enough to gauge their size by the human eye, upwards of 400 microns. The size difference can be attributed to the amount of nickel the aluminum encountered: the larger the particle, the more aluminum that came in contact before reacting.

Nearly the same result is true for the 3:1 ratio product of Ni_3Al. Figure 2 shows the SEM for Ni_3Al with no diluent. Particle sizes are mainly around 50 microns in this sample. This is explained by the increased amount of nickel in the sample. With three times as much nickel as

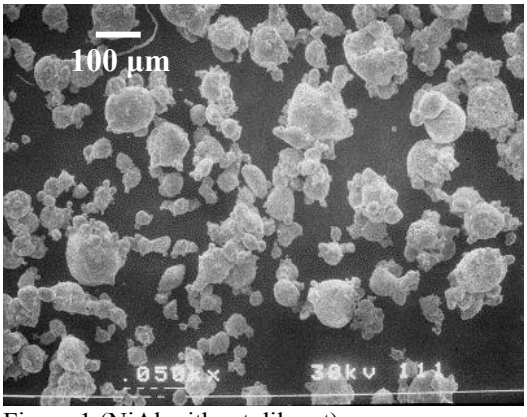

Figure 1 (NiAl without diluent)

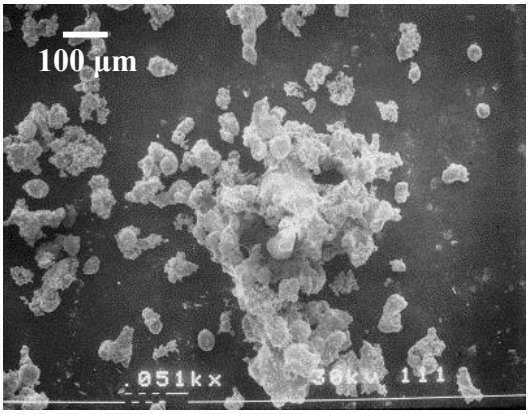

Figure 2 Ni_3Al without diluent.

the previous sample, the nickel acts somewhat as a diluent by providing a surface for molten aluminum to coat instead of coalesce.

Diluent made a drastic difference on the size and appearance of the samples. When diluent was added to 1:1 NiAl the physical appearance changed from small metal spheres to that of a powder. When removed from the crucible, each product was in a small clump. Once a clump was transferred to a vial and shaken gently, the clump was quickly broken up. When NiAl with diluent was shaken it reduced to a fine powder, and the SEM image confirms this (Figure 3). In the SEM, a much smaller group of particles is observed. The diluent has done what was intended and reduced the particle size.

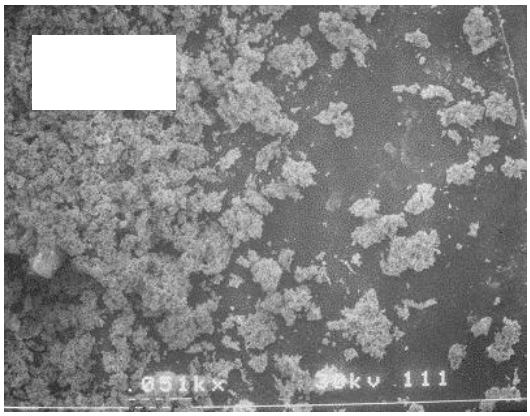

Figure 3 (NiAl with 30% diluent)

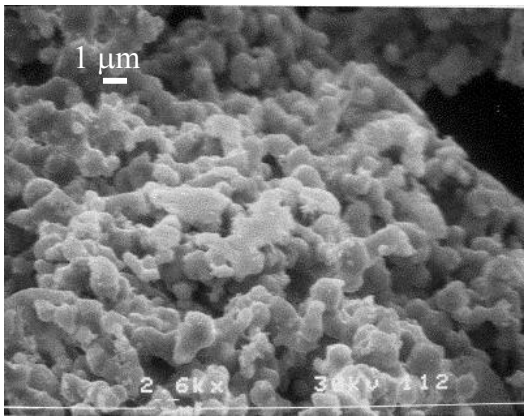

Figure 4 (NiAl with 30% diluent zoom)

Figure 4 illustrates just how much particle size was reduced. This SEM was taken at 2600x magnification of the same sample as Figure 3. With this SEM it can be seen that most particles in the agglomerate are about 1 micron in size. In addition, the large diluent particles are not seen in Figure 3, implying that the diluent material is somehow broken down to smaller particles during the reaction process. XRD analysis for this sample confirmed the identity of nickel aluminide. XRD also indicates some unidentified species. Further investigation will be done to discover the identity of this unknown.

Nickel aluminide in a 3:1 ratio exhibited identical behavior to that of its 1:1 counterpart. When diluent was added to Ni_3Al, particle size was reduced. Figures 5 and 6 show Ni_3Al with 10% diluent added at 50x and 2600x magnification. These agglomerated particles are about 1 micron in diameter as well. This sample was also easily reduced to a fine powder by a series of quick shakes while in a vial.

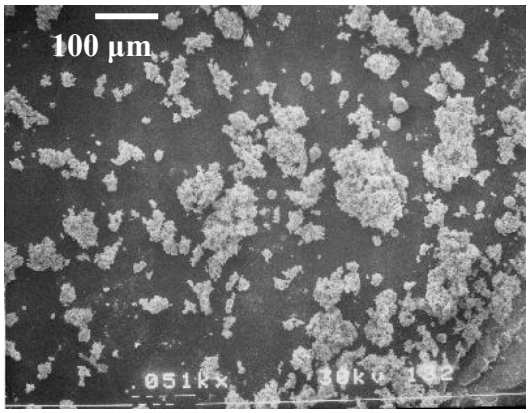

Figure 5, (Ni_3Al with 10% diluent)

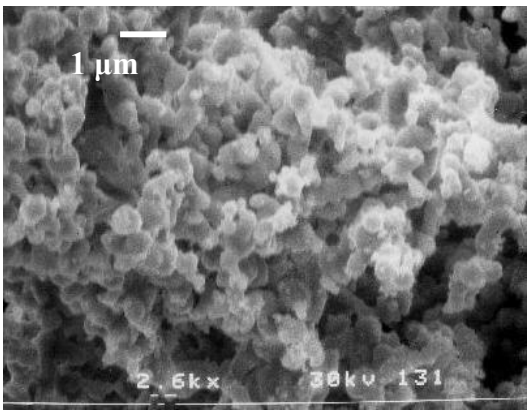

Figure 6, (Ni_3Al with 10% diluent zoom)

SEM micrographs of the remaining samples (Figs. 7 – 10) indicate similar sizing patterns except for 1:1 NiAl with 10% diluent. In that sample it appeared that the amount of diluent added was not enough to overcome coalescing effects of the aluminum. This coalescing is not seen in 3:1 NiAl with 10% diluent, however, and is most likely attributed to the extra surface area provided by the nickel.

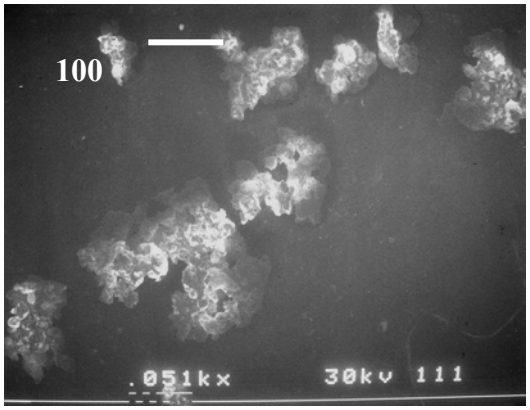

Figure 7, (NiAl with 10% diluent)

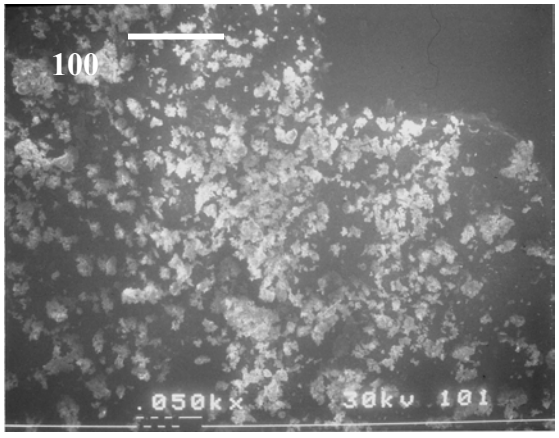

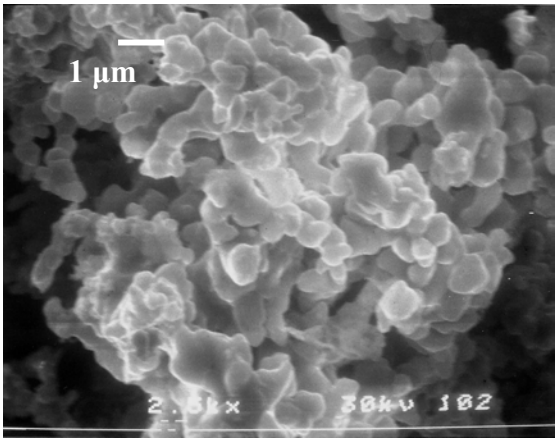

Figure 8, (Ni_3Al 30% diluent)

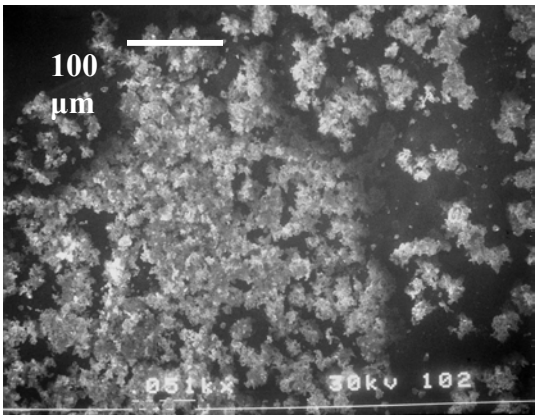

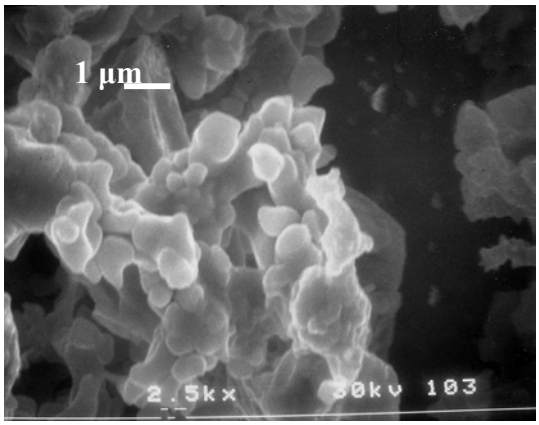

Figure 9, (NiAl 50% diluent)

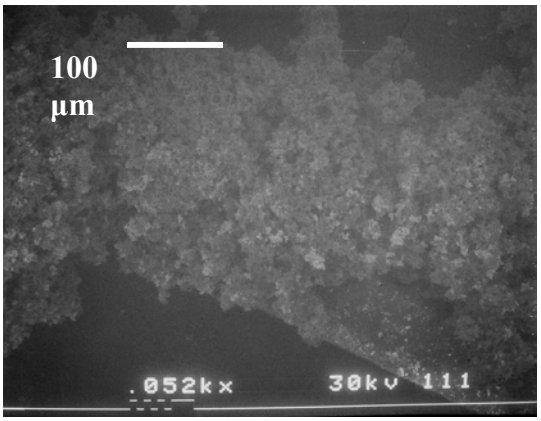

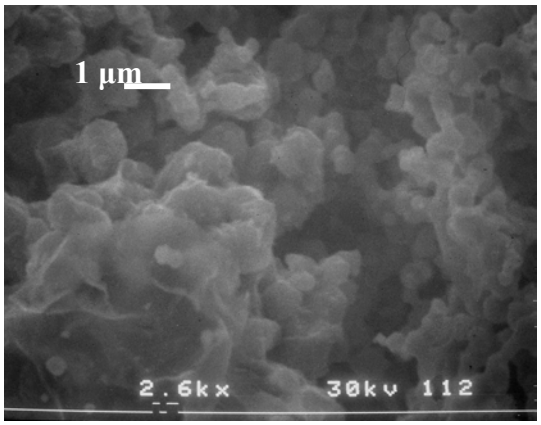

Figure 10, (Ni_3Al 50% diluent)

PSD was run on all the NiAl and Ni_3Al samples. Figures 11-22, all look similar. The product peaks are all centered around 0.4-0.5 microns (in pink). The biggest difference between the PSDs is the tail end from 10 to 100 microns. The tail ends show if there is any unreacted material, or coalescence and growth of the product particles. The nickel and aluminum powders (the feed) used to create the nickel aluminide are very large and have distributions that are very spread out. Adding 30% Diluent to create either NiAl or Ni_3Al seem to work the best. The tails for both graphs (Figures 13 and 19) have very few particles above 1 micron in diameter.

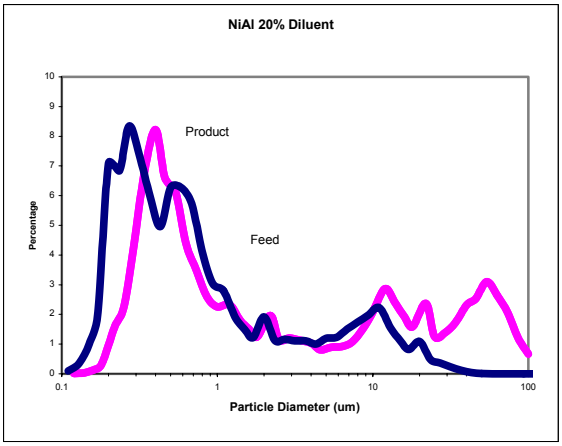

Figure 11

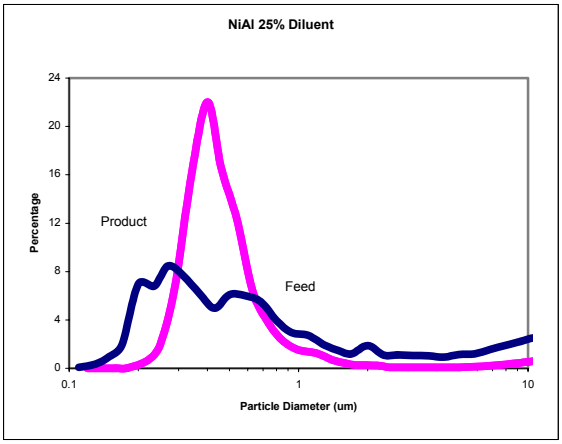

Figure 12

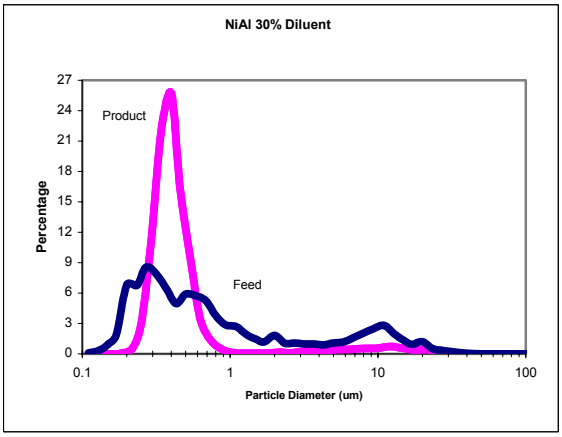

Figure 13

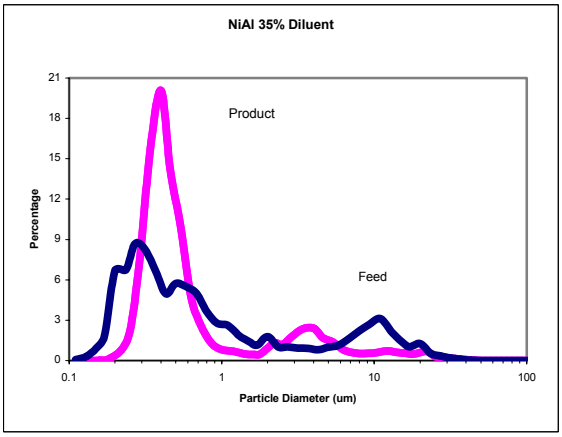

Figure 14

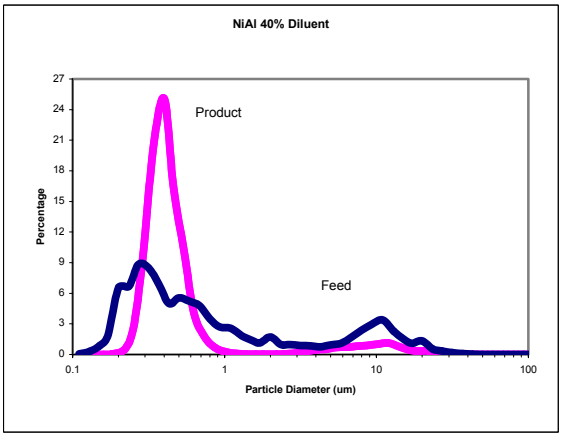

Figure 15

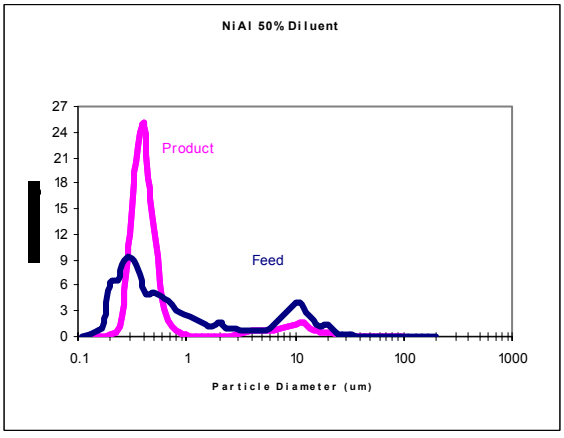

Figure 16

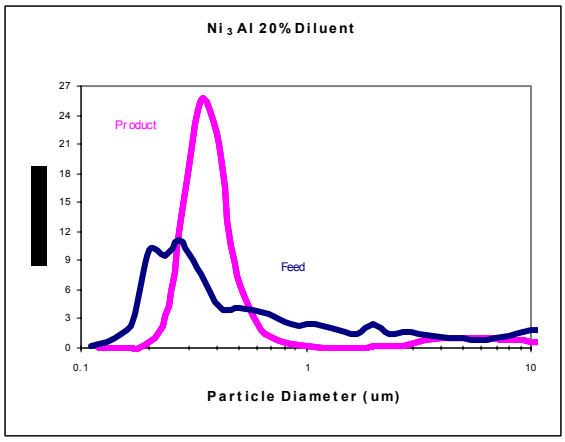

Figure 17

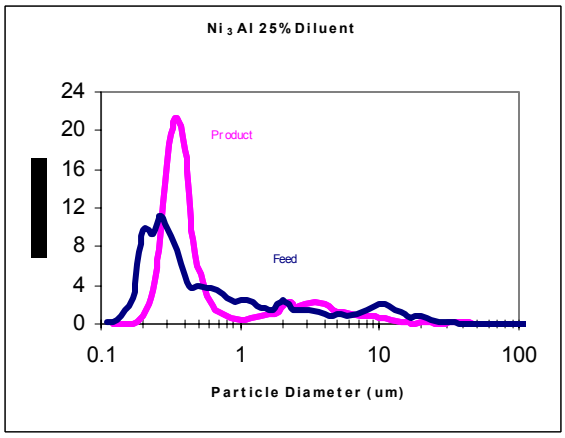

Figure 18

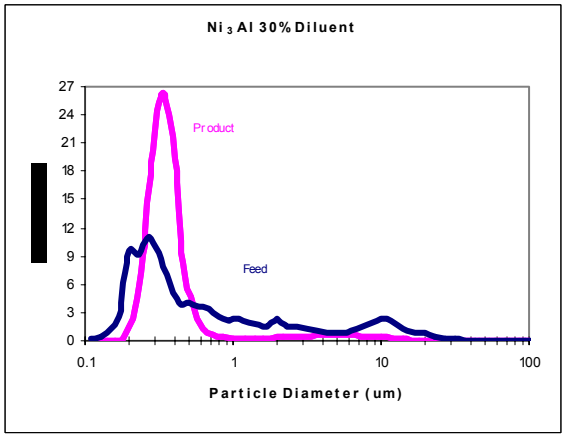

Figure 19

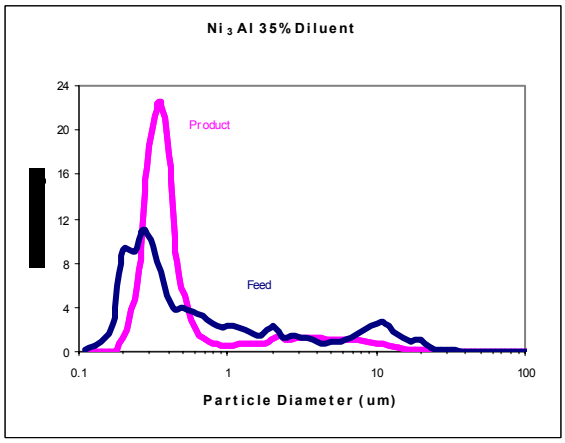

Figure 20

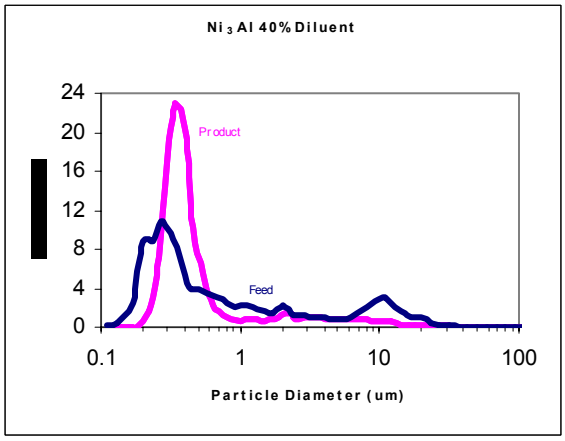

Figure 21

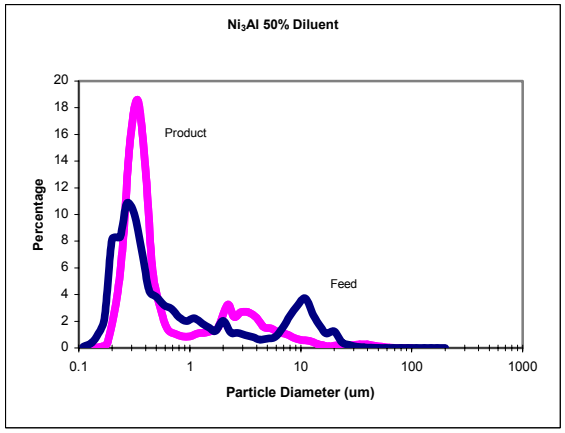

Figure 22

Part Two

The titanium carbide results were fairly straightforward. The first experiment with the titanium oxide, carbon black, nickel, and aluminum was unsuccessful. Only the nickel and aluminum reacted, the titanium oxide and carbon black did not react. This is known because when titanium oxide reacts with carbon, the change in mass is around 40-50%. For this experiment, only a 10% change in mass was observed (see Figure 23). The small change in mass is most likely due to aluminum reacting with some of the titanium oxide. The most probably explanation for the lack of formation of titanium carbide is that as it formed, the nickel aluminide coated the remaining reactants, preventing them from interacting with one another.

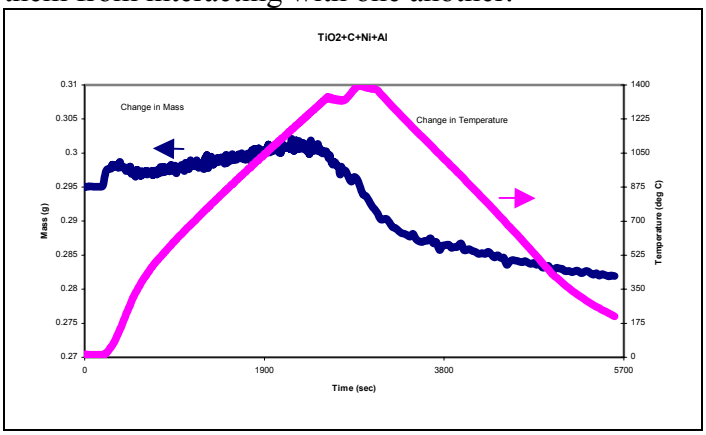

Figure 23 (experiment with TiO_2, C, Ni, and Al)

The mixture of only titanium oxide and carbon black powders in the TGA did create TiC but the particle size was much bigger than the NiAl and the distribution of the size was spread out, Figure 24.

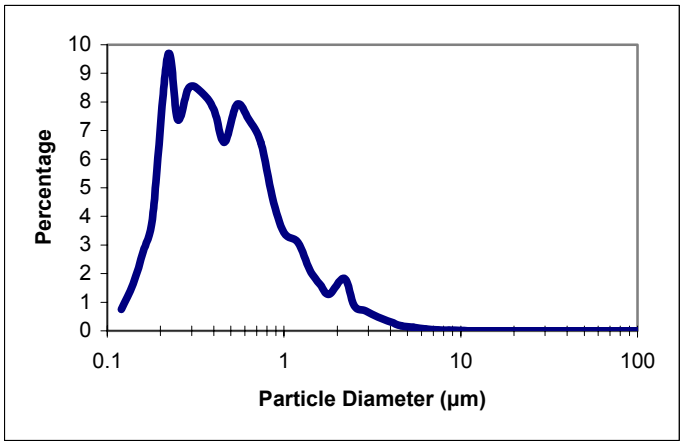

Figure 24 (PSD on TiC created from TiO_2 and C powders)

The TiC created from the pellets created a much smaller size particle. Figure 25 shows that the majority of the TiC created from the pellets have a diameter around 0.4-0.5 µm. These particles are much more uniform in size than the TiC particles created from the powders.

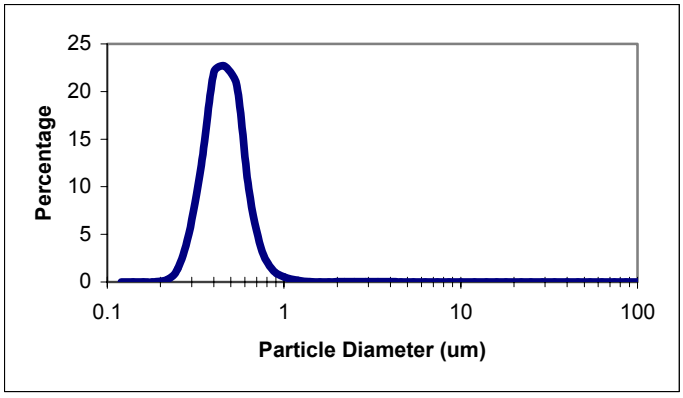

Figure 25 (particle size of the TiC created from pellets)

All of the experiments run with the TiC, nickel, aluminum, and sometimes the diluents were run. The PSD looks almost identical for all the samples involved. It is unclear why the percent of TiC or the addition of diluent made little or no difference in the particle size. XRD and SEM still have yet to be done on these samples, hopefully those results will be more conclusive in displaying a difference between all the mixtures.

Conclusions

The use of a diluent material was found to significantly reduce the size of nickel aluminide product powders. The incorporation of 30% diluent material into the feedstock reduced the size of the product by as much as two orders of magnitude. SEM and PSD confirmed the particle size distribution and morphology. XRD showed that the desired aluminides were being synthesized. It is believed that the diluent provides a surface for the molten aluminum to coat, reducing the growth and coalescence of the product particles. Also, the reaction seems to attack the diluent material, resulting in a homogeneous product that does not show evidence of the larger diluent powder.

In addition, the synthesis of titanium carbide powders was also performed. These powders had a narrow size distribution in the 0.4 – 0.5 micron range. Once synthesized, the TiC can be substituted for the nickel aluminide as the diluent material without triggering greater particle growth. This allows for the creation of a cermet material with submicron homogeneity. However, the initial experiments did not show an optimum concentration of TiC; a wide range of mass percentages produced product powders with very similar particle size distributions. More testing and analysis of the data must be done to understand how the TiC reacts with the nickel and aluminum to produce the cermet and what the optimum amount of TiC is needed.

References

(1) Weimer, A. *Carbide, Nitride and Boride Materials Synthesis and Processing*; Chapman & Hall: London, 1997.

(2) Strnad, Z. *Glass-Ceramic Materials: Liquid Glasses*; Elsevier: New York, 1986.

(3) Cortie, M.; http://www.mintek.ac.za/Physmet/intermet/intro.htm ed.; Council for Mineral Technology, 2002; Vol. 2002.

(4) Ritzert, F.; http://technology.grc.nasa.gov/tech/tops/ms/MS0701.PDF ed.; NASA, 2002; Vol. 2002.

(5) Dunand, D. *Mat. and Manuf. Proc.* **1995**, *10*, 373.

(6) Mandorf, V.: US, 1967.

(7) Keskinen J. *TiC/Ni3Al composites manufactured by self-propagation high-temperature synthesis and hot isostatic press*ing. Journal of Materials Synthesis and Processing (Jul 1999), v 7, 253-258

(8) Choo H. *Thermal residual stresses in NiAl-AlN-Al2O3 composites measure by neutron diffraction.* Materials Science and Engineering A (1999), v 264, 108-121

(9) Deevi Sc. *Exo-Melt™ process for melting and casting intermetallics*. Intermetallics (1997), v 5, 17-27

(10) Fan Q. *Dissolution-precipitation mechanism of self-propagation high temperature synthesis of mononickel aluminides*. Intermetallics (2001), v 9, 609-619

(11) Zang S. *Titanium carbonitride-based cermets: Processes and properties*. Materials Science and Engineering A (1992), v 163, 141-148

Intermetallic-Bonded Cermets

P. F. Becher and S. B. Waters
Oak Ridge National Laboratory

Objective/Scope

The goal of this task is to develop materials for diesel engine applications, specifically for fuel delivery systems and wear components (e.g., valve seats and turbocharger components). This will require materials that have a minimum hardness of 11 GPa and a thermal expansion coefficient of between 10 to 15 x 10^{-6}/°C. The material should also have excellent corrosion resistance in a diesel engine environment, flexure strength in excess of 700 MPa, and fracture toughness greater than 10 MPa$\sqrt{m}$ to ensure long-term reliability. The material should also be compatible with steels and not cause excessive wear of the steel counter face. The upper temperature limit for fuel delivery systems applications is 200°C, and for the other wear applications, the limit is 815°C. Finally, the total material processing costs for these advanced materials should be competitive with competing technologies such as TiN or other ceramic coatings on high-speed tool steels.

Technical Highlights

Studies to assess the potential of new cermet systems are currently being undertaken in collaboration with Dr. Enrique Rocha-Rangel, a post doctoral fellow from the Materials Department at the Autonomous Metropolitan University in Mexico City, Mexico. These studies are evaluating processing approaches to form oxide-based cermets, in particular alumina cermets. In these systems, the wetting of the oxide by the molten metallic phase is the critical hurdle to overcome. Sessile drop studies over the temperature range of 900° to 1300°C in a vacuum of ~ 10^{-3} Pa have been used to evaluate the influence of additives on the wetting behavior of the Al-alumina system. Results show that the equilibrium contact angle between molten Al and alumina is typically ≥ 80 degrees, which results in a non-wetting condition where spreading of the Al is also extremely limited. In the processing of a cermet, this basically means that the liquid Al will not fill the pores in the alumina compact nor conform to the alumina grains. This will produce a microstructure that does not contain a continuous Al phase surrounding the alumina but rather exhibits globular Al regions in a porous alumina matrix. To overcome this, the equilibrium contact angle must be reduced. Sessile drop studies have shown that the presence of carbon substantially reduces the equilibrium contact angle for the Al-alumina system to ≤ 40 degrees and promotes spreading of the molten Al. This approach is being employed to examine the processing of alumina cermets where the binder phase is formed by a reaction sintering processing based on the use of Al as the liquid phase.

Status of Milestones

On schedule

Communication/Visits/Travel

None

Publications

None

Low-Cost Manufacturing of Precision Diesel Engine Components

S.B. McSpadden, Jr.
Oak Ridge National Laboratory

Objective/Scope

- To develop and demonstrate optimized, cost-effective fabrication processes for producing precision components for use in diesel engines.
- To develop and demonstrate optimized, cost-effective, non-destructive testing methods for detecting and preventing machining-induced damage in engine components.

Technical Highlights

Investigation of Non-Destructive Detection of Flaws in Ceramic Components – The Ernst Leitz Scanning Acoustic Microscope (ELSAM) is being upgraded to provide the state-of-the-art capabilities needed to make it a useful instrument for the user program. The upgrade is being performed in three stages and should be complete by late summer. The upgrade provides new computer hardware and software, a new control interface between the instrument and the computer, and on-site training and calibration once the upgrade is complete. Components needed for the upgrade have been ordered and field service representatives are scheduled to begin the on-site work by the end of August. Two small projects are already under way in which the ELSAM will be used to investigate subsurface machining damage in ceramic components.

Tabletop Turning and Machining Centers to Provide New Machining Capabilities – Machining capabilities at the Machining, Inspection, and Tribology User Center have been limited to instrumented grinding. This was appropriate when ceramic materials were our primary concern. However, we frequently receive requests to address machinability issues on metal matrix composites, intermetallics, and other materials where grinding might not be the machining process of first choice. In the past, the cost of procuring, instrumenting, operating, and maintaining industrial-sized machining centers has been prohibitive, and we have been unable to perform experiments involving turning, milling, and drilling. We have recently learned of the availability of relatively low-cost, miniature, tabletop machine tools that have most of the capabilities of full-scale industrial machines. These machines have the advantages of a very small footprint, low initial cost, ease of operation, and extremely low operating and maintenance costs. We plan to procure and instrument a computer-controlled turning center (lathe) and machining center (mill). These machines should be operational by the end of the fiscal year, and will provide much-needed new capabilities for machining research on high-performance materials.

Creep Feed Surface Grinder Update– Once the new creep-feed surface grinder was placed in service, we began experiencing persistent problems with the variable-speed spindle motor controller. These problems were evaluated by the vendor, and a replacement motor and controller of a different design were provided under warranty, at no cost. We also became aware of a problem in balancing heavier, superabrasive grinding wheels when operating them at the higher speeds typically associated with ceramic grinding. This problem has also been resolved and the machine is fully operational. Minor improvements are being made to the instrumentation and control software. These changes will provide the capability to automatically measure and

log coolant pressure and flow rate, and to precisely control the collection of force data from the dynamometer.

Communications/Visits/Travel
None.

Publications
None.

Cylindrical Wire Electrical Discharge Machining (EDM) and Temperature Measurement

Albert Shih
University of North Carolina

Objective/Scope

To develop precise, efficient, and cost-effective cylindrical Wire Electrical Discharge Machining (WEDM) process for cermet and other electrically conductive advanced engineering materials, and temperature measurement methods for grinding and diesel exhaust aftertreatment devices.

Technical Highlights

Most of the effort this quarter is concentrated on developing temperature measurement methods for diesel exhaust aftertreatment filters. As mentioned in the last quarterly report, a system with angled sapphire fiber and a PbS/PbSe infrared sensor has been assembled. This system is set up and calibration method was developed. This quarterly report covers most of the calibration method. Preliminary experiments on measuring temperature in microwave-heated filters, provided by Industrial Ceramic Solutions at Oak Ridge, TN, have been conducted.

The configuration of temperature measurement system and setup for calibration are first presented. Key theory of radiation ratio thermometry is then introduced and procedures are developed. Results from system calibration are discussed.

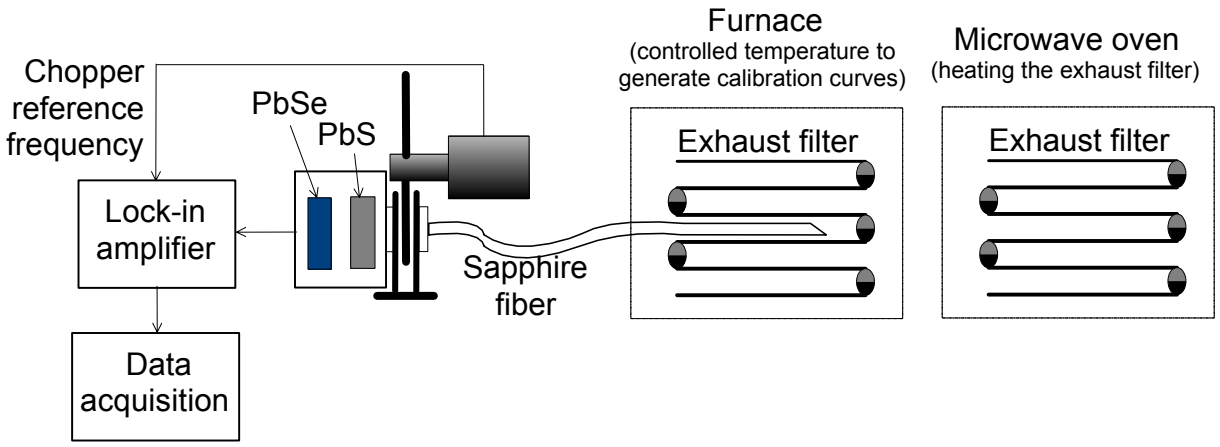

Fig. 1. Schematic temperature measurement system setup

System Configuration

Figure 1 shows the schematic of the setup for infrared-based temperature measurement for diesel exhaust aftertreatment filters. A flexible sapphire fiber, which has a 45 degree angled tip and does not interfere in the microwave field, harnesses the infrared signal from the filter wall in the calibration furnace or microwave heater to the PbS/PbSe infrared sensor.

The semiconductor detectors can be categorized into photodiode (or photovoltaic) and photoconductor. The photodiode detector, such as the Si-based detector used for grinding temperature measurement, operates in DC mode. The detector's DC voltage output is related to the intensity of thermal radiation and temperature. On the contrary, the photoconductor detector

operators in AC mode and requires a mechanical chopper to modulate the light input. Photodiode detectors allow a simple hardware configuration. However, the photoconductor detectors, particularly the PbS and PbSe used in this research, can detect far wavelength infrared signal (2 to 4 μm for PbS and PbSe). This enables the measurement of temperature between 200 to 800ºC, which is typical operating temperature range for diesel exhaust filters.

In Fig. 1, the mechanical chopper optically interrupts the radiation flux input at a fixed frequency and generates AC signals for the PbS and PbSe detectors. The voltage outputs from the PbS and PbSe detectors can be conditioned by a potentiometer, filtered and amplified by lock-in amplifiers, and/or recorded by an oscilloscope or data-acquisition system. The combination of these techniques can be used, which has increased the complexity of this research. If the lock-in amplifier is used, the chopper transmits a reference chopping frequency to the amplifier.

A bias current is required in photoconductive detector. Associated with the chopping frequency f, a dominant noise proportional to $1/f$ is presented at low frequencies [1]. The photoconductive detector operates in AC or synchronous mode to suppress the $1/f$ noise. The background noise, detector noise, and offset of the DC signal are also suppressed by operating in the AC mode. The lock-in amplifier extracts the modulated signal from the detector and suppressed all non-synchronous noise or noise components out of phase with the modulated signal. This results in a signal-to-noise improvement of many orders of magnitude.

Setup for Calibration

Figures 2(a) and 2(b) illustrate the sapphire fiber, sensor, chopper, thermoelectric cooling controller, sensor power supply, chopper control, lock-in amplifier, and furnace in a setup for calibration. The exhaust filter was first placed deep inside of the furnace (Fig. 2(c)). The furnace temperature can be set and controlled constant in a range from 100°C to 1000°C or even higher. The small window glass in the front of the furnace was removed to insert the sapphire fiber and a type K high temperature thermocouple into the filter cavity. The window was covered by Al_2O_3 fiber for insulation (Fig. 2(d)). Since the heat leakage occurs in the window area, a temperature gradient exists in the furnace. To minimize the effect of the temperature gradient, after the furnace reaches the thermal equilibrium at each setup temperature after about an hour, the temperature distribution along a filter cavity was measured by moving the thermocouple. Meanwhile, the detector outputs were recorded by oscilloscope. The temperature of the furnace is increased to the point when the detectors start to generate detectable voltage signal, about 150ºC for PbS and 200ºC for PbSe. This is the starting temperature. About 3 to 4 temperature and sensor voltage readings are recorded every 100 ºC until the sensor signal is saturated or reached 900ºC.

As shown in Fig. 2(a), a thermo-electrical cooling is used to cool the sensor to increase its sensitivity and a two-channel oscilloscope is used to record the DC voltage from both PbS and PbSe detectors. A filter heated in the furnace is shown in Fig. 2(e).

Two-color radiation ratio thermometry

The radiation ratio thermometry is used to process signals acquired from the PbS/PbSe sensors and convert into temperature. The thermal radiance emitted by filter surface near the tip of the sapphire fiber is transmitted to the PbS/PbSe sensors. Two distinct spectral regions, 2.7 μm for

PbS and 3.2 μm for PbSe, were detected by the two detectors. The ratio of these two detector outputs was used to measure the temperature.

The emissive power from a blackbody is described by Planck's distribution law [2].

$$E_{\lambda,b}(\lambda,T)=\frac{C_1}{\lambda^5(e^{\frac{C_2}{\lambda T}}-1)} \tag{1}$$

where the first and second radiation constants are C_1=3.742×10^8 W · μm^4/m^2 and C_2=14390 μm · K, and T is the absolute temperature (K). When λT<<C_2, it can be approximated by Wien's law [2] and is of the form

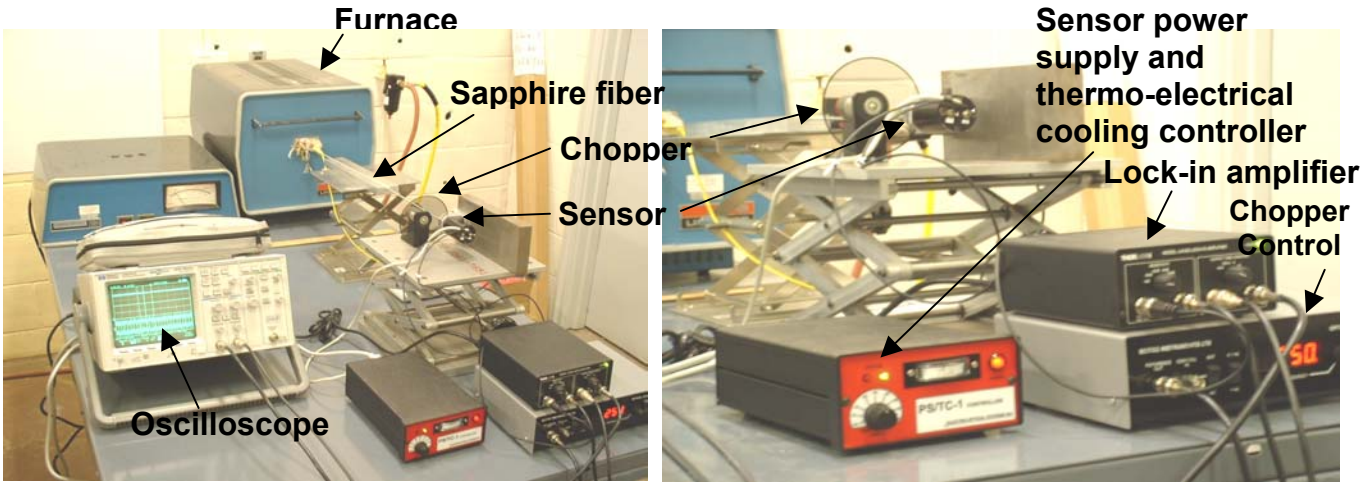

(a) (b)

(c) (d) (e)

Fig. 2. Setup for sensor calibration system

$$E_{\lambda,b}(\lambda,T) = \frac{C_1}{\lambda^5} e^{-\frac{C_2}{\lambda T}} \tag{2}$$

After scaled by the emissivity $\varepsilon(\lambda,T)$ of the emitting surface and the transmissivity $\tau(\lambda, T)$ of the intervening medium or window, the radiance arriving at the detector is

$$b(\lambda,T) = C_1 \tau(\lambda,T)\varepsilon(\lambda,T)\lambda^{-5} e^{-\frac{C_2}{\lambda T}} \tag{3}$$

The response of the detector to the thermal infrared radiance is a voltage [3] given by,

$$V(\lambda) = g(\lambda) b(\lambda,T) \tag{4}$$

where $g(\lambda)$ is the gain or detector's spectral electrical response constant to radiation at wavelength λ. Substituting Eq. (3) into Eq. (4), it follows that

$$V(\lambda) = C_1 g(\lambda)\tau(\lambda,T)\varepsilon(\lambda,T)\lambda^{-5} e^{-\frac{C_2}{\lambda T}} \tag{5}$$

In ratio thermometry, the target temperature is inferred from the ratio of signals received by the thermometer at two different wavelengths.

$$\frac{V_2(\lambda_2)}{V_1(\lambda_1)} = \frac{g_2(\lambda_2)\tau(\lambda_2,T)\varepsilon(\lambda_2,T)\lambda_2^{-5} e^{-\frac{C_2}{\lambda_2 T}}}{g_1(\lambda_1)\tau(\lambda_1,T)\varepsilon(\lambda_1,T)\lambda_1^{-5} e^{-\frac{C_2}{\lambda_1 T}}} \tag{6}$$

Taking the natural logarithm of both sides,

$$\ln(\frac{V_2(\lambda_2)}{V_1(\lambda_1)}) = \ln(\frac{g_2(\lambda_2)}{g_1(\lambda_1)}) + \ln(\frac{\tau(\lambda_2,T)\varepsilon(\lambda_2,T)}{\tau(\lambda_1,T)\varepsilon(\lambda_1,T)}) - 5\ln(\frac{\lambda_2}{\lambda_1}) + \frac{C_2}{T}\frac{\lambda_2-\lambda_1}{\lambda_1\lambda_2} \tag{7}$$

In Eq. (7), λ_1 and λ_2 are known. $g_1(\lambda_1)$ and $g_2(\lambda_2)$ are constants provided that detectors' temperature is not affected by ambient temperature variation, which can be practically achieved by the utility of thermo-electrical or liquid nitrogen cooling to the small and sealed detector cavity. $V_1(\lambda_1)$ and $V_2(\lambda_2)$ can be measured. Ideally, if the assumption of a gray target and gray intervening media is applicable, $\varepsilon(\lambda_1,T)=\varepsilon(\lambda_2,T)$ and $\tau(\lambda_1, T)=\tau(\lambda_2, T)$, then the second term on the right side of Eq. (7) is 0.

In practice, the gray assumption doesn't hold in most cases, and the logarithm term composed of $\varepsilon(\lambda_1,T)$, $\varepsilon(\lambda_2,T)$, $\tau(\lambda_1, T)$, and $\tau(\lambda_2, T)$, in Eq. (8) is also difficult to determine within sufficient accuracy in many cases. Attempts are made to overcome this by choosing the wavelength λ_1 and λ_2 as close as possible. As long as the emissivity ε and transmissivity τ do not sharply change within the selected narrow wavelength region, i.e., $\varepsilon(\lambda_1,T)=\varepsilon(\lambda_2,T)$ and $\tau(\lambda_1, T)=\tau(\lambda_2, T)$, the

second term on the right side of Eq. (7) is still close to 0. Thus the following simplified equation may give a reasonable estimation for temperature measurement.

$$\ln(\frac{V_2(\lambda_2)}{V_1(\lambda_1)}) = \ln(\frac{g_2(\lambda_2)}{g_1(\lambda_1)}) - 5\ln(\frac{\lambda_2}{\lambda_1}) + \frac{C_2}{T}\frac{\lambda_2 - \lambda_1}{\lambda_1\lambda_2} \quad (8)$$

For better accuracy, a system calibration is required to compensate the variation of ε and τ.

Calibration results

The scheme of system calibration and temperature measurement is shown in Fig. 1. The exhaust filter was first put into a furnace to generate calibration curves, which builds the relationship between the voltage ratio on the left side of Eq. (7) and the absolute temperature T and other terms on the right side of Eq. (7). After the calibration data was obtained, a high order polynomial was used to fit the data. An example of calibration curve is given in Fig. 3.

Figure 3(a) shows different voltage outputs between the two channels of PbS and PbSe. This is due to the PbS/PbSe sandwiched sensor configuration, different amplification gain and sensitivity of the detector materials. PbSe is less sensitive and outputs a lower voltage. PbS can detect low temperature but is likely to saturate the sensor or amplifier output at high temperatures.

Results of the logarithm of the ratio of voltage outputs from the two detectors are shown in Fig. 3(b). The value of the ratio is not unique across the 200 to 900°C range. The ratio curve peaks at about 380°C. Efforts have been made to extend the detection range to lower temperature by adjusting the amplification gains of both PbS and PbSe channels. The results of different system responses under different gain adjustment to both PbS and PbSe channels will be described in the next quarterly report.

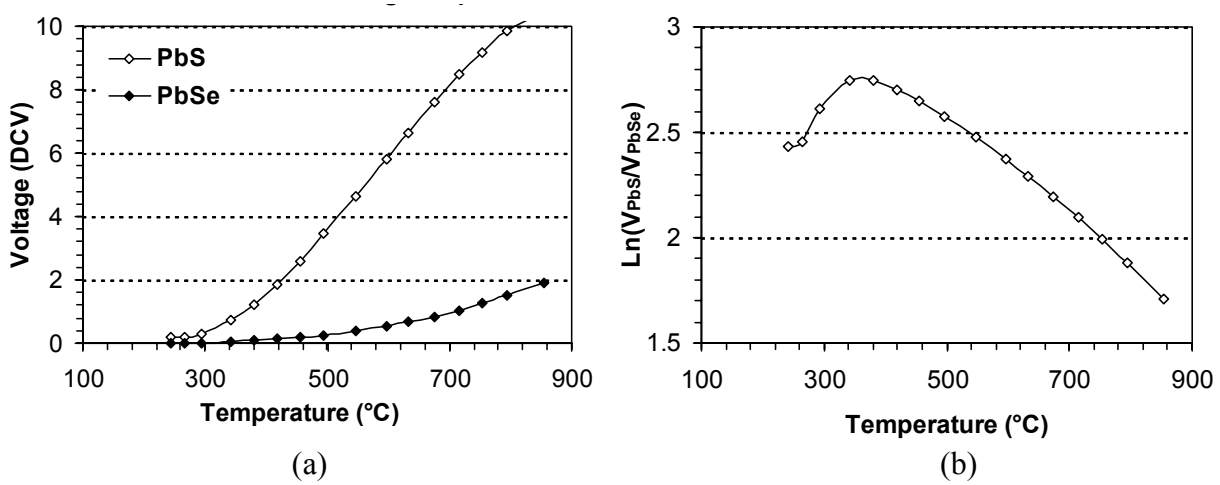

(a) (b)

Fig. 3. Typical calibration curve (a) voltage output of PbS and PbSe (b) ratio

Status of Milestones

Milestone 1: Develop process technology to achieve high material removal rate in cylindrical WEDM of advanced engineering materials.

Status: Three journal and two conference papers have been published or accepted on this research.

Milestone 2: Determine the level of form tolerances and surface finish achievable by the cylindrical WEDM.

Status: Nothing to report. The surface finish was as low as 0.68 μm Ra, comparable to rough grinding, for the carbide materials.

Milestone 3: Prototype needles, armature pins, and plungers for diesel engine fuel injectors.

Status: Currently working with Cummins Technical Center to transfer the technology of cylindrical wire EDM for the roughing operation in prototype plunger manufacturing.

Milestone 4: Develop mathematical models for material removal rate and surface finish of the cylindrical WEDM.

Status: The mathematical models for material removal rate and surface finish have been derived. These results have been summarized in two technical papers.

Milestone 5: Characteristics of the recast layer after WEDM and cylindrical WEDM and the surface condition after abrasive blasting.

Status: Nano-indentation tests have been applied to quantify mechanical properties of cylindrical wire EDM surface layers on WC-Co workpiece. Micro SiC abrasive blasting of the recast layer was demonstrated to improve the surface finish of WC-Co by about 40%~60%. These results are summarized in two technical papers.

Milestone 6: Development of the optical fiber based temperature measurement method, with applications for grinding process and diesel exhaust aftertreatment filters.

Status: The temperature measurement system was adjusted and improved. Based on the theory of two-color radiation ratio thermometry, a diesel exhaust aftertreatment filter was placed in a heavy-duty heating furnace for measurement system calibration.

Communications/Visit/Travel

May 15-16: Visit to Porvair and ORNL. Albert Shih and Ron Scattergood visited ORNL and gave a presentation to update our research.

June 25-27: Visit to Cummins and ORNL. Albert Shih visited Cummins Technical Center and identified the possible application of the developed infrared-based method to measure surface temperature for NO_x filter and the potential technical transfer of the cylindrical wire EDM technology for prototype cermet plunger manufacturing.

Publications

SiC grinding of zirconia and grinding temperature measurement:

- A.C. Curry, A.J. Shih, R.O. Scattergood, and S.B. McSpadden, "Grinding Temperature Measurements in MgO PSZ Using Infrared Spectrometry," *J. Am. Ceram. Soc*. (accepted)

- A.J. Shih, R.O. Scattergood, A.C. Curry, T.M. Yonushonis, D.J. Gust, M.B. Grant, S.B. McSpadden, "Grinding of Zirconia using the Dense Vitreous Bond Silicon Carbide Wheel," Journal of Manufacturing Science and Engineering (submitted).
- A.C. Curry, A.J. Shih, R.O. Scattergood, S.B. McSpadden, and R.B. Dinwiddie (2001) "Infrared Spectrometry for Grinding Temperature Measurement," *2001 ASPE Annual Meeting*, Crystal City, VA.

Cylindrical wire EDM:

- J. Qu, A.J. Shih, and R.O. Scattergood (2002) "Development of the Cylindrical Wire Electrical Discharge Machining Process: Part I: Concept, Design, and Material Removal Rate," *ASME Journal of Manufacturing Science and Engineering*, Vol. 124, No. 3, pp. 702-707.
- J. Qu, A.J. Shih, and R.O. Scattergood (2002) "Development of the Cylindrical Wire Electrical Discharge Machining Process: Part II: Surface Integrity and Roundness," *ASME Journal of Manufacturing Science and Engineering*, Vol. 124, No. 3, pp. 708-714.
- J. Qu, A.J. Shih, R.O. Scattergood, and S.B. McSpadden (2001) "Cylindrical Wire Electrical Discharge Machining Process Development," *2001 ASPE Annual Meeting*, Crystal City, VA.
- J. Qu, A.J. Shih, and R.O. Scattergood (2001) "Development of the cylindrical wire EDM process," Symposium of Nontraditional Manufacturing Research and Applications, *2001 ASME IMECE* New York, NY.
- J. Qu, L. Reister, A.J. Shih, R.O. Scattergood, E. Lara-Curzio, "Nanoindentation Characterization of Surface Layers of Electrical Discharge Machined WC-Co," *Materials Science and Engineering: A* (accepted).
- J. Qu and A.J. Shih, "Analytical Surface Roughness Parameters of an Ideal Profile Consisting of Elliptical or Circular Arcs," *Precision Engineering* (submitted).
- A.J. Shih, J. Qu, R.O.Scattergood, and J. Luo, "Abrasive Micro-Blasting of Surface Layers of Electrical Discharge Machined WC-Co Composite," *2003 Wear of Materials Conference* (submitted).

Remark

Under the support of this project, Jun Qu has received his Ph.D. degree from NC State University in April 2002. He is now a post-doc research fellow at Oak Ridge National Laboratory.

References

[1] E.L. Dereniak and D.G. Crowe, *Optical radiation detectors*, John Wiley & Sons, 1984, pp. 86–106.

[2] D.P. Dewitt and G.D. Nutter, *Theory and Practice of Radiation Thermometry*, John Wiley & Sons, 1989, pp. 25–50.

[3] D. Ng, 1998, "Self Calibration of a 2-wavelength Pyrometer," NASA/TM-1998-208808.

NDE/C Technology for Heavy Duty Diesel Engines:
Fuel Delivery and Insulating Materials

W. A. Ellingson, C. Deemer, and M. Shields
Argonne National Laboratory
in cooperation with
A. Parikh
Illinois Institute of Technology

Objective/Scope

The objective of the work in this task, part of the Testing and Characterization research area of the Heavy Vehicle Propulsion System Materials Program, is to develop enabling nondestructive evaluation/characterization (NDE/C) technology for lower cost and high performance materials. Specifically, this project addresses development of advanced NDE/C technology for; (a) advanced fuel delivery systems (including injector nozzles), and (b) insulating materials for reducing heat losses in the combustion zone. Fuel delivery systems for heavy-duty diesel engines are complex, very expensive and represent a significant portion of the cost of a heavy vehicle diesel engine. High pressures inside these fuel delivery systems contribute to poor fuel delivery and hence poor emissions. Materials development is part of Goal 3 of the heavy vehicle propulsion materials program. Insulating materials are also a significant materials development area because of the improvement in engine efficiency if reduced heat losses can be obtained. NDE/C technology that can provide information for reliable cost production and engine component surveillance would be of benefit to reaching the goals.

Technical Highlights

The technical highlight this period is that we have refined the laser scatter technique by increasing sensitivity to both surface and subsurface cracks. Further, investigations are underway to determine the optimal angle for the optical back-scatter parameters. As noted last period, we have continued in our efforts to develop an analytical model for the back-scattered laser effort so that we might begin to be able to predict effects of different subsurface defects on the resulting back-scattered laser data.

Technical Progress

The efforts this period have been on refining the angle for the optical laser scatter NDE method for evaluating oxide monolithic ceramic fuel metering plungers (see Quarterly Progress Report January – March 2002). The development of this technique for application to ceramic fuel metering plungers has been two-fold: (A) increasing the power of the incident light though application of a higher power laser and setup modification, and (B) optimization of the method parameter, specifically the incident-scatter angle from elastic electro magnetic theory.

A. Experimental Setup Modification

This period we have installed a more powerful laser – a class 3b laser. This is a 35 mW He-Ne (632.8 nm wavelength) randomly polarized laser. As before, the laser light was focused directly onto the ceramic fuel injector nozzle at an angle of 11° off the sample's surface normal. The intensity of the light scattered off the sample was measured at an angle of 11° ± 0.7° by focusing the reflected light on to an optical power meter. The integrated intensity of the back-scattered

light between 4° and 18° off the surface normal was converted to optical power with a digital optical power meter and monitored with a PC. Figure 1 shows a schematic diagram of the experimental set up.

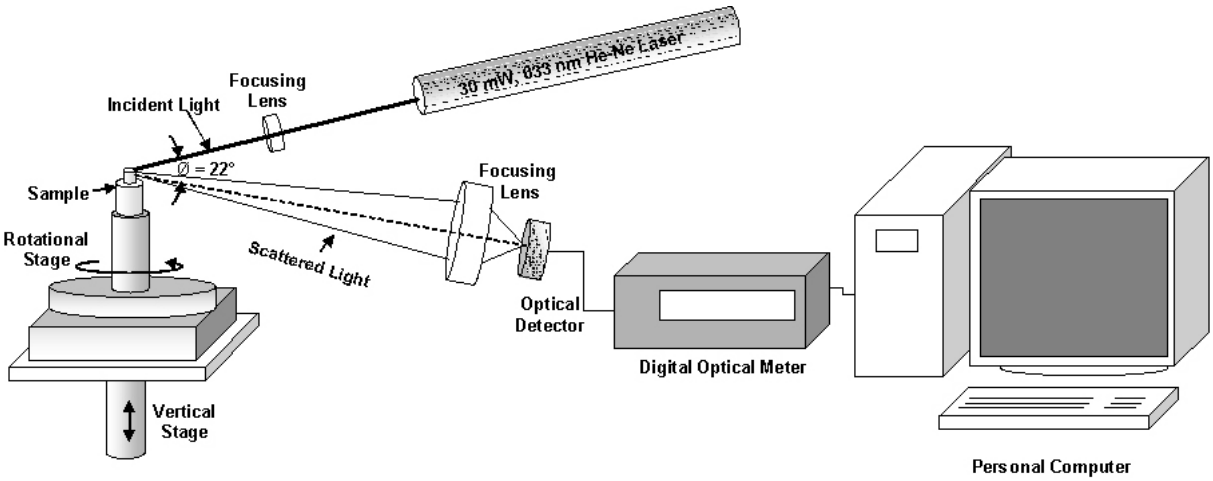

Fig.1. Schematic diagram of the angle elastic optical back-scatter experimental setup.

The ceramic fuel injector nozzle is mounted in a custom-made clamping device. This in turn is mounted on the computer-controlled rotational stage. The vertical position of the measurement point on the ceramic fuel injector was manually controlled with a vertical positioning stage. This vertical motion stage was also added this period. The addition of the vertical motion stage allowed back-scatter power measurements to be raster scanned both angular and vertically.

Experimental Results

Optical back-scatter power scans were acquired from a Cummins Engine Company MgO monolithic ceramic fuel-metering plunger. Optical photomicrograph of the top face of the plunger (see Fig. 2) shows three surface-breaking cracks. Figure 3 shows a resulting scan where Figure 3a is a single line scan and Figure 3b is the "area" scan of the entire upper surface. You will note the huge improvement in the signal of the crack using the new laser. From this surface "image," (see Fig. 3b) the presence of the three surface-breaking cracks are clearly visible. This is a significant improvement.

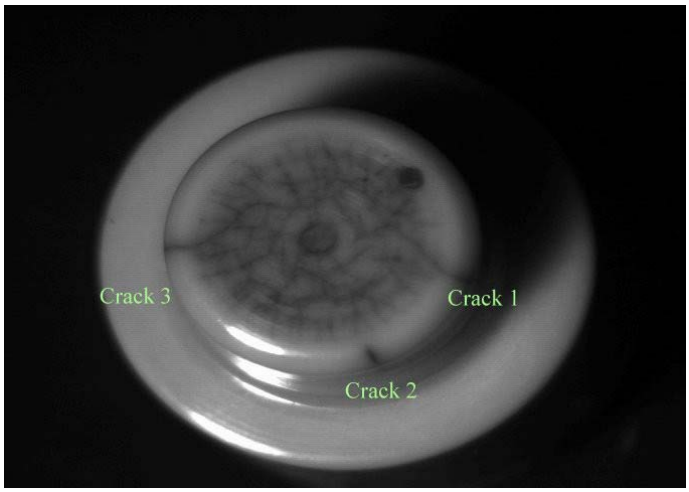

Fig. 2. Optical Photomicrographs of MgO High pressure fuel injector nozzle showing position of surface-breaking cracks.

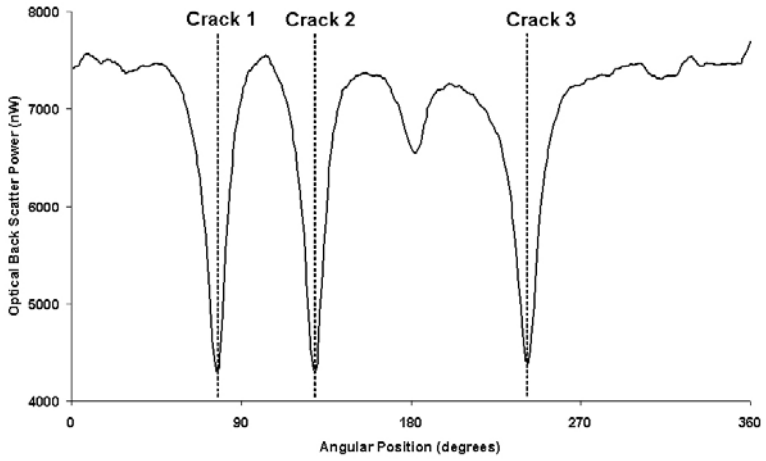

(a)

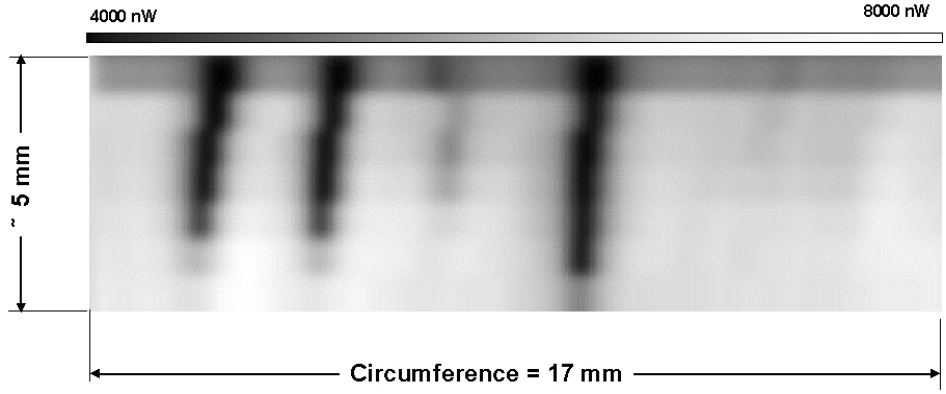

(b)

Fig. 3. Optical back-scatter scan of MgO high-pressure fuel injector nozzle. (a) Line scan 1.2 mm from plungers top, (b) area scan (after image processing) of region 1.2 mm to 4.0 mm below top of sample.

B. Angle Optimization

Investigations are being done to determine the optimal angle for the angle back-scatter technique. The objective is to differentiate between surface and subsurface flaws. For this purpose, we are studying Brewster's Law to find the optimal angle. Brewster's Law states that at a particular angle, the Brewster Angle, all light reflected off of the surface of the sample will be polarized at an angle perpendicular to the plane of incidence. The plane of incidence is defined by the orientation of the incident beam and the reflected beam. The direction of polarization of a light wave is defined by the direction of propagation of the electric field vector. When the electric field vector is perpendicular to the plane of incidence, the beam is said to be perpendicularly polarized. The Brewster Angle is defined by the optical properties of the material from the following relationship:

$$\tan \theta = n_2/n_1,$$

where n_2 is the index of refraction of the material being observed and n_1 is the index of refraction of the air.

When the laser is positioned at the Brewster Angle, some of the perpendicularly polarized component of the light reflects off the surface of the material. The parallel-polarized component of the incident light is transmitted below the surface. This light travels through the material until it dissipates, interacts with another surface, or is completely transmitted. Some of the refracted light that interacts with another surface such as a subsurface defect will then be reflected (see Fig. 4). The light that reflects off the internal surface will also be captured by the wide-angle camera lens. This reflected light is then focused in with the originally reflected light. Since the internally reflected light has a larger parallel-polarized component, the ratio of parallel light intensity to total intensity will increase. The beam then travels through a polarizing beam splitter cube. The beam splitter cube separates the parallel and perpendicularly polarized components of the scattered light and sends them in different directions. The light then travels to detectors, which sends a signal to an optical power meter which gives a readout.

Initial data have been acquired from glass slides with simulated defects on the back surface. The laser is set up at the Brewster Angle for glass, and the above procedure is followed. Data acquired from a glass slide with no simulated defects returned a beam that had a parallel component that was about 1% of the total beam. With the simulated defects on the back surface of the glass, about 5% of the light returned had parallel polarization.

NDE for Insulating Materials

We continue work on developing this aspect of this effort.

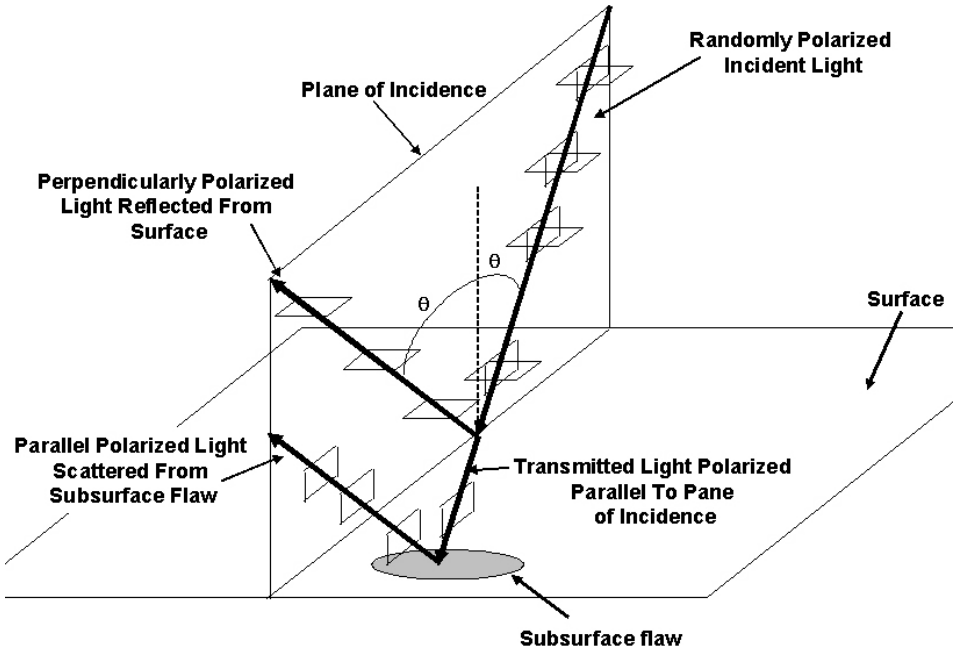

Fig. 4. Some light reflects off the surface of the material while some is refracted and reflects off a subsurface defect.

Meetings, Trips, Communications

Meetings

None

Trips

None

Communications

Additional discussions were held with staff of Cummins Engine in Columbus, IN.

NDE Development for Ceramic Valves for Diesel Engines

J. G. Sun, J. Zhang, W. A. Ellingson,
Argonne National Laboratory
and
M. J. Andrews
Caterpillar, Inc.

Objective/Scope

Emission reduction in diesel engines designated to burn fuels from several sources has lead to the need to assess ceramic valves to reduce corrosion and emission. The objective of this work is to evaluate several nondestructive evaluation (NDE) methods to detect defect/damage in structural ceramic valves for diesel engines. One primary NDE method to be addressed is elastic optical scattering. The end target is to demonstrate that NDE data can be correlated to material damage as well as used to predict material microstructural and mechanical properties. There are three tasks to be carried out: (1) Characterize subsurface defects and machining damage in flexure-bar specimens of NT551 and SN235 silicon nitrides to be used as valve materials. Laser-scattering studies will be conducted at various wavelengths using a He-Ne laser and a tunable-wavelength solid-state laser to optimize detection sensitivity. NDE studies will be coupled with examination of surface/subsurface microstructure and fracture surface to determine defect/damage depth and fracture origin. NDE data will also be correlated with mechanical properties. (2) Assess and evaluate subsurface damage in ceramic valves to be run in bench test and in a single-cylinder-engine test. All valves will be examined at ANL prior to test, during periodic scheduled shut downs, and at the end of the planned test runs. (3) Evaluate healing of subsurface damage by laser glazing on machined surfaces of GS44 ceramics. ANL will perform laser-scattering characterization on machining surfaces at before and after glazing treatment. NDE data will be correlated with glazing parameters and mechanical properties.

Technical Highlights

Work during this period (April-June 2002) focused on developing laser scatter system for full-valve scans.

1. Elastic Optical Scattering NDE for Machining Damage

During this period a limited effort was spent on calibration of laser scatter data. A NIST standard specimen with a C-crack is used for this study. Laser-scattering image data will be analyzed to determine detection sensitivity of the C-crack under various setup conditions and scan parameters. Results of this study will be presented in the next quarterly report.

2. Laser-Scattering System Development for Si_3N_4 Valves

During this period we continued development of the laser-scattering system suitable for scanning an entire valve. A lathe unit will be used to rotate and translate the valve for scanning. Figure 1 is a photograph of the lathe unit and Fig. 2 shows the modified schematic diagram of the laser-scattering system setup. All four stages (two translation and two rotation stages) used in the system have been individually tested. A data acquisition program has been developed to control the combined motions of all four stages to follow the shape of a valve and to synchronously obtain data during a scan. The profile of a typical ceramic valve was measured as plotted in

Fig. 3. The optical detection train is also been setup. Progress of this development will be reported in the next period.

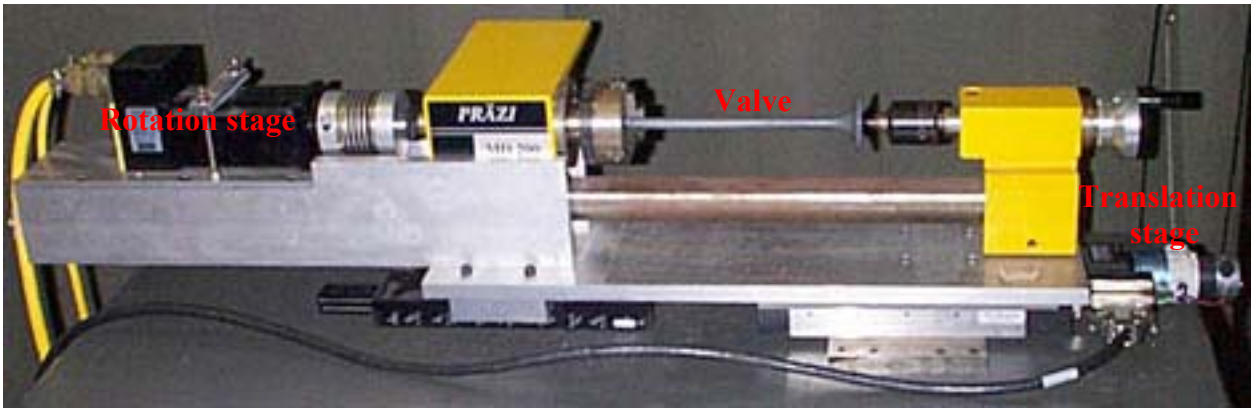

Fig. 1. Photograph of a lathe unit consisting of a translation and a rotation stage for laser-scattering scanning of the mounted valve.

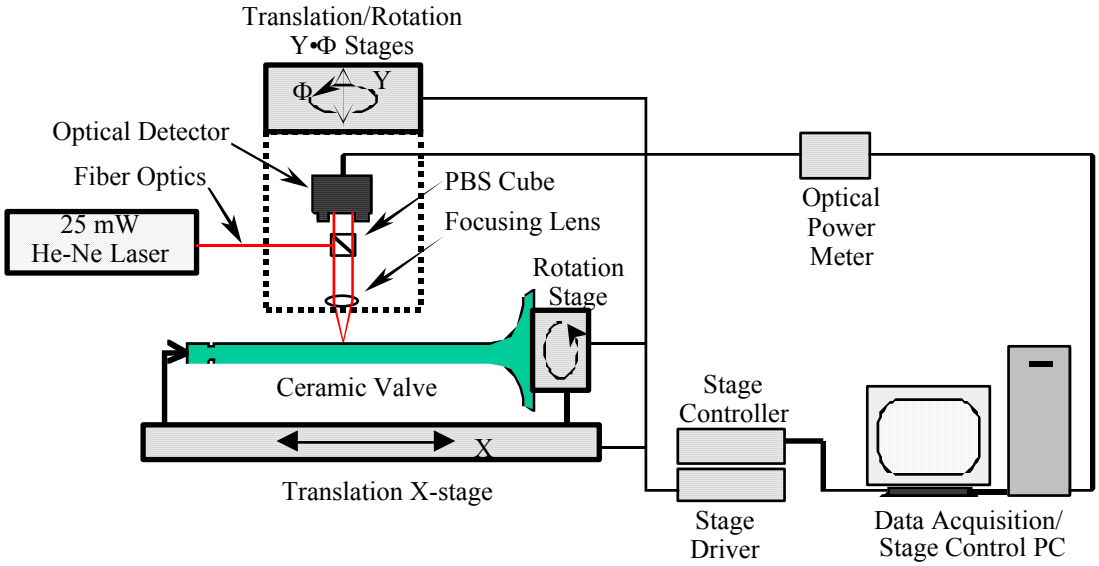

Fig. 2. Schematic diagram of laser-scattering system for valve scan.

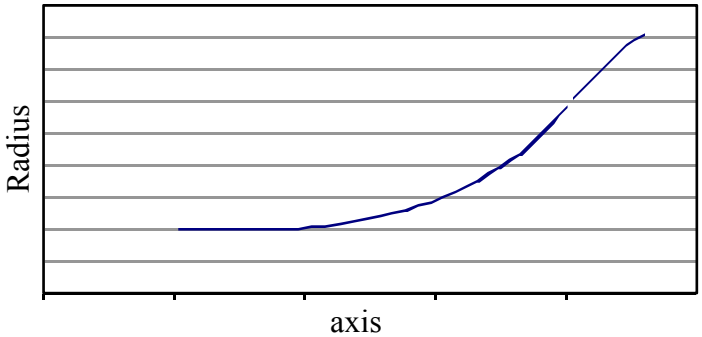

Fig. 3. Measured profile of a ceramic-valve head section.

Status of Milestones
Current ANL milestones are on or ahead of schedule.

Communications/Visits/Travel
J. G. Sun attended the American Ceramic Society's 104th Annual Meeting & Exposition in St. Louis, MO, April 28-May 1, 2002, and made a presentation entitled "Laser Scattering Detection of Subsurface Defects as Fracture Origins in Silicon-Nitride Ceramics."

J. G. Sun visited Dr. M. J. Andrews of Caterpillar Inc. on May 14, 2002, to discuss project issues.

Problems Encountered
None this period.

Publications
None this period.

Life Prediction of Diesel Engine Components

H. T. Lin, T. P. Kirkland, M. K. Ferber
Oak Ridge National Laboratory
and
M. J. Andrews
Caterpillar, Inc.

Objective/Scope

The valid prediction of mechanical reliability and service life is a prerequisite for the successful implementation of structural ceramics as internal combustion engine components. There are three primary goals of this research project which contribute toward that implementation: the generation of mechanical engineering data from ambient to high temperatures of candidate structural ceramics; the microstructural characterization of failure phenomena in these ceramics and components fabricated from them; and the application and verification of probabilistic life prediction methods using diesel engine components as test cases. For all three stages, results are provided to both the material suppliers and component end-users.

The systematic study of candidate structural ceramics (primarily silicon nitride) for internal combustion engine components is undertaken as a function of temperature (< 900°C), environment, time, and machining conditions. Properties such as strength and fatigue will be characterized via flexure and rotary bend testing.

The second goal of the program is to characterize the evolution and role of damage mechanisms, and changes in microstructure linked to the ceramic's mechanical performance, at representative engine component service conditions. These will be examined using several analytical techniques including optical and scanning electron microscopy. Specifically, several microstructural aspects of failure will be characterized:

(1) strength-limiting flaw-type identification;
(2) edge, surface, and volume effects on strength and fatigue size-scaling
(3) changes in failure mechanism as a function of temperature;
(4) the nature of slow crack growth; and
(5) what role residual stresses may have in these processes.

Lastly, numerical probabilistic models (i.e., life prediction codes) will be used in conjunction with the generated strength and fatigue data to predict the failure probability and reliability of complex-shaped components subjected to mechanical loading, such as a silicon nitride diesel engine valve. The predicted results will then be compared to actual component performance measured experimentally or from field service data. As a consequence of these efforts, the data generated in this program will not only provide a critically needed base for component utilization in internal combustion engines, but will also facilitate the maturation of candidate ceramic materials and a design algorithm for ceramic components subjected to mechanical loading in general.

Technical Highlights

Studies of dynamic fatigue properties of SN84 silicon nitride ceramic at 1200°C in air, which were transversely machined per ASTM C116 standard, were completed during this reporting period. The objective of this study is to provide an understanding on the effect of grinding orientation on the mechanical properties. Mechanical tests for transversely machined bend bars would be more representative of mechanical strength obtained for the silicon nitride valves, which would be transversely machined in the component production lines. The study would also provide a complete database for component design and lifetime prediction interest of diesel engine companies. Dynamic fatigue tests were conducted in four-point bending using 20mm/40mm, α-SiC semi-articulating fixtures at 1200°C in air. Stressing rate of 30 MPa/s was employed to evaluate the inert strength characteristic as a function of test temperature. Tests at stressing rate of 0.003 MPa/s was not carried out due to the limited availability of test bend bars. Load was continuously measured and controlled as a function of time via a PC, and flexure strength was calculated using ASTM C1161. Mechanical results at 1200°C showed that the strength of SN84 bend bars was not sensitive to machine orientation, similar to those obtained at 850 and 1000°C, as shown in Fig.1 and Table 1. The insensitivity of mechanical properties to machining orientation at elevated temperatures could be attributed to the healing of surface machining flaws by oxidation. On the other hand, the inert strength of SN84 remained relative constant, especially for transversely machined bend bars, at temperature between 20 and 1200°C, as shown in Fig. 2. However, the strengths obtained at temperature ≥1000°C and 0.003 MPa/s were ~10% higher than those obtained at 30 MPa/s, suggestive of the onset of SCG processes possibly due to the softening of secondary glassy phase.

Sixteen Norton NT551 silicon nitride exhaust valves evaluated previously were provided to Caterpillar for bench rig test, as shown in Fig. 3. The objective of bench rig test is to verify the probabilistic design of valve via the use of ANSYS Finite Element analysis. Also, the use of bench test rig could save $140K operational cost as compared with the engine test at the initial design stage. Engine test with candidate silicon nitride valves will be followed after the success of bench rig test and probabilistic design validation.

Both tensile and rotary bending fatigue specimens of TiAl intermetallic alloy in as-received and after oil immersion test have been received from Caterpillar. Test matrices for both tests at temperature up to 800°C in air have been established to develop database necessary for probabilistic design and life prediction for TiAl valve components.

Status of Milestones

All milestones are on schedule.

Communications / Visitors / Travel

A complete set of dynamic fatigue results of transversely machined SN84 bend bars were communicated with M. J. Andrews at Caterpillar.

Update of the status of initial bench test on Norton NT551 silicon nitride exhaust valves was held with M. J. Andrews at Caterpillar.

Communication with Juses Chapa-Cabrera at Caterpillar to discuss the testing matrix for the TiAl alloy.

Problems Encountered

None.

Publications

H. T. Lin and T. P. Kirkland, A. A. Wereszczak, and M. J. Andrews, "Effect of Long-Term Oil Immersion Test on Mechanical Reliability of Candidate Silicon Nitride Ceramics for Diesel Engine Applications," presented in the 2002 American Ceramic Society Annual Meeting, April 28-May 1, 2002.

References

[1] H. T. Lin, T. P. Kirkland, M. K. Ferber, and M. J. Andrews, "Life Prediction of Diesel Engine Components," Heavy Vehicle Propulsion System Materials Program Bimonthly Technical Progress Report to DOE Office of Transportation Technologies, Sept.-Dec. 2001.
[2] H. T. Lin, T. P. Kirkland, M. K. Ferber, and M. J. Andrews, "Life Prediction of Diesel Engine Components," Heavy Vehicle Propulsion System Materials Program Bimonthly Technical Progress Report to DOE Office of Transportation Technologies, Jan. – March 2002.

Table 1. Summary of uncensored Weibull strength distributions for NGK SN84 specimens, longitudinally and transversely machined per ASTM C1161.

				± 95%

Material	# of Spmns. Tested	Stressing Rate (MPa/s)	Temp. (°C)	± 95% Uncens. Weibull Modulus	Uncens. Uncens. Weibull Modulus	Uncens. Chrctstic Strength (MPa)	Chrctstic Strength (MPa)
SN84 (Long.)	20	30	20	10.59	7.06, 15.00	858	818, 898
SN84 (Long.)	20	0.003	20	9.61	6.52, 13.80	754	716, 792
SN84 (Tran.)	15	30	20	12.52	7.59, 18.24	758	723, 793
SN84 (Tran.)	15	0.003	20	10.10	6.67, 14.02	659	662, 697
SN84 (Long.)	15	30	850	25.14	15.58, 37.35	818	718, 803
SN84 (Long.)	15	0.003	850	10.27	6.51 15.06	761	718, 803
SN84 (Tran.)	15	30	850	20.38	13.12, 29.25	810	787, 832
SN84 (Tran.)	15	0.003	850	18.13	11.75, 25.85	781	756, 805
SN84 (Long.)	15	30	1000	20.59	13.49, 29.45	777	757, 796
SN84 (Long.)	15	0.003	1000	14.71	9.63, 20.85	863	829, 896
SN84 (Tran.)	15	30	1000	15.80	9.63, 23.69	780	752, 809
SN84 (Tran.)	15	0.003	1000	11.72	7.58, 16.81	816	776, 855
SN84 (Long.)	15	30	1200	13.36	8.34, 19.83	777	757, 796
SN84 (Long.)	15	0.003	1200	9.82	5.87, 15.04	863	829, 896
SN84 (Tran.)	15	30	1200	14.61	9.43, 20.94	775	744, 805

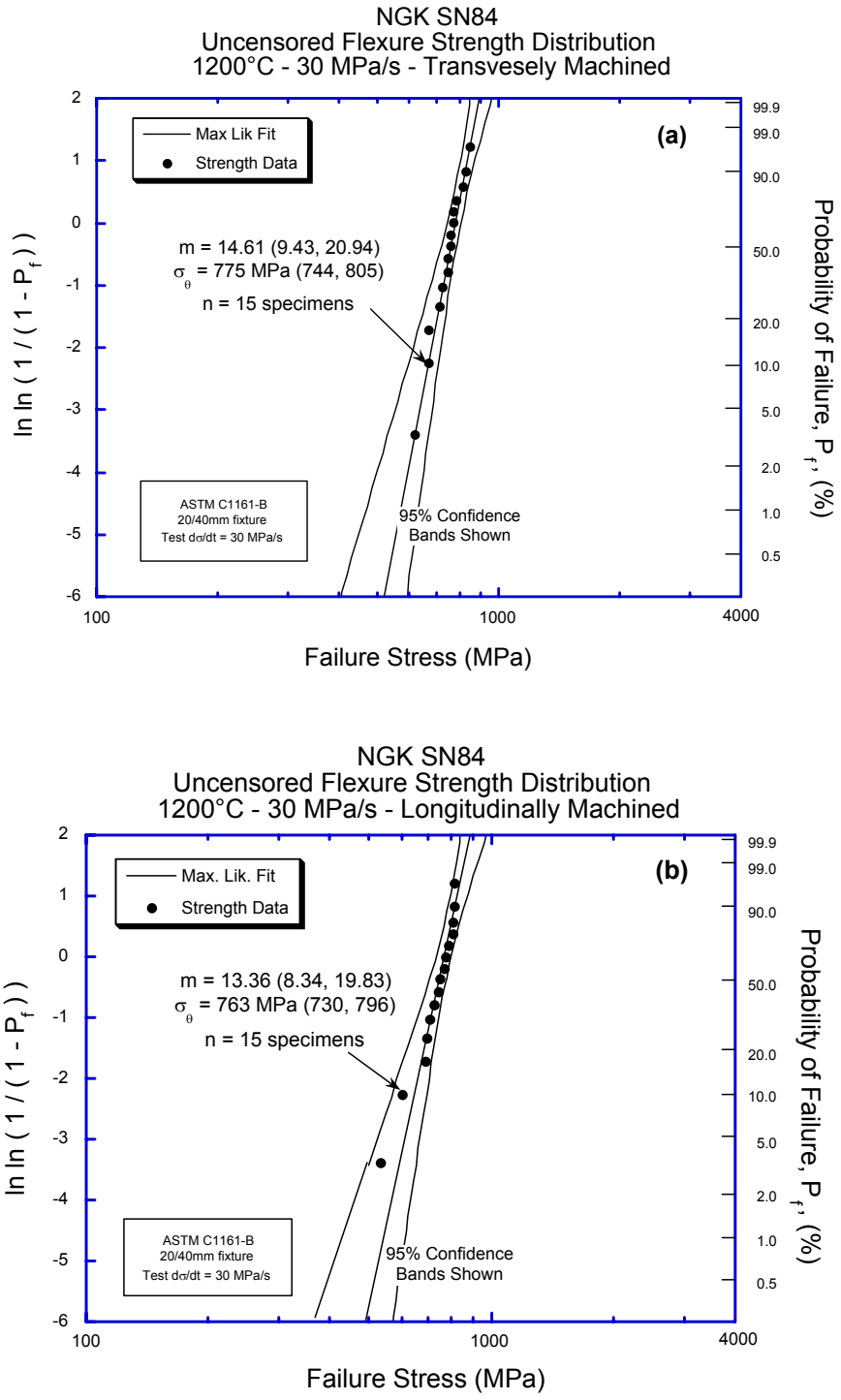

Figure 1. Characteristic strength of NGK SN84 silicon nitride machined transversely and tested at 1200°C and 30 MPa/s. Note that the dimension of bend bar has been scaled down to unit size in the analysis. Results of longitudinally machined SN84 MOR bars are included for comparison (Fig. 1b).

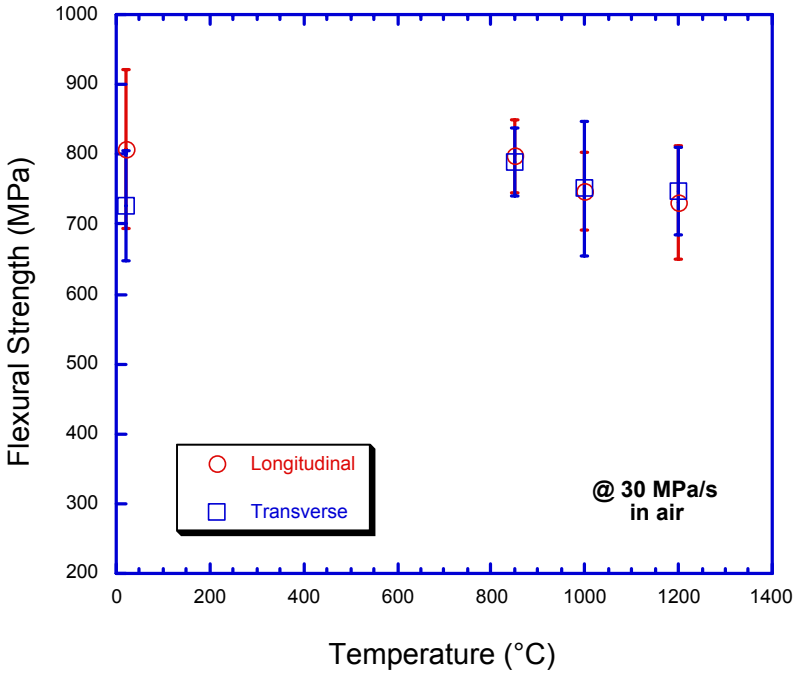

Figure 2. Flexural strength versus test temperature results of SN84 silicon nitride machined transversely and longitudinally.

Figure 3. Norton NT551 silicon nitride valve provided to Caterpillar to bench rig test and verify the probabilistic design.

Durability of Diesel Engine Component Materials

Peter J. Blau and Ronald D. Ott
Oak Ridge National Laboratory
and
Jun Qu
ORISE Post-Doctoral Fellow

Objective/Scope

The objective of this effort is to enable the development of more durable, low-friction moving parts in diesel engines for heavy vehicle propulsion systems by conducting friction, lubrication, and wear analyses of advanced materials, surface treatments, and coatings. The scope of materials and coatings is broad and includes any metallic alloy, intermetallic compound, ceramic, or composite material which is likely to be best-suited for the given application. Parts of current interest include scuffing-critical components, like fuel injector plungers and EGR waste gate components. Hot scuffing is a primary surface damage mode of interest. Bench-scale simulations of the rubbing conditions in diesel engine environments are used to study the accumulation of surface damage, and to correlate this behavior with the properties and compositions of the surface species. The effects of mechanical, thermal, and chemical factors on scuffing and reciprocating sliding wear are being determined. Results will be used to refine material selection strategies and suggest materials for durability-critical engine components.

Technical Highlights

High-Temperature Scuffing Tests. Results of high temperature (600^{o} C) scuffing tests of ten leading candidate material couples, reported previously, indicated that the best composite scores were obtained for a self-mated, commercial alloy steel (GallTough™) and for a ceramic/ intermetallic alloy couple (transformation toughened zirconia against Ni_3Al alloy). This test involves a cylindrical pin, pivoting on its cylindrical surface against a flat tile so as to form a wear mark shaped like a bow tie.

Further studies were conducted on the GallTough alloy to investigate the microstructural changes that occurred as a function of contact exposure (number of cycles). Tests were conducted for seven minutes, 20 minutes, and 60 minutes. As before, the normal force was 10 N, and the oscillating rate was 1 Hz. At a cycle rate of 1 Hz, 7 minutes = 420 cycles, 20 minutes = 1200 cycles, and 60 minutes = 3600 cycles of oscillation. The intervals of testing corresponded to the mid-point of an initial drop in frictional torque (7 minutes), the point where the torque seemed to level off (20 minutes), and the endpoint of the standard test interval used for all the material pairs (60 minutes), respectively.

Tile specimens were examined in both optical and scanning electron microscopes, both on their contact surfaces and in polished cross-sections designed to reveal sub-surface microstructural details. Scanning electron images of the GallTough tile specimen are shown in Figure 1. The 420-cycle surface showed evidence of plastic deformation but relatively little wear debris. The 1200 cycle and 3600 cycle contact surfaces showed considerably more debris. The increase in debris corresponded with a drop in frictional torque on the specimens, suggesting that once a debris layer formed, the frictional torque level was reduced. Most of this decrease occurred

between 420 and 1200 cycles of contact oscillation. Beyond about 1200 cycles, the torque level remained relatively steady.

	Surface Features	Subsurface Features
420 cycles (plastic deformation, few loose wear particles)	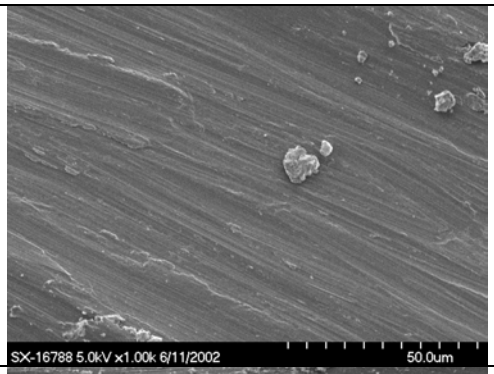	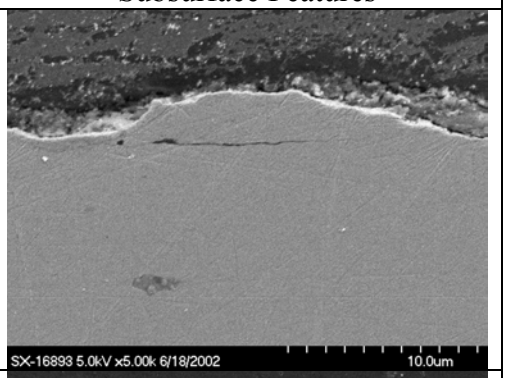
1200 cycles (loose particles and growth of compacts of agglomerated particles)	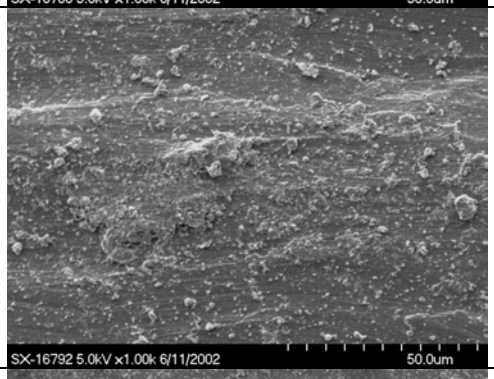	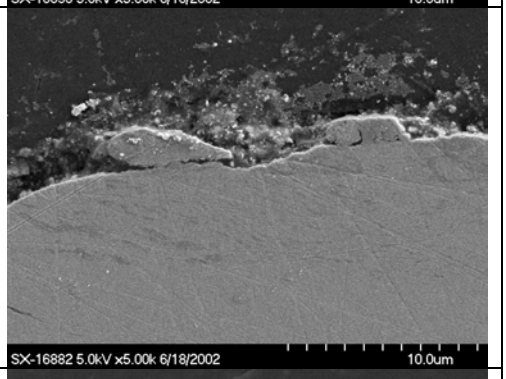
3600 cycles (established layers of particle compacts, some loose particles)	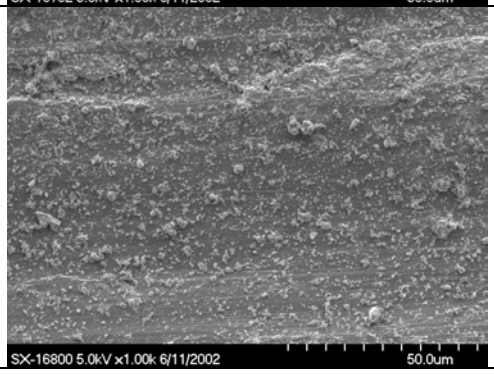	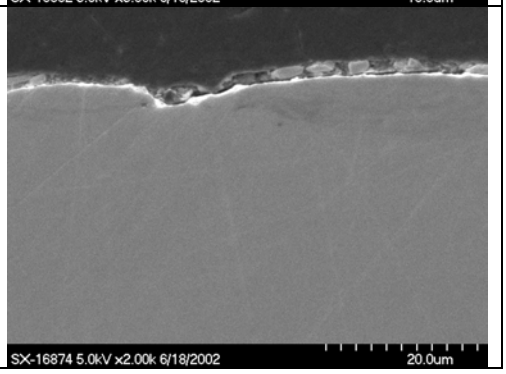

Figure 1. Surface and subsurface features of GallTough™ tile specimens subjected to different durations of oscillating contact. A scaling bar is indicated at the lower right of each image. (SEM)

The 420-cycle tile displayed indications of sub-surface micro-cracking, but similar features were not seen in the 1200 and 3600 cycle specimens. It is possible that the continued compression of the surface and the generation of compliant, lower shear-stress debris layers reduced the cracking tendency. Careful examination indicates mechanical mixing of the oxidized and un-oxidized, but plastically deformed alloy in localized regions of the surface for all three test lengths. These specimens will be further examined using the ORNL scanning acoustic microscope to seek additional evidence of the stages of damage evolution in high-temperature scuffing.

Scuffing tests were also performed using upper pins treated with a proprietary "C3" surface treatment (C3 International, Roswell, GA). This process for metal wear and friction reduction was originally developed in the former Soviet Union and is in the process of commercialization in the US. Results of those tests fell within the range of the other material couples and will not be discussed further here.

Fuel Injector Plunger Scuffing. The contact conditions of the ORNL 'single cylinder-on-twin cylinders' tests run earlier on a series of plunger materials and candidate plunger materials produced a more severe form of wear than would be observed on actual fuel injection system components. Therefore, a revision of the contact geometry to reduce the contact stress has been made. During the next period, a series of wear tests in at least one type of diesel fuel will be run to generate baseline data for zirconia on 52100 steel and tool steel on 52100 steel, selected to represent typical plunger material couples.

Future Plans

1. Continue metallurgical studies of scuff-tested specimens, including use of the scanning acoustic microscope.

2. Conduct tests on fuel injector plunger materials under diesel fuel-lubricated conditions using a new contact configuration that is designed to better simulate the stresses and type of damage seen in actual plunger components.

Travel

None.

Status of FY 2002 Milestones

1) Complete design and construction of fixtures to adapt existing ORNL friction and wear testing machine for fuel injector plunger materials. (December 15, 2001 – completed.)

2) Complete elevated temperature scuffing tests of leading candidate materials and coatings. Submit report. (March 31, 2002 – uncoated material evaluations are completed, but these will be supplemented with additional work on novel coatings in the next quarter.)

3) Complete tests of candidate ceramic materials and cermets for fuel injector applications. Submit report. (September 30, 2002)

Publications

None this period.

Laser Surface Texturing Of Lubricated Ceramic Parts

Peter J. Blau
Oak Ridge National Laboratory

Objective/Scope

The objective of this effort is to evaluate the frictional benefits of laser dimple patterns on the lubrication of ceramic surfaces. This project is part of a joint Argonne National Laboratory/ ORNL analysis of the benefits of a laser surface texturing (LST) process developed by Prof. Itzhak Etsion, Surface Technologies, Ltd., Israel. That process uses a computer-controlled laser to produce a pattern of shallow, rounded dimples on bearing surfaces. Based on calculations, preliminary tests, and limited field trials, the developer claims that LST enhances the ability of a lubricated surface to establish a load-bearing hydrodynamic film that decreases friction relative to a non-dimpled surface. The ORNL portion of this joint effort is focused on two aspects of LST: (1) conducting reciprocating tests of ceramic surfaces using lubricating fluids with various viscosities, and (2) determining the microstructural changes that are associated with the LST process.

Technical Highlights

The selection of ceramic materials and the tribotesting conditions were both described in the previous quarterly report. In summary:

Materials:
LST specimens: zirconia (TTZ), silicon carbide (Hexaloy-SA™);
Flat specimens: silicon nitride (GS-44)
Geometry: oscillating flat-sided cylinder on flat tile
Normal forces: 25, 50, 75, and 100 N.
Oscillating frequencies 2, 5, 10 Hz
Stroke length: 10 mm
Lubricants: water, mineral oil, Valvoline brand "Cummins Blue" diesel motor oil.

Scanning electron microscopy characterization of LST damage in TTZ. Specimens of TTZ were laser surface-treated (LST) by Surface Tech, in Israel, and then optically photographed and measured using stylus-type and laser-type surface measuring systems. Image analysis was performed to determine the percent of the surface that was covered by the laser dimples. Scanning electron micrographs were obtained as an initial study of laser-induced microstructural changes. Figure 1 shows the 'splash zone' near the edge of a laser dimple and Figure 2 shows its detailed quenched structure consisting of 100 nm-sized grains. Note that the cooling-induced microfractures tend to be intergranular. Additional work is planned to study the fine structure and phase content of the thermally-affected zone using the ORNL, High Temperature Materials Laboratory focused-ion-beam thinning facility to select regions of interest, and transmission electron microscopy to examine the resultant thin sections.

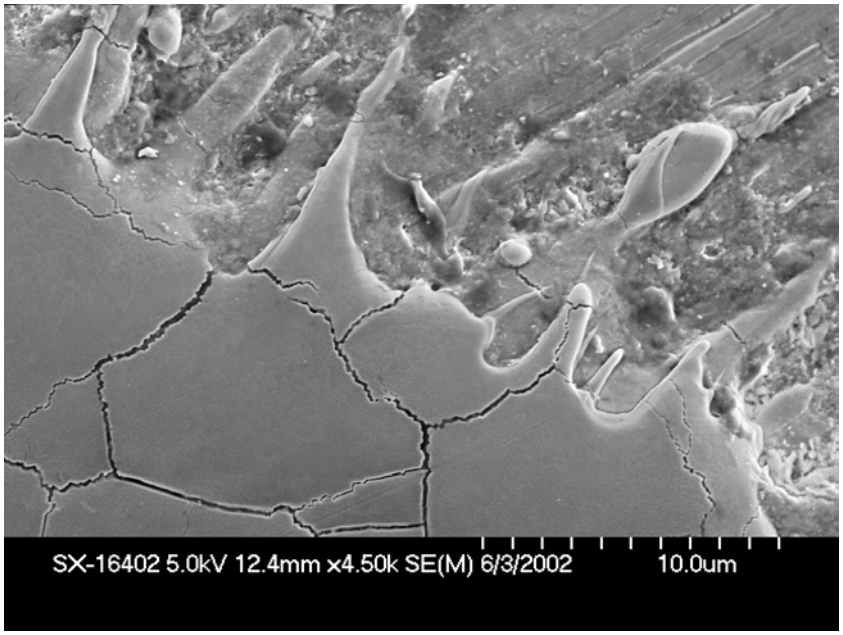

Figure 1. Edge of a dimple in a LST surface of TTZ (as-received). The original ground surface can be seen at the upper right, and the smooth, but micro-fractured region of the dimple is evident. The size marker is at the lower right. Each small tic is 1 μm.

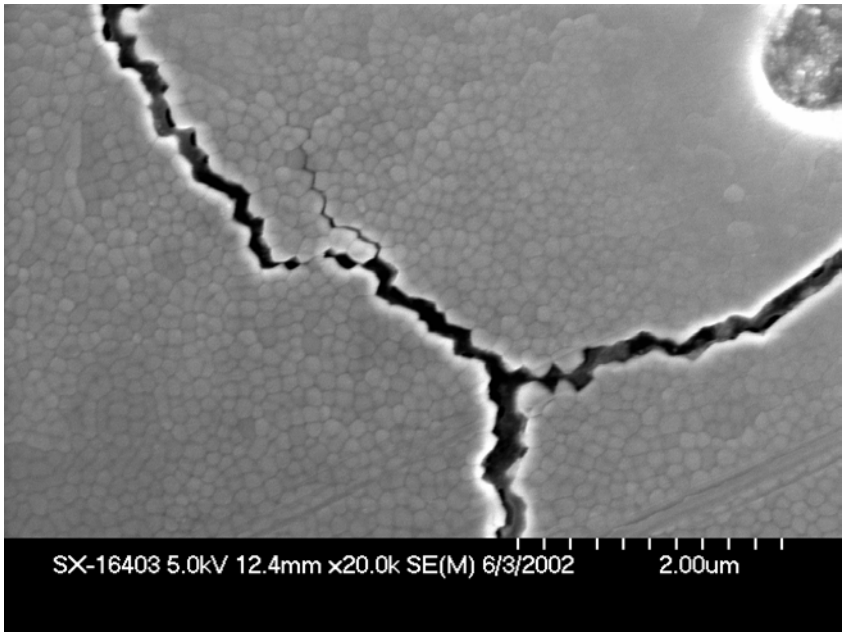

Figure 2. Detail of the 'splash' zone above showing nano-scale grains.

Work continues on tribotesting the LST SiC specimens that were recently prepared by Prof. Etsion at Surface Tech. Baseline tests on un-LST surfaces will be compared with tests on LST surfaces. A significant challenge is in the alignment of the test surfaces. Special, new fixtures have been fabricated to address this issue.

Future Plans

(1) Continue friction tests on LST and non-LST SiC materials.

(2) Use transmission electron microscopy to characterize LST damage to both TTZ and SiC.

Travel

P. Blau visited Argonne National Laboratory on June 10-12, 2002, both to review ORNL progress on this effort for Sid Diamond, DOE/OTT, and to coordinate research plans with G. Fenske and O. Ajayi.

Status of FY 2002 Milestones

1) Complete design and construction of fixtures to adapt existing ORNL friction- and wear-testing machine for cylinder on flat testing. (January 31, 2001 – completed.)

2) Complete baseline friction tests of as-ground ceramics in three liquid lubricants. (May 31, 2002)

3) Complete friction tests of laser surface textured ceramics in three lubricants. Submit report. (July 31, 2002 – delayed in order to include results on SiC)

4) Characterize laser-dimpling effects on the microstructures of selected ceramics. Submit report. (September 30, 2002)

Publications

None.

Implementing Agreement For A Programme Of Research And Development On Advanced Materials For Transportation Applications

M. K. Ferber
Oak Ridge National Laboratory

Objective/Scope

The International Energy Agency (IEA) was formed via an international treaty of oil consuming countries in response to the energy crisis of the 1970s. A major objective of the IEA is to promote secure energy supplies on reasonable and equitable terms. The governing board of the IEA, which is composed of energy officials from each member country, regularly reviews the world energy situation. To facilitate this activity, each member country provides energy experts who serve temporary staff assignments at IEA headquarters. These staff or secretariat support the governing board by collecting and analyzing energy data, making projections in energy usage, and undertaking studies on specialized energy topics. The governing board is also assisted by several standing groups; one being the committee on energy research and technology (CERT), which encourages international cooperation on energy technology. Implementing agreements (IAs) are the legal instruments used to define the general scope of the collaborative projects. There are currently 40 active implementing agreements covering research topics such as advanced fuel cells, coal combustion science, district heating and cooling, enhanced oil recovery, fluidised bed conversion, fusion materials, solar heating and cooling, pulp and paper, hydropower, heat pumping technologies, hybrid and electric vehicles, high temperature super conductivity, wind turbines, and high temperature materials. A complete listing can be found at the IEA website, www.iea.org.

This progress report summarizes recent activities in the implementing agreement entitled, "Implementing Agreement For A Programme Of Research And Development On Advanced Materials For Transportation Applications." This implementing agreement currently consists of one active annex entitled," Annex II: Co-Operative Program on Ceramics for Advanced Engines and Other Conservation Applications". The motivation for this IA is the development of new and improved ceramic materials, brittle material design methods, and life prediction methodology. The objective of Annex II is coordinated R&D on advanced ceramics leading to standardized methods for testing and characterization.

The Executive Committee for the IA on Advanced Materials is also exploring the possibility of adding new efforts (Annex III and Annex IV). Annex III focuses on the characterization of contact damage (fatigue) while Annex IV deals with materials for hydrogen storage.

Technical Highlights

Preparations for the annual Executive Committee meeting were initiated this reporting period. This meeting will be held in conjunction with the CIMTEC 2002 Meeting on Tuesday, July 16 from 3:00 to 6:00 p.m. in Florence, Italy.

Annex II

Annex II currently consists of two active efforts, Subtasks 11 and 12. In Subtask 11, techniques for the measurement of thermal and mechanical fatigue of silicon nitride ceramics are being examined. National efforts in Japan and the United States focus on the development of procedures for evaluating the mechanical fatigue behavior of silicon nitride ceramics using either uniaxial flexure or biaxial test specimens. The national effort in Germany consists of the development of thermal fatigue procedures using the laser thermal shock equipment evaluated in Subtask 9. The national effort in Sweden will focus on the evaluation of the fracture surfaces of specimens tested in Japan, the United States, and Germany.

United States research activities in support of Annex II have involved the measurement of the cyclic fatigue of a commercial silicon nitride (GS44 manufactured by Honeywell Ceramics Components). The rotary bend fatigue (RBF) machine being used for this effort is shown in Figure 1 while Figure 2 illustrates the loading configuration. Note that in the present equipment, the dead weight loading that is normally used to generate stresses in the specimens was replaced by a computer controlled pneumatic loading system. This system could either maintain a static load or control the load as a function of time.

Preliminary testing involved measuring the 850°C strength of RBF specimens as a function of loading rate at a fixed rotational speed. During slow loading rate tests, deformation of the left-hand grip caused excessive deformation at the free end of the cantilever which prevented completion of the test. This problem was attributed in part to the high stresses generated in the left-hand grip due to the high applied in this region (see by the moment diagram in Figure 2). To correct this problem, an opposing loading configuration is being explored (Figure 3).

Status of Milestones

All milestones are on track.

Communications/Visits/Travel

Contacts were made with the executive committee members to discuss the next executive committee meeting.

Publications

None.

References

None

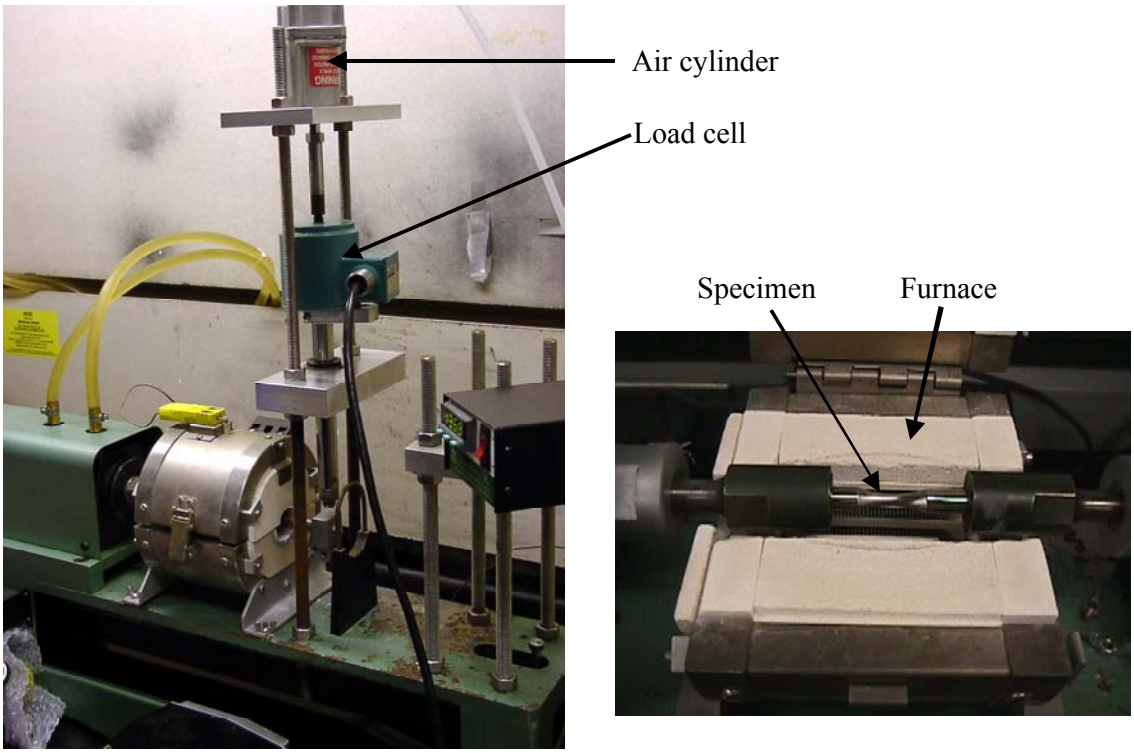

Figure 1: Rotary fatigue machine modified with computer-controlled pneumatic loading system.

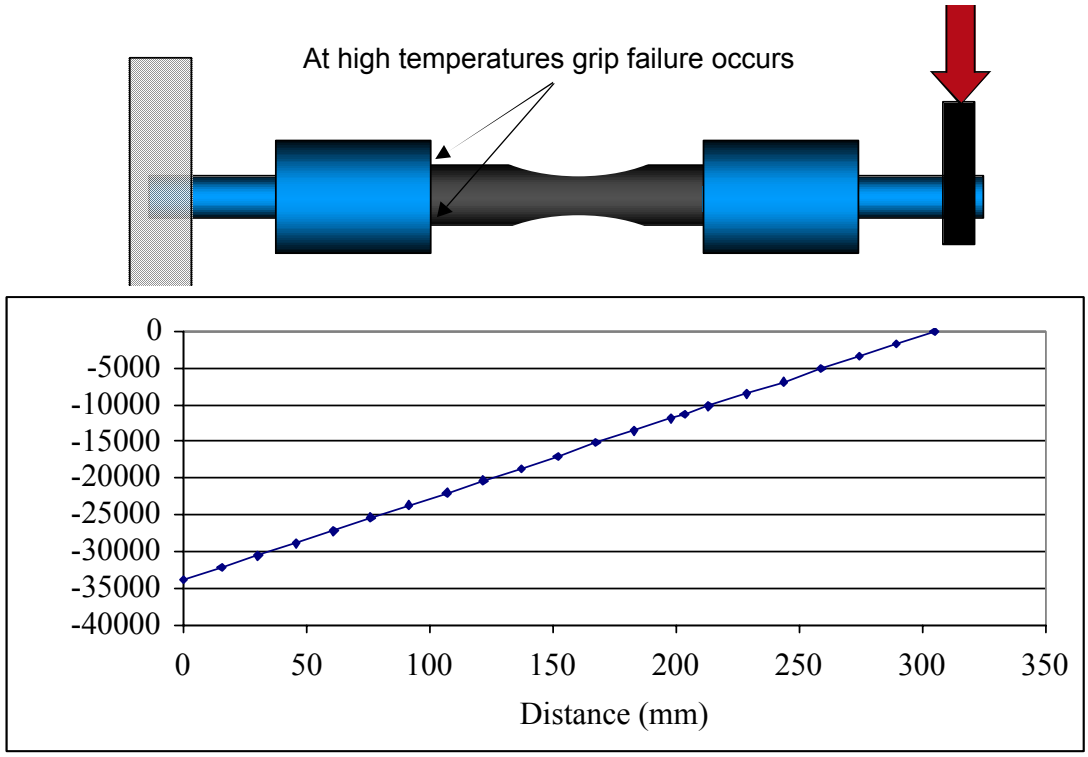

Figure 2: Schematic representation of the load geometry and corresponding moment diagram.

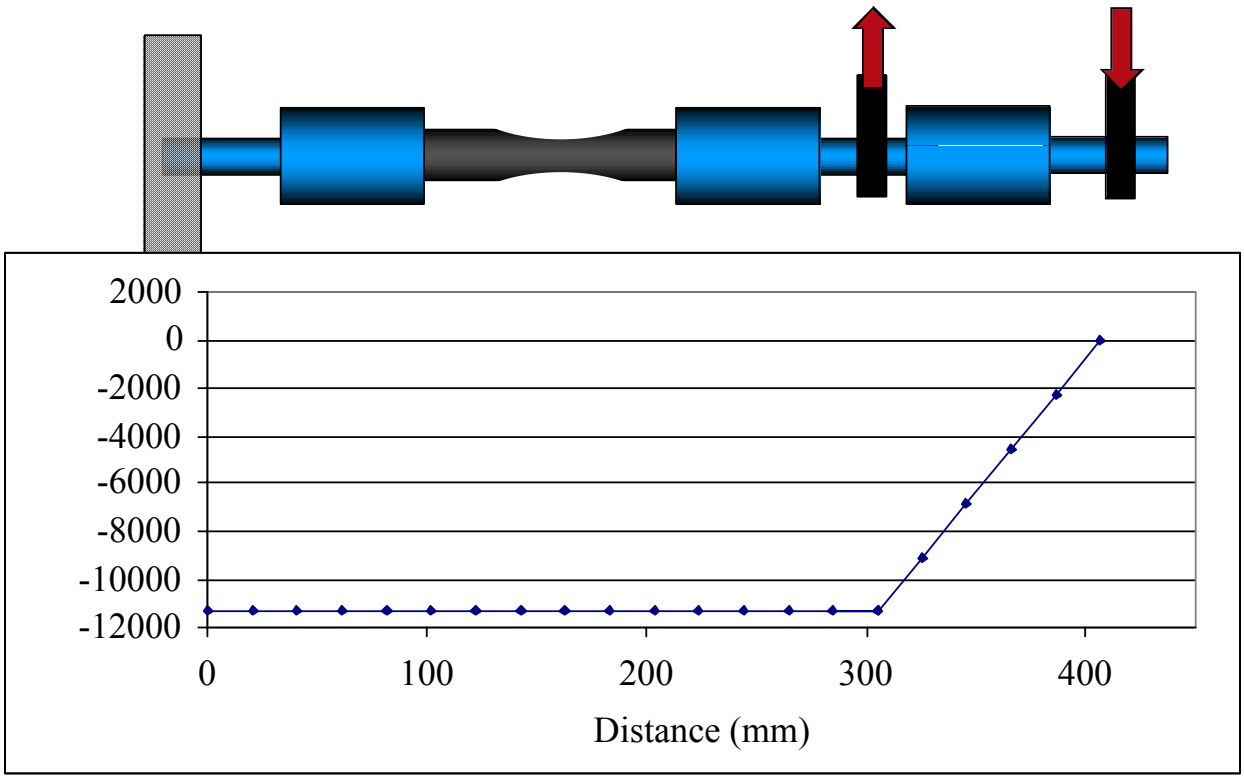

Figure 3: Schematic representation of the modified load geometry used to generate a constant moment.

Standards For Reliability Testing Of Heavy Vehicle Propulsion Materials

Said Jahanmir and William Luecke
National Institute of Standards and Technology

Objective/Scope

The objective of this project is to develop international standard test methods for assessing the reliability of ceramic components used in diesel engines and other heavy vehicle propulsion systems. Advanced ceramics such as silicon nitride offer a unique combination of properties that include lightweight, excellent high-temperature strength, and resistance to wear and corrosion. These properties make them particularly attractive for diesel engines, where their use as key engine components will allow the higher operating temperatures that lead to higher thermal efficiencies and environmentally cleaner propulsion systems. Reliability and cost-effectiveness are critical issues in implementing ceramics in the valve train of diesel engines. Ceramic valve train components are subjected to demanding conditions that include high contact loading, elevated temperatures, and corrosive environments. To ensure a reliable service life, standard test methods are needed to evaluate the performance of potential ceramics in highly loaded rolling and sliding contacts. This project will develop test methods for evaluating the contact damage behavior of ceramics under rolling and sliding conditions that simulate the cam roller followers, valves and valve seats. In support of this goal we will pursue four research thrusts: 1) fundamental issues in the relation between ceramic microstructure and performance reliability, 2) basic mechanisms that lead to formation and propagation of contact damage and the effect on reliability of residual stresses developed during machining and by contact, 3) effect of machining damage on contact reliability as well as the interactions between machining and contact damage that may lead to premature failure, 4) development of international standards for assessing contact damage.

Technical Highlights

Pre-Standards Research for Rolling Contact Fatigue

Although early grades of silicon nitride exhibited rolling contact fatigue (RCF) failures by spalling, similar to bearing steels in various laboratory tests,[1,2] modern grades typically do not fail by RCF[3,4,5] in laboratory testing. Effectively, the newer materials have outstripped the ability of the test method. Although several test geometries exist for evaluating RCF in the laboratory (thrust washer, ball-on-3-balls, twin-disc-on-rod), the 3-ball-on-rod (Federal Mogul test) is the most common in the United States. We are researching extensions to this test method that will enable it to again yield RCF data on modern grades of silicon nitride. We are also examining the its potential for ASTM standardization. The 3-ball-on-rod test[1], see Figure 1, uses a 9.52 mm diameter rod approximately 75 mm long, held in a precision chuck and driven at 3600 rpm. A special test head clamps 3 (or 5) specially prepared AISI 52100 steel balls against the rod at a known, fixed load. An accelerometer mounted on the test head detects the vibration produced as the balls drop into a developing spall on the rod, and shuts the test down when that vibration reaches a prescribed level.

During this reporting period research extended the wear rate tests from the previous period using Ceradyne Ceralloy 147-31N test rods to lower contact stresses. Table 1 summarizes the rolling contact fatigue/wear data to date. We have tested rods prepared by a proprietary, commercial finishing procedure (CF) and rods finished by rough grinding using a 220 grit wheel and further hand polished (HP). Visually, the HP rods have a finer finish than the CF rods, but the surface roughness, measured by profilometry is nominally the same ($R_a \approx 0.08$ μm). Figure 2 compares the two finishing procedures via SEM images and roughness profiles along axial and circumferential traces.

Are reported previously the commercially finished rods (CF) tested using Si_3N_4 balls at 7.27 GPa contact stress fail primarily by spalling along 1/2 to 1/3 of the circumference. These spalls are typically 20-30 μm deep. In contrast, two tests conducted at 6.3 GPa using Si_3N_4 test balls resulted in deep uniform wear, which resembled that of the hand-polished (HP) rods.

At all contact stresses the hand-polished (HP) wear excessively and uniformly around the circumference instead of spalling. These wear tracks are up to 90 μm deep. Generally the Si_3N_4 balls are also damaged along the contact circle. This damage is a shallow (1-2μm) flake 0.2-1 mm wide anywhere from 0.2 mm to the full circumference of the ball. Figure 3 shows the results of special interrupted tests to characterize the wear rate at contact stresses $4.0 < \sigma < 7.3$ GPa. In Figure 3, the wear coefficient, K, is defined as

$$K = \frac{VH}{PL} \tag{1}$$

where V is the volume of material removed by wear during sliding a distance, L, under a load, P; H is the hardness. Two things are apparent in Figure 3. The wear coefficient for the 7.27 GPa contact stress tests, using Si_3N_4 test balls, is larger than for the other contact stresses. Optical and SEM examination of the wear tracks and test balls did not indicate any obvious change in the wear mechanism that would account for this change, however. The wear tracks were visually similar. Secondly, the wear coefficient using the special 52100 steel test balls at 6.3 GPa is significantly smaller than that for 6.3 GPa using the Si_3N_4 test balls. In the previous reporting period we established that wear or deformation of the 52100 steel test ball is not the source of this difference.

Most of the work in this reporting period extended the research on contact damage in Si_3N_4 during single cycle indentation using spherical WC indenters. Twelve different silicon nitrides (Table 2) were characterized for hardness, toughness and indentation response. The different silicon nitrides fall into three basic types: bearing-grade materials, HIP'ed, creep resistant materials, and higher-toughness, gas-pressure-sintered (GPS) materials.

Knoop hardness $H_{K1}$was measured from five or six indents using a P = 9.8 N (1 kg) load following ASTM C1326 and calculated from

$$H_{K1} = 0.014229\left(\frac{P}{d^2}\right), \tag{2}$$

where d is the long diameter (in mm) of the indent measured optically. Fracture toughness, K_{1c}, was measured using the indentation crack length method of Anstis, et al.[6] using both 98 N and 49 N loads:

$$K_{1c} = 0.016\left(\frac{E}{H}\right)^{1/2}\left(\frac{P}{c^{3/2}}\right), \quad (3)$$

where E = Young's modulus, H = hardness, P = load and $2c$ = the tip-to-tip length of the resulting indentation crack. Of course, this method yields only approximate values of the toughness, subject to the accuracy of the calibration coefficient (0.016). However, there should be relatively little variability in the calibration for twelve such similar materials. Of course, the toughnesses may differ significantly from those measured by other methods, so no special weight should be assigned their absolute magnitudes. The indentation diagonal length, d (in mm) can be used to calculate the Vickers hardness, H_V, from the load, P, in N:

$$H_V = 0.0018544\frac{P}{d^2} \quad (4)$$

Testing employed the general procedure of ASTM C1327, but the loads were much higher: 49 N and 98 N. The calculation of the fracture toughness (Eq. 3) used this hardness. Although complete characterization of Young's modulus by instrumented, low-load spherical indentation is planned, that task is not complete, and for purposes of comparison, we have assumed E=310 GPa for all twelve silicon nitrides. The manufacturers reported values lie with 15 GPa of this value. The uncertainties reported in Table 2 represent only the statistical variability of the length measurements, and do not include any systematic errors.

The response to contact damage from spherical indenters was characterized for both the appearance of a residual impression as well as the formation of ring cracks around the indent site. Testing employed WC indenters of two diameters: 6.35 mm and 3.175 mm. After indentation at 25 N/s the shape and depth of the residual impression, d_{max}, was characterized by profilometry (Mahr Perthen Perthometer PRK). Residual impressions were typically up to 1 μm deep and 0.75 mm in diameter with a roughly spherical profile. Most often, there was little detectable uplift (h<0.05 μm) surrounding the indent. The one notable exception was the NBD-100, where the residual impressions inside the ring cracks were flat-bottomed and material outside the ring crack was raised up over the surface by up to 0.3 μm. The surface roughness of some of the specimens, as well as their slight (~1 μm over 6 mm) curvature, limited the accuracy of the residual impression depth to +/-0.03 μm. Often it was possible to find residual impressions by profilometry that were not detected using differential interference contrast (DIC or Nomarski) in the optical microscope. The existence of ring cracks surrounding the indent site was verified using optical microscopy, typically using DIC.

Figures 3 and 4 show that the different grades of silicon nitride have significantly different residual impression depths, d_{max} . Generally, the lines extrapolate back to significantly different critical loads, P_Y, for formation of the residual impression as well. Table 4 summarizes the critical load data. Tests are still in progress for some of the specimens to reduce the uncertainty in the critical load. Generally the critical loads for formation of a residual impression are greater for the bearing grade silicon nitrides than for the high-temperature or high strength grades, as would be expected. Planned microstructural characterization will reveal whether this difference arises from differences in the microstructure or not.

The bearing-grade silicon nitrides generally formed obvious ring cracks at loads, P_C 10-20 % below the critical load, P_Y, at which they first developed a residual impression. The other grades (High-T and High-toughness) always developed a residual impression before cracking. In many

cases (see Table 3) it was not possible to induce ring cracks. When ring cracks did form, they were invariably more irregular and difficult to detect than in the bearing-grade materials.

Status of Milestones

1. Propose to the IEA Executive committee the formation of a new subtask under Annex II to study contact damage (December 2001): complete.
2. Compare the nature of failure mechanisms in single-cycle ball-on-flat contact damage to those in rolling contact fatigue for silicon nitride. (March 2002) complete
3. Compare the nature of failure mechanisms in multi-cycle contact damage to those in rolling contact fatigue for silicon nitride. (July 2002) on schedule
4. Explore the feasibility of standardizing the 3-ball-on-rod rolling contact fatigue (RCF) test and assemble a team of users of the 3-ball-on-rod RCF test to conduct an interlaboratory study of RCF of engine ceramics. (September 2002) on schedule.

Communication/Visits/Travel

Said Jahanmir made a presentation entitled "Rolling Contact Fatigue Testing of Silicon Nitride" on May 23 at the STLE annual conference in Houston, TX.

Said Jahanmir traveled to the CIMTEC conference in Florence, Italy, in mid-July to discuss IEA Annex III activities.

Publications

None this period

References

[1] Douglas Glover, "A Ball-rod Rolling Contact Fatigue Tester," pp 107—124 in *Rolling Contact Fatigue Testing of Bearing Steels*, J. J. C. Hoo, ed. ASTM STP 771, American Society for Testing and Materials, Philadelphia, Pa, (1982)

[2] Harold L. Burrier Jr. "Optimizing the Structure and Properties of Silicon Nitride for Rolling Contact Bearing Performance," *Trib. Trans.*, **39**[2], 276—285 (1996)

[3] L.-Y Chao, R. Lakshminarayanan, N. Iyer, G.-Y. Lin, and D. K. Shetty, "Transient Wear of Silicon Nitride in Lubricated Rolling Contact," *Wear*, **223**, 58-65, (1998).

[4] Vimal Pujari and William Collins, "All Ceramic Bearing", United States Patent 6158894,December 12, 2000.

[5] Deborah L. Allen, "Effect of Composition and Physical Properties of Silicon Nitride on Rolling Wear and Fatigue Performance," *Trib. Trans.*, **37**[2], 410—414, (1994)

[6] G. R. Anstis, P. Chantikul, B. R. Lawn and D. B. Marshall., *J. Am. Ceram. Soc.* **64**[9] 533-538 (1981)

Table 1 Summary of RCF Tests to date

Rod-Track	Initial Stress (GPa)	Ball Mat'l	# Cycles	Track depth (μm)	Spall size	Notes; why shutdown
HP1-0	6.3	AISI 52100	1.3E7	0.2	no spall	ball spall
HP1-4	6.3	AISI 52100	5.8E6	0.4	no spall	ball spall
HP1-5	6.3	AISI 52100	5.2E7	3.0	no spall	3 restarts, all ball spalls
HP5-1	6.3	AISI 52100	3.1E7	0	no spall	suspended test
HP1-1a	6.3	AISI 52100	2.3E7	0.4	no spall	
CF6-1	6.3	AISI 52100	<3.5E7	0	19.3 μm deep	suspended test
CF6-2	6.3	AISI 52100	6.27E7	0	2 μm deep	ball spall
CF6-14	6.3	AISI 52100	5.8E7	0	no spall	suspended test
CF6-3	7.3	Si_3N_4	3.6e5	0	19.6 μm ¼ circum	rod spall
CF6-4	7.3	Si_3N_4	3.1E5	0	27.9 μm ¼ circum	rod spall
CF4-1	7.3	Si_3N_4	4.6E5	2.2	16.5 μm 1/3 circum	rod spall
CF4-3	6.3	Si_3N_4	2.5E7	53	uniform wear	test suspended
CF4-4	6.3	Si_3N_4	2.4E7	35.5	uniform wear	test suspended
CF6-5	7.3	Si_3N_4	8.8E5	0.2	33.3 μm ¼ circum	rod spall
CF6-2a	6.3	Si_3N_4	7.5E7	56.3	no spall, uniform wear	test suspended
CF6-3a	6.3	Si_3N_4	1.1E6	0.9	10.9 μm ½ circum	rod spall
HP5-2	7.3	Si_3N_4	2.3E8	58.6	no spall	uniform, deep wear; suspended test
HP5-3	7.3	Si_3N_4	1.2E7	86.3	no spall,	machine failure
HP5-6	6.3	Si_3N_4	9.8E7	62.7	no spall	test suspended
HP1-6	6.3	Si_3N_4	8.4E7	48.5	no spall	test suspended
			Wear Rate Tests			
HP5-4	7.3	Si_3N_4	4.1E5	0.7	no spall	test suspended
HP5-5	7.3	Si_3N_4	9.8E5	5.6	no spall	test suspended
HP5-7	7.3	Si_3N_4	2.2E6	22.0	no spall	test suspended
HP1-11	6.3	Si_3N_4	5.2E5	0.3	no spall	test suspended
HP1-12	6.3	Si_3N_4	1.0E6	0.5	no spall	test suspended
HP1-13	6.3	Si_3N_4	2.4E6	25.2	no spall	test suspended
HP1-7	5.0	Si_3N_4	9.9E7	28.7	no spall	test suspended
HP1-8	5.0	Si_3N_4	3.4E7	21.6	no spall	test suspended
HP1-9	5.0	Si_3N_4	1.2E7	6.8	no spall	test suspended
HP1-10	5.0	Si_3N_4	1.0E6	0.3	no spall	test suspended
HP5-8	4.0	Si_3N_4	8.5E7	7.4	no spall	test suspended
HP5-9	4.0	Si_3N_4	3.4E7	7.3	no spall	test suspended
HP5-10	4.0	Si_3N_4	1.1E7	4.8	no spall	test suspended
HP5-11	4.0	Si_3N_4	1.1E6	0	no spall, no wear	test suspended

Table 2: Si_3N_4 Properties

Material	Typical use	H_{K1} GPa	$u(H_{K1})$ GPa	H_{V10} GPa	$u(H_{V10})$ GPa	K_{1c} MPa $m^{1/2}$	$u(K_{1c})$ MPa $m^{1/2}$
147-31N	Bearing	14.07	0.15	14.88	0.16	4.32	0.05
N8201	Bearing	13.68	0.15	14.83	0.14	4.56	0.07
NBD-100	Bearing	16.14	0.11	18.61	0.23	3.41	0.08
NBD-200	Bearing	14.48	0.11	15.32	0.16	4.34	0.02
TSN-03NH	Bearing	14.48	0.11	15.45	0.17	4.67	0.07
GN-10	High-T	14.30	0.11	15.51	0.34	4.67	0.28
AS800	High-T	13.36	0.17	14.70	0.31	4.74	0.08
SN88	High-T	14.18	0.11	14.56	0.21	3.80	0.10
NT-164	High-T	14.53	0.16	15.72	0.22	3.94	0.09
GS44	High strength	13.52	0.11	15.12	0.39	4.72	0.08
5Y-2Al-1Mg	experimental	14.68	0.39	14.27	0.09	5.21	0.15
13Yb-.05Al	experimental	13.21	0.19	15.20	0.47	4.71	0.13

Table 3: Critical Loads, P_C, for ring crack formation

	3.175 mm WC ball				6.35 mm WC ball			
	Cracking load (N)		P_C	$u(P_C)$ *	Cracking Load		P_C	$u(P_C)$
Material	Yes	No	(N)	(N)	Yes	No	(N)	(N)
147-31N	?	498			1550	1451	1500.5	49.5
N8201	860	699	779.5	80.5	2239	1761	2000	239
NBD-100	560	N/D†			1019	N/D		
NBD-200	560	N/D			1019	N/D		
TSN-03NH	860	699	779.5	80.5	1761	1356	1558.5	202.5
GN-10	N/D	1044			N/D	2796		
AS800	1252	1019	1135.5	116.5	N/D	3439		
SN88	860	699	779.5	80.5	1761	N/D		
NT-164	860	699	779.5	80.5	2796	2239	2517.5	278.5
GS44	1252	1044	1148	104	3439	2796	3117.5	321.5
13Yb-.05Al	N/D	860			N/D	2796		
5Y-2Al-1Mg	N/D	1044			N/D	N/D		

(*) uncertainty in critical load (max-min)/2 † N/D = not determined—critical load is above or below max or min load
? replicate tests give different critical loads in the range XX < P < XX

Table 4: Critical load, P_Y, for residual impression

	3.175 mm WC Ball				6.35 mm WC Ball			
Material	Yes	No	P_Y	$u(P_Y)$	Yes	No	P_Y	$u(P_Y)$
147-31N	440	339	389.5	50.5	1761	1653	1707	54
N8201	699	560	629.5	69.5	2796	2239	2517.5	278.5
NBD-100	699	560	629.5	69.5	1356	1019	1187.5	168.5
NBD-200	699	560	629.5	69.5	2239	1761	2000	239
TSN-03NH	860	699	779.5	80.5	N/D	2796		
GN-10	699	N/D			1761	N/D		
AS800	255	N/D			1019	743	881	138
SN88	699	N/D			1761	N/D		
NT-164	560	440	500	60	1356	1019	1187.5	168.5
GS44	440	339	389.5	50.5	1019	N/D		
13Yb-.05Al	560	N/D			1356	N/D		
5Y-2Al-1Mg	560	N/D			N/D	N/D		

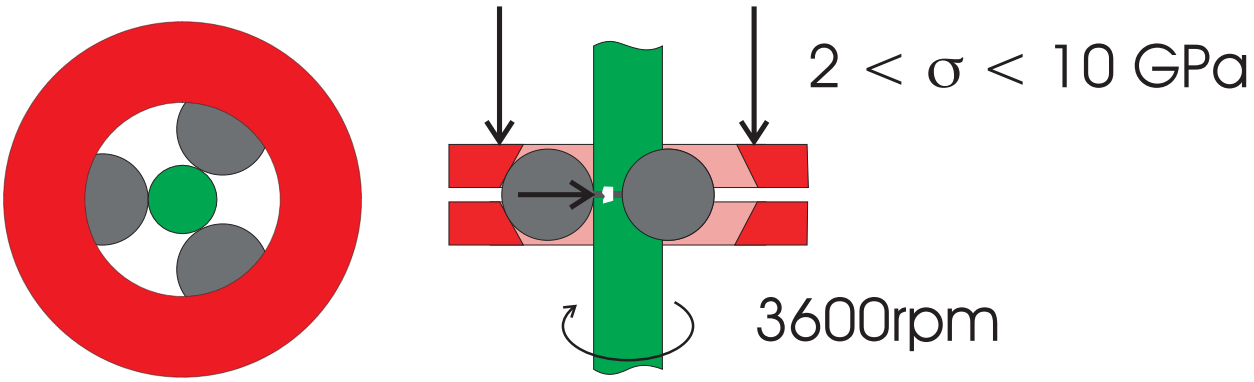

Figure 1. Schematic of the rolling contact fatigue test geometry

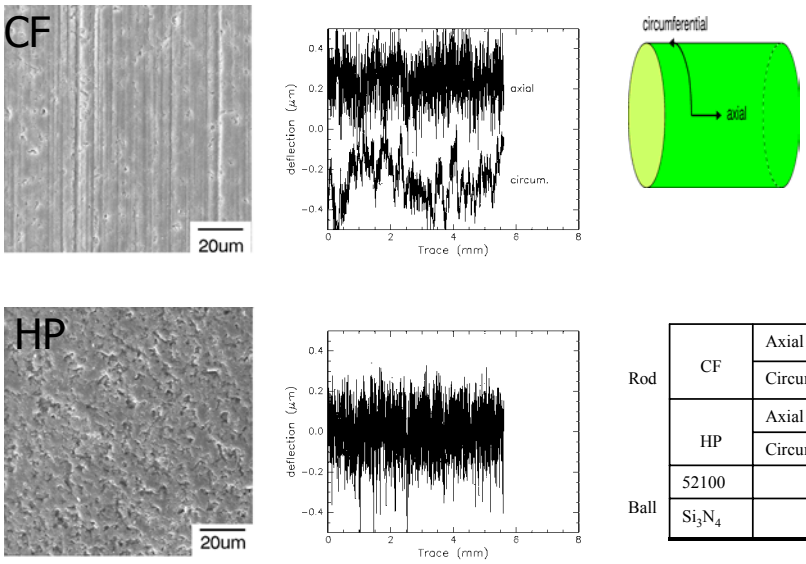

			R_a um
Rod	CF	Axial	0.069±0.002
		Circum	0.081±0.0005
	HP	Axial	0.081±0.0002
		Circum	0.082±0.0004
Ball	52100		0.985±0.010
	Si_3N_4		0.016

Figure 2. SEM images (secondary electrons) as well as axial and circumferential surface roughness traces of the CF and HP finished test bars.

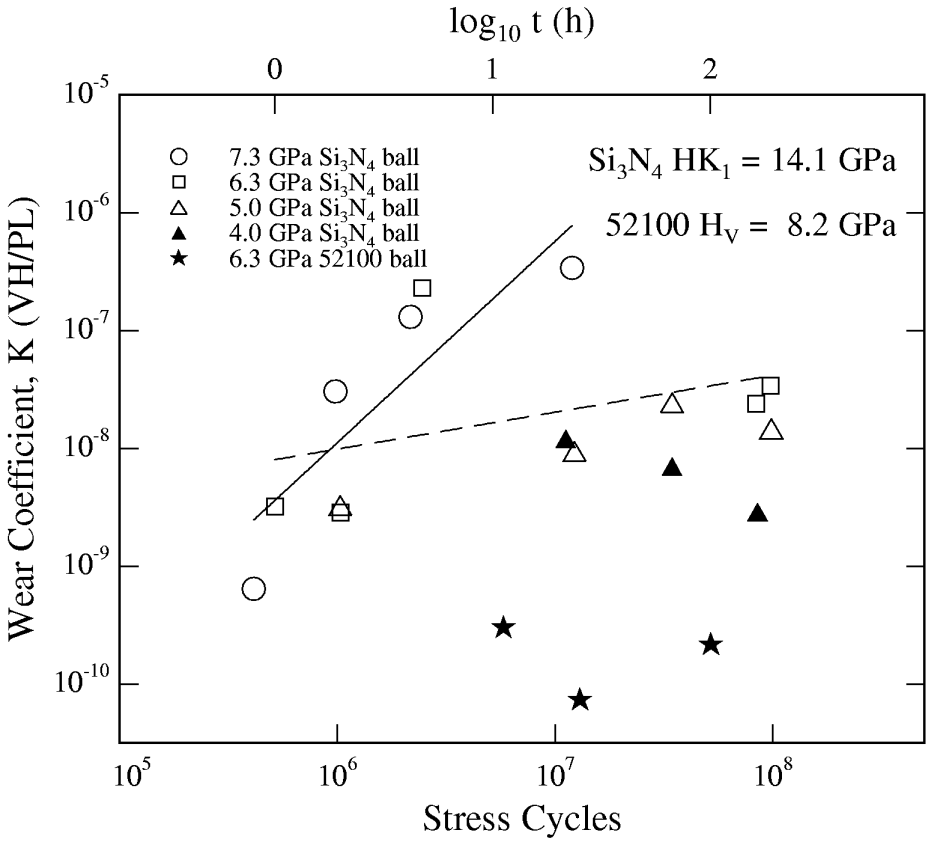

Figure 3. Wear coefficient for rolling contact wear of HP finished rods at different initial contact stresses.

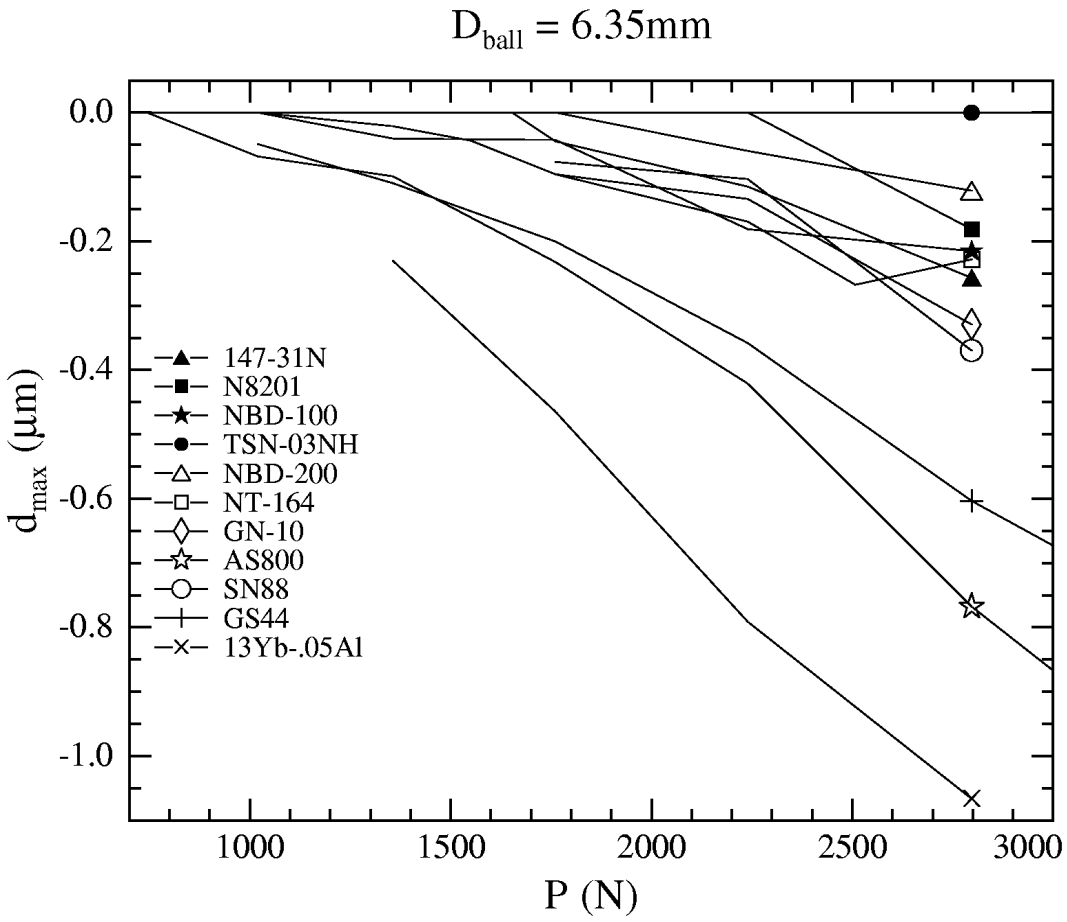

Figure 4. Residual impression depth , d_{max} as a function of contact load for 6.35 mm

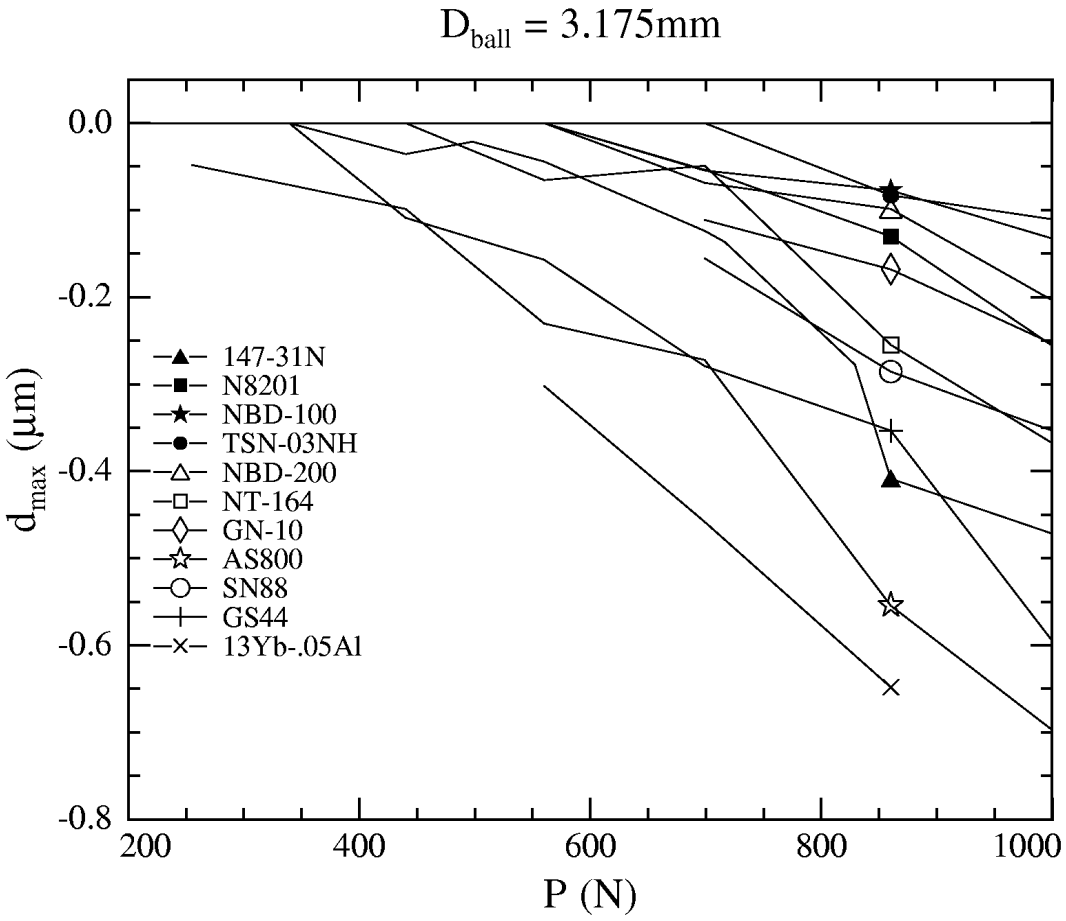

Figure 5. Residual impression depth, d_{max} as a function of contact load for 3.175 mm diameter balls

Mechanical Property Test Development

George Quinn
NIST

Objective/Scope

This task is to develop mechanical test method standards in support of the Propulsion Systems Materials Program. Test method development should meet the needs of the DOE engine community but should also consider the general USA structural ceramics community as well as foreign laboratories and companies. Draft recommendations for practices or procedures shall be developed based upon the needs identified above and circulated within the DOE engine community for review and modification. Round robins will be conducted as necessary. Procedures will be standardized by ASTM and/or ISO.

Technical Highlights

1. General

Analysis of machining damage cracks in silicon nitride was completed this period. A first draft of a lengthy report was completed in late May. The report will be prepared as a NIST monograph. It has over 100 illustrations and schematic drawings of machining cracks. It is the most thorough fractographic characterization of machining damage ever done. We are beginning to get some important practical payoffs from this work. We have a better understanding of machining damage, how to detect it, how to control it, and how to prepare test standards. The report also has an analysis of the trends in machining damage severity as a function of machining conditions. There are some stunning, contra-intuitive new findings. Performance may be limited not by the average grinding wheel characteristics, but by a single severe abrasive grit in the wheel! Silicon nitrides with greater fracture toughness develop deeper, more severe grinding crack damage than those in less tough silicon nitrides ground under the identical machining conditions!

As always, there are follow-ups and balloting procedures underway for several ASTM and ISO standards. New papers on the effective surfaces and effective volumes of rods and rectangular bars have been written. A paper was written and submitted on the application of the methods in the fracture toughness standard C 1421 to Ceradyne's SRBSN.

2. Fracture Toughness

a. ASTM C 1421 This topic is completed. A paper on the application of C 1421 to Ceradyne's production grade sintered reaction bonded silicon nitride grade Ceraloy 147 was prepared and sent to the American Ceramic Society. Consistent results were obtained by when the 3 test methods specified in C 1421 were used. This is good news.

b. ISO DIS 18756, Fracture Toughness by the SCF method

This document is nearing completion. It will be voted on as a formal "Draft International Standard" in mid 2002.

3. Flexural Strength of Advanced Ceramics – Rectangular Specimens

***a. ASTM C 1161** Revisions*

After 11 years on the books, ASTM standard C 1161 was overhauled in the fall of 2001. Twenty-six revisions were approved. Four follow on revisions were balloted in late January 2002. In this quarter, much time was spent remedying many mistakes in the ASTM proof copy.

***b. ASTM C 1211**, Elevated Temperature Flexural Strength Revisions*
This standard, which is the elevated temperature version of C1161, was due for an overhaul. In April twenty separate ballot items were prepared and sent to ASTM for balloting in the fall of 2002. The changes are similar to those made to C 1161, the room temperature standard.

***c. ISO 17565,** Elevated Temperature Flexural Strength*
Fourteen editorial revisions were recommended for this standard. It passed its 5-month worldwide balloting period at the end of March 2002. It received 12 national affirmative ballots (including Japan and United Kingdom), no negatives, and two affirmatives with comment. It now begins its 5-month enquiry stage ballot as a FDIS, "Final Draft International Standard."

4. ASTM Standard C 1322, Fractographic Analysis of Advanced Ceramics
This ground breaking standard was due for renewal. It was the first standard in the world for normal fractographic analysis and interpretation of fractured strength-test specimens. In late December, the author in cooperation with Mr. J. Swab of the U.S. Army Research Laboratory compiled a group of 19 revisions to C 1322. They were balloted by ASTM in late January to mid-March 2002. The ballot responses were reviewed at the ASTM Committee meeting in St. Louis at the end of April 2002. A negative vote on the issue of some of the terms (including "Brittle fracture") caused the major section of the revisions that included new definitions to be thrown out. It will have to be reballoted in the Fall 2002 ballot. One of the ballot items, inclusion of a definition of "brittle fracture" is listed below:

> *Brittle fracture*, n – fracture that takes place with little or no preceding plastic deformation.
>
> Background – the term "brittle fracture" with a different definition was on the Spring 2002 ASTM ballot and received two negative votes that were sustained.
>
> The new definition proposed above was discussed and agreed to by those in attendance at the April 2002 subcommittee C28.05 meeting in St. Louis, MO. At that meeting, we reviewed definitions in Kingery's book "Introduction to Ceramics," Jack Wachtman's new book on "Mechanical Properties of Ceramics," Dave Richerson's books "Modern Ceramic Engineering," Mike Ashby's book "Engineering Materials," Frank McClintock and Ali Argon's book on "Mechanical Behavior of Materials," as well as other key references.
>
> Many of the definitions were similar.
>
> Subcommittee C28.05 agreed on the proposed definition above, that is simple adaptation of a similar definition in the famous Wolff, Hayden & Moffatt book: "The Structure and Properties of Materials, Mechanical Behavior, Vol. III," p. 145, (1965).

Many of the revisions were intended to shorten the document and make it easier for users to understand.

C 1322 was expanded in some areas. More guidance is given on component failure analysis. A simple flowchart was added that illustrates the logical order of the common fractographic analysis. A new, vastly expanded appendix of fracture mirror constants was added. It is the most complete tabulation of these parameters ever compiled. We also added many more examples and illustrations of machining damage cracks, based on the lessons we have learned in this program.

5. Flexural Strength Testing of Cylindrical Ceramic Specimens

The NIST Ceramic Machining Consortium program was completed in December 2001. Follow on analysis and intensive fractographic examination of hundreds of specimens continued until the end of May 2002. We have reached the point that we can detect transverse machining damage fairly easily in many materials. This was quite an achievement, since at the beginning of the study; the machining cracks seemed very elusive! ASTM standard C 1322 was revised to include numerous illustrations and general schematics of machining damage cracks. **Figures 1 and 2** show astonishing fracture surfaces of coarsely ground bars wherein the lighting has been adjusted to reveal a skin of machining damage cracking that completely extends along the bottom surface! These markings were very common in the coarse ground specimens. It is amazing, but one may be able to ascertain that machining damage was a likely fracture source from such markings, *even if the mirror and origin itself are obscured or lost.*

In the last quarterly report we presented an important summary graph and some preliminary conclusions showing the depth of machining damage cracks as a function of grinding wheel grit. The same figure but with some minor polishing is shown here as **Figure 3.** The general trend of our data on the Ceradyne SRBSN was consistent with data from as many as 10 other studies through the years, although the other data sets were far more sketchy or incomplete. It is now clear that abrasive grit size is the dominant parameter. While this is not unexpected, the full quantification and verification of the trend is new. Also the fact that many different silicon nitrides all have similar trends was surprising as shown in **Figure 3.** Most of the data shown is for transverse machining damage cracks, which are easier to discern. Other conclusions are listed below. The three **bold findings** are new conclusions that were not in the previously quarterly report.

- Damage depths in rods and bars are remarkably similar.
- Damage depths are remarkably similar from a variety of studies on variety of silicon nitrides over the course of 30 years.
- Although other factors such as depth of cut, wheel speed, wheel concentration, etc undoubtedly contribute to machining cracks damage, their influence is clearly secondary compared to grit size.
- Westinghouse's old (1970's) calculated estimates for longitudinally-machining crack depths match the experimentally observed outcome much better than the Daimler Benz estimates or Westinghouse's transverse grinding estimates.
- Machining crack size data at grit sizes finer than 600 grit are nonexistent. Few people have studied finer grits and usually machining cracks do not control fracture!
- Machining cracks are rarely if ever deeper than 100 μm.
- **Fracture from coarse-ground surfaces always started from one particular striation, not necessarily the deepest or most obvious one on the surface. Evidently single deleterious abrasive grit in the grinding wheel controlled the performance of the finished part.**
- **The very tough Dow sintered silicon nitride (K_{Ic} ~ 7.0 MPa√m) has deeper machining cracks than the other silicon nitrides!**
- **The more brittle, less tough Eaton reaction bonded silicon nitride has less severe machining cracks than the other silicon nitrides!**

(a)

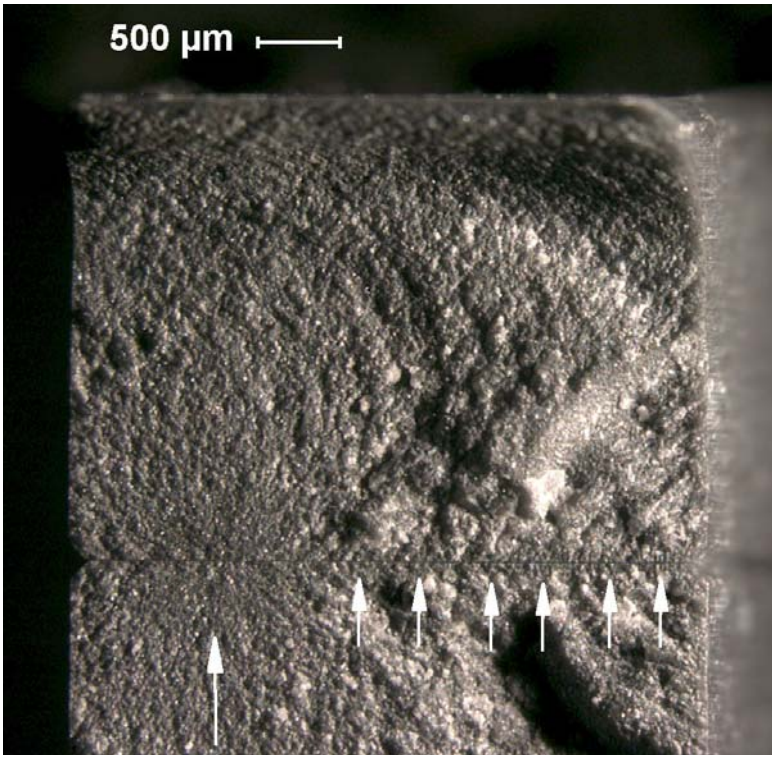

(b)

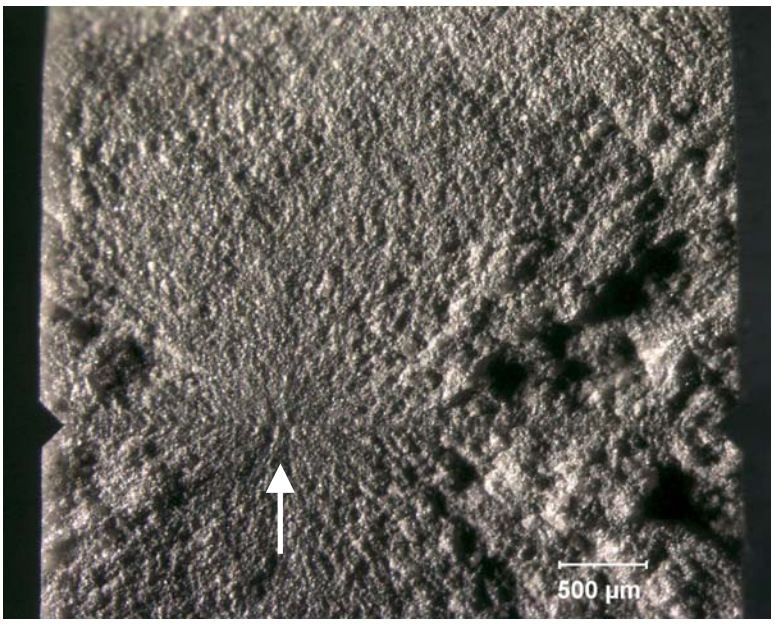

Figure 1. Optical photos of a" zipper crack" in 150 grit transversely-ground Ceradyne SRBSN bars. Both fracture halves are mounted back-to-back. The large arrow in (a) identifies the **"coarse zipper crack"** at the origin, but the machining crack damage is also visible as a thin band running across the entire fracture surface width (small arrows) (411 MPa). (b) shows a similar zipper crack in a 412 MPa specimen. Notice the three vertical fingerlets at the origin in this low magnification optical photo. The low angle directional illumination highlights these tell-tale features.

(a)

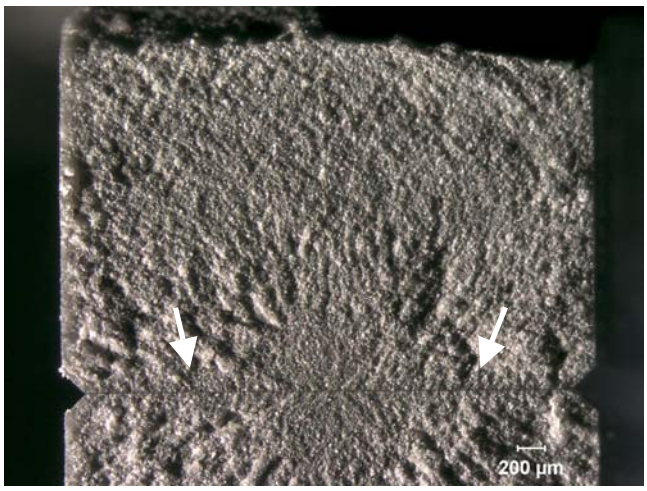

(b)

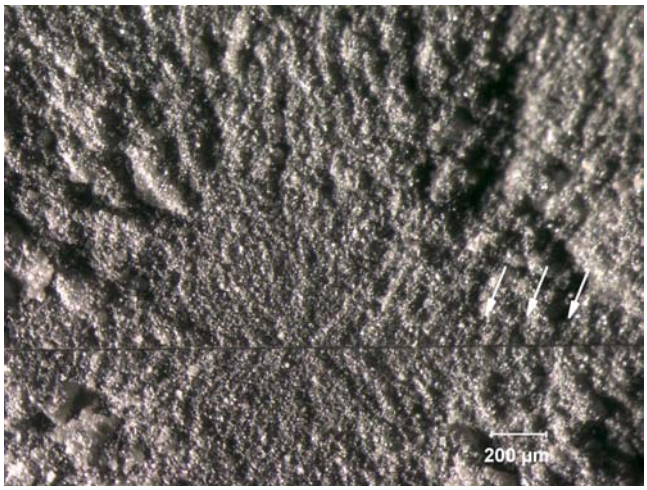

(c)

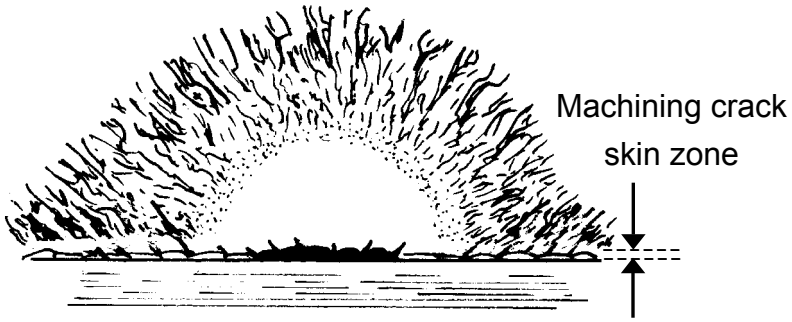

Figure 2. Optical photos (a, b) and matching schematic (c) of a 65 µm deep zipper cracks in a 150 grit transversely ground SRBSN bar (399 MPa). The mirror and the origin are in the middle, but the thin band of machining crack damage extends out to either side to the specimen side surfaces marked by the large arrows in (a) and small arrows in (b). (c) is a schematic view which illustrates that the depth of the machining crack skin zone is similar to the depth of the cracks at the origin.

The finding that a single striation was the cause of fracture in many coarse ground specimen was stunning. This should set off new lines of research on the effects of machining on strength, reliability and performance. *Average grinding wheel properties may not be as important as one atypical diamond abrasive grit.*

The last two findings are remarkable and real. Tougher silicon nitrides have deeper damage. Grinding was done in the same shops and to the same specifications as the Ceradyne SRBSN that was used for the core of the study. That tough silicon nitrides are apt to have severer machining damage is contra intuitive and contradicts some models of machining damage. There is a simple explanation, however, which will be revealed in our paper that is in preparation. The comprehensive paper was in preparation for the Journal of Machining Science and Technology, but the paper became too long in large part due to the numerous illustrations. It will be prepared as a special NIST monograph and a condensed summary paper will be submitted to the Journal of Machining Science and Technology.

A new paper on the derivation of effective surfaces and effective volumes for rod specimens tested in flexure was written for the Journal of the American Ceramic Society. It includes a handy simple compilation of these factors. They are one building block in the eventual construction of a new ASTM standard test method for cylindrical rods. Flexural testing of rods is inefficient in sampling either volume or surface flaws. Only a tiny portion of the rod (the very bottom) experiences the true maximum tensile stresses. Hence, the effective volume of rectangular "B" bars is similar to that for physically larger rods. Furthermore, the effective surface of rectangular "B" bars is usually greater than that of larger rods.

A new paper was written on the surprising finding that conversion (or scaling) factors for converting ASTM flexural strengths to JIS strengths is <u>independent of whether flaws are surface or volume distributed</u>. This is a curious conclusion, but verified by simple mathematical analysis. They key is that the cross section sizes of the ASTM and JIS specimens are identical (3 mm x 34 mm). Hence, the stress gradients are the same. The scaling independence has an important practical ramification: Conversion of strength numbers from JIS to ASTM or to CEN or ISO standards does not depend upon what kind of flaws are present. Fractographic analysis is unnecessary! Strength numbers may be adjusted by a simple factor when converting from testing configuration to another.

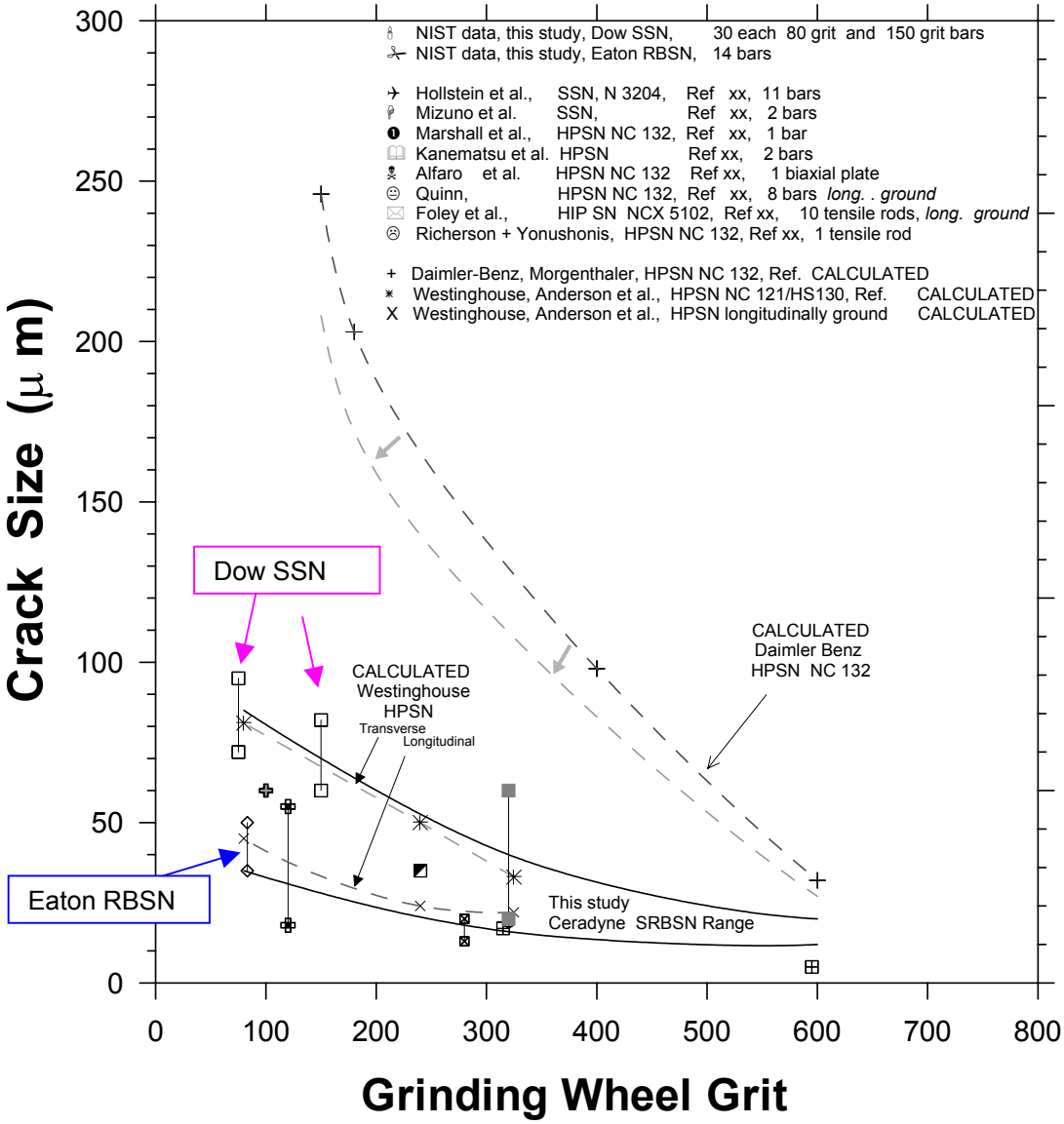

Figure 3 Machining crack size versus wheel grit from a variety of studies for silicon nitride. The **range** of outcomes for the SRBSN from the NIST study are included as solid lines. With the exception of the Daimler Benz calculations and the Dow SSN data, nearly all the data fit a single trend.

Figure 4 summarizes the depth of machining cracks in the sintered reaction bonded silicon nitride as a function of diamond wheel grit size. The depth numbers were based on hundreds of observations. Other dense silicon nitrides may be expected to have similar sized cracks.

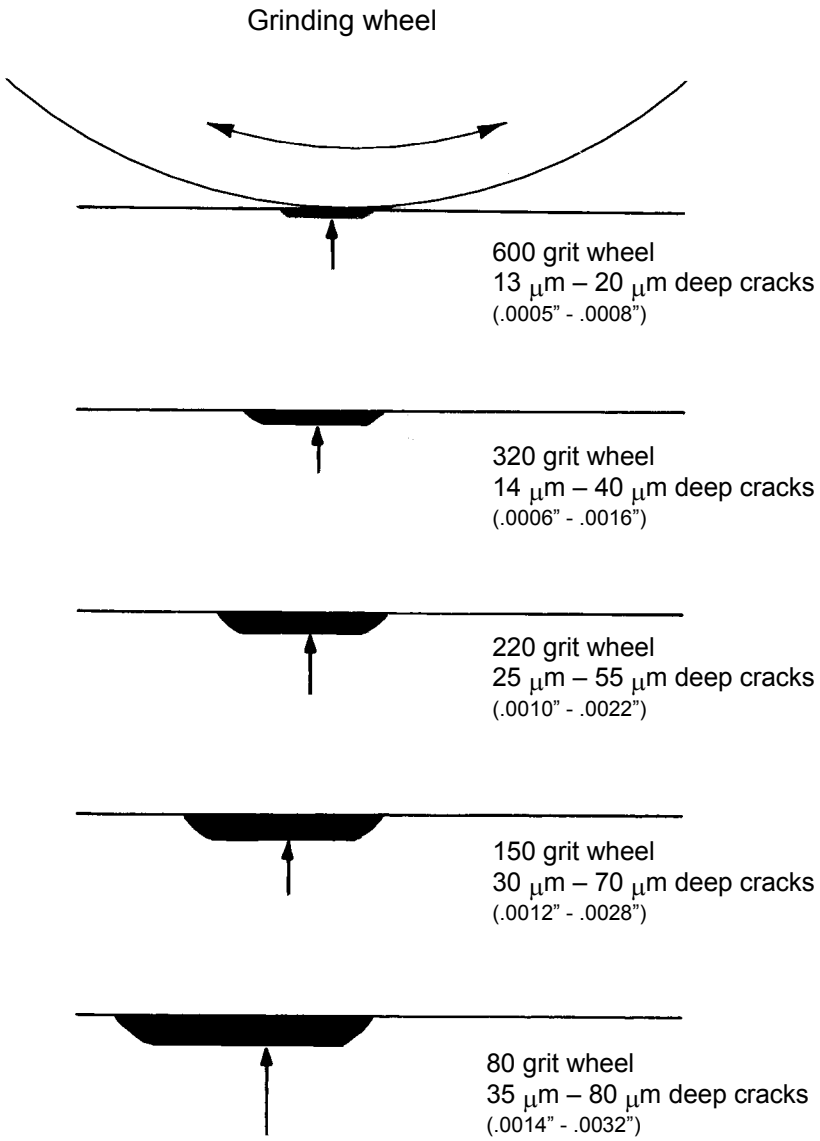

Figure 4. Depth of machining damage as a function of grinding wheel grit in SRBSN silicon nitride.

6. Compare SCF Knoop artificial cracks to machining cracks in Ceradyne SRBSN
An oral presentation on comparing fracture toughness data from Knoop artificial flaws to data generated from fractographic and strength analysis for real machining cracks was presented at the American Ceramic Society Annual Meeting in April 2002, in the Van Frechette Memorial symposium.

Status of Milestones
We seized on the opportunity to thoroughly characterize machining cracks. This plus, the extra time needed to organize and manage the major revisions to ASTM C 1161 and C 1322, have delayed progress on several tasks such as a new cylindrical rod strength test method and diametral compression work.

412146	Ballot major revisions to ASTM C 1161 flexural strength	September 2001, **Completed, October 2002✓**
412147	Prepare ballot revisions for ASTM C 1322, Fractographic Analysis	April 2002, **Completed, January 2002✓**
412148	Prepare follow on specimen machining revisions to ASTM C 1161 flexural strength if needed	April 2002 **Completed, April 2002✓**
412149	Prepare ballot-ready first ASTM draft of cylindrical rod flexure strength test	April 2002 **Delayed**
412150	Prepare paper on effect of machining on strength of SRBSN rods.	May 2002 **In progress, First draft done**
412151	Prepare review paper on flexural testing of cylindrical rods.	October 2002

Communications/Visits/Travel
Dave Carruthers, formerly of Kyocera and now with Carruthers Associates, contacted G. Quinn for information about the ASTM fracture toughness standard C 1421. Ray Cutler of Ceramatec also inquired about C 1421 and the ASTM hardness tests C 1326 and C 1327. Bill Mandler of Enceratec contacted G. Quinn about Weibull statistics and effective volume and effective surface scaling and conversion of strength numbers generated by the ASTM and JIS standards. Free copies of a simple bend fixture design for flexural strength testing in accordance with ASTM C 1161 were sent to Foster Miller in Waltham, MA. A letter was sent to Kristin Breder at St. Gobain about zeroing in on the exact thermal shock ΔT_c by water quench experiments. This was in connection with her ASTM draft standard. An old early 1970's paper on how the critical temperature can determined efficiently by using artillery fire techniques (shoot long, then short, and step towards the target) was written by Lt. Charles Seaton of Watertown Arsenal. The list of new fracture mirror constants was sent to Al Segal at Washington State University. A list of C-28 ASTM standards was sent to Prof. Jack Mecholsky at University of Florida so that he can present them to his students. A letter and VAMAS–ISO report on thermal conductivity measurements of thin films was sent to Steve Gonczy the C 28.01 chairman.

Additional announcements and letters and specimen s blueprints about the ASTM C 1161 revisions were sent out to about 20 interested parties.

Publications and presentations
1. G. D. Quinn and J. A. Salem, "Effect of Lateral Cracks Upon Fracture Toughness Determined by the Surface Crack in Flexure Method," published by J. Am. Ceram. Soc. 85 [4] 873-80 (2002).

2. G. D. Quinn, P. J. Patel, and I. Lloyd, "Effect of Loading rate Upon Conventional Ceramic Microindentation Hardness," accepted by the Journal of Research of NIST April, 2002.
3. S. W. Freiman and G. D. Quinn, "How Standards Help Bring New Materials to Market," Facets, p1 +5 International Union of Materials Research Societies, Volume 1, #3, July 2002.
4. G. D. Quinn, J. J. Swab, and M. J. Motyka, "Fracture Toughness of a Toughened Silicon Nitride by ASTM C 1421," subm to J. Am. Ceram. Soc., May 2002.
5. G. D. Quinn, "Weibull Strength Scaling for Standardized Rectangular Flexure Specimens," subm. to J. Am. Ceram. Soc., May 2002.
6. G. D. Quinn, "Weibull Effective Volumes and Surfaces for Cylindrical Rods Loaded in Flexure," subm. to J. Am. Ceram. Soc., May 2002.
7. G. D. Quinn, "How to Break a Bend Bar and What It Means," presented at the Annual Meeting of the American Ceramic Society, April 29, 2002, St. Louis, Mo.
8. G. D. Quinn, "Fractographic Analysis of Machining Cracks Versus Controlled Artificial Flaws in a Commercial Toughened Silicon Nitride," presented at the Annual Meeting of the American Ceramic Society, April 29, 2002, St. Louis, Mo.